

See discussions, stats, and author profiles for this publication at: <https://www.researchgate.net/publication/251470142>

Influence of Grain Boundary Structure on Dislocation Nucleation in FCC Metals

Chapter *in* Dislocations in Solids · December 2008

DOI: 10.1016/S1572-4859(07)00002-2

CITATIONS

62

READS

878

3 authors, including:



Mark A. Tschopp

Army Research Laboratory

170 PUBLICATIONS 2,530 CITATIONS

[SEE PROFILE](#)



Douglas E. Spearot

University of Florida

80 PUBLICATIONS 1,311 CITATIONS

[SEE PROFILE](#)

Some of the authors of this publication are also working on these related projects:



Nanocrystalline Material Design [View project](#)



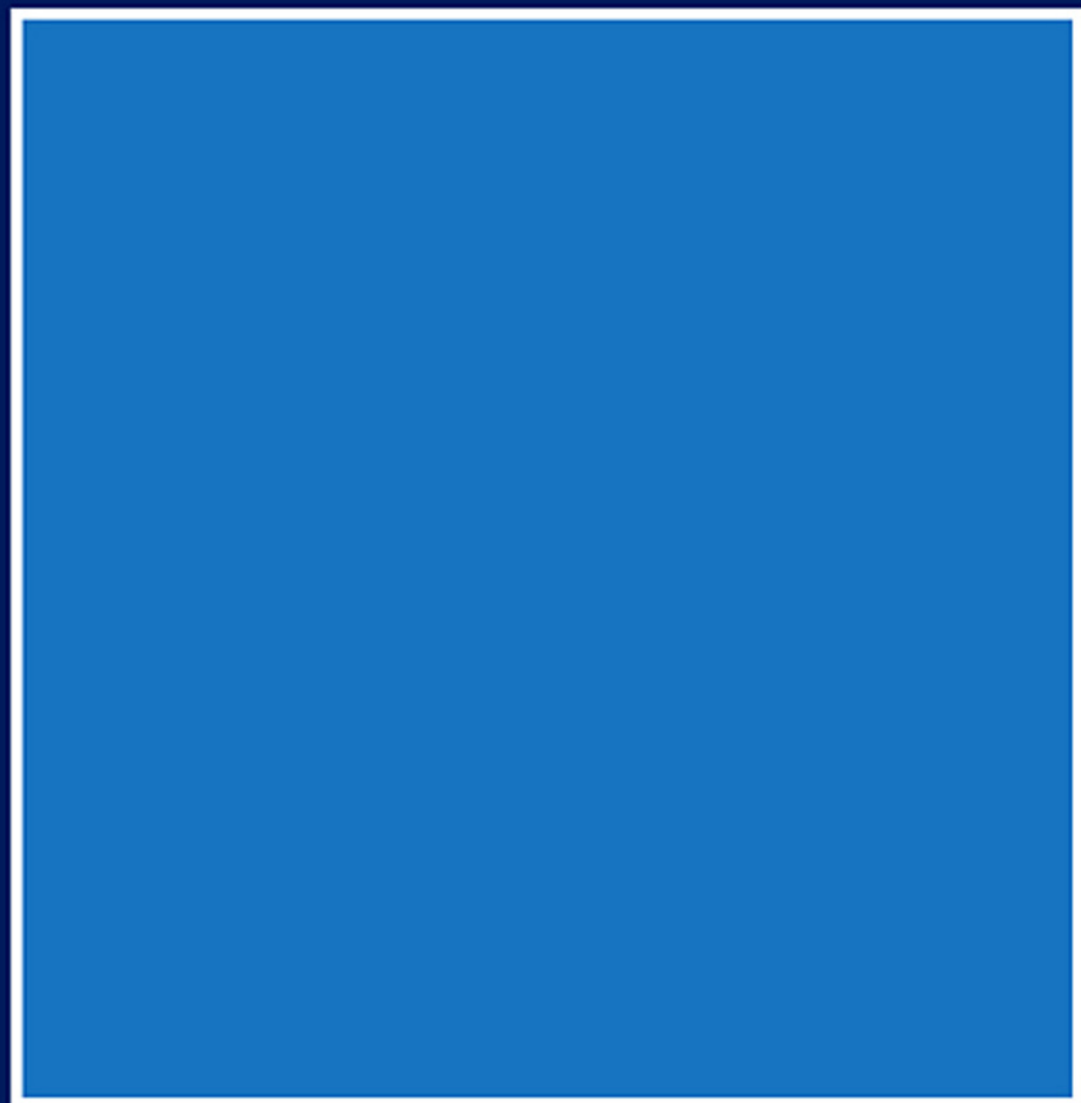
Deformation in HCP materials [View project](#)

Edited by
J.P. Hirth

A Tribute to F.R.N. Nabarro

Dislocations in Solids

Volume 14



North-Holland

Dislocations in Solids

Volume 14

This page intentionally left blank

Dislocations in Solids

Volume 14

A Tribute to F. R. N. Nabarro

Edited by

J. P. HIRTH

Hereford, AZ, USA



Amsterdam • Boston • Heidelberg • London • New York • Oxford
Paris • San Diego • San Francisco • Singapore • Sidney • Tokyo

North-Holland is an imprint of Elsevier



Elsevier
Radarweg 29, PO Box 211, 1000 AE Amsterdam, The Netherlands
Linacre House, Jordan Hill, Oxford OX2 8DP, UK

First edition 2008

Copyright ©2008 Elsevier B.V. All rights reserved

No part of this publication may be reproduced, stored in a retrieval system or transmitted in any form or by any means electronic, mechanical, photocopying, recording or otherwise without the prior written permission of the publisher

Permissions may be sought directly from Elsevier's Science & Technology Rights Department in Oxford, UK: phone (+44) (0) 1865 843830; fax (+44) (0) 1865 853333; email: permissions@elsevier.com. Alternatively you can submit your request online by visiting the Elsevier web site at <http://www.elsevier.com/locate/permissions>, and selecting *Obtaining permission to use Elsevier material*

Notice

No responsibility is assumed by the publisher for any injury and/or damage to persons or property as a matter of products liability, negligence or otherwise, or from any use or operation of any methods, products, instructions or ideas contained in the material herein. Because of rapid advances in the medical sciences, in particular, independent verification of diagnoses and drug dosages should be made

Library of Congress Cataloging-in-Publication Data

A catalog record for this book is available from the Library of Congress

British Library Cataloguing in Publication Data

A catalogue record for this book is available from the British Library

ISBN: 978-0-444-53166-7

ISSN: 1572-4859

For information on all Elsevier publications
visit our website at books.elsevier.com

Printed and bound in Hungary

08 09 10 11 12 10 9 8 7 6 5 4 3 2 1

Working together to grow
libraries in developing countries

www.elsevier.com | www.bookaid.org | www.sabre.org

ELSEVIER

BOOK AID
International

Sabre Foundation

Preface

This volume is dedicated as a tribute to F.R.N. Nabarro, the founder of this series. As documented in his biography,¹ he made many contributions to dislocation theory in conventional materials and received a number of awards for that work. However, he was also a pioneer in applying dislocation and disclination concepts to unusual materials. This included such topics as disclinations in seashells, dislocations in liquid crystals, and dislocations in molecular crystals and viruses. His vision in these matters was reflected in the broad set of topics that has appeared in the thirteen volumes of *Dislocations in Solids* that he edited. The present volume continues in that spirit.

The first three chapters present results of atomistic simulations at the forefront in this burgeoning area. Van Swygenhoven and Derlet discuss dislocation behavior in nanocrystals and focus on some scaling problems in such simulations. Tschopp et al. present results on dislocation nucleation at grain boundaries, including a new nucleation mechanism. Demkowicz et al. discuss interphase interfaces, with Cu–Nb as an example, providing new insight into structures extending over several planes near the interface, with dislocations spreading in the interface, and with differing local point defect concentrations. Zbib and Khraishi give results of dislocation dynamics calculations using discrete dislocation segments. They treat size effects and high velocity dislocation behavior. Bonneville et al. consider dislocations in icosahedral quasicrystals, including a new mechanism for dislocation motion in such materials. Alshits et al. present a theory for the magnetoplastic effect that explains a wide variety of such phenomena in a self-consistent manner. Vitek and Paidar treat non-planar cores in a variety of crystals, including intermetallic compounds, ionic and covalent bonded structures, and molecular crystals. Seemingly conflicting deformation trends can be explained by their models.

¹ A.G. Every, *S. Afr. J. Sci.* 103 (2007).

This page intentionally left blank

Contents

Volume 14

<i>Preface</i>	v
<i>Contents</i>	vii
<i>List of Contents of Volumes 1–13</i>	ix
81. H. Van Swygenhoven and P.M. Derlet <i>Atomistic Simulations of Dislocations in FCC Metallic Nanocrystalline Materials</i>	1
82. M.A. Tschopp, D.E. Spearot and D.L. McDowell <i>Influence of Grain Boundary Structure on Dislocation Nucleation in FCC Metals</i>	43
83. M.J. Demkowicz, J. Wang and R.G. Hoagland <i>Interfaces Between Dissimilar Crystalline Solids</i>	141
84. H.M. Zbib and T.A. Khraishi <i>Size Effects and Dislocation–Wave Interaction in Dislocation Dynamics</i>	207
85. J. Bonneville, D. Caillard and P. Guyot <i>Dislocations and Plasticity of Icosahedral Quasicrystals</i>	251
86. V.I. Alshits, E.V. Darinskaya, M.V. Koldaeva and E.A. Petrzhiik <i>Magnetoplastic Effect in Nonmagnetic Crystals</i>	333
87. V. Vitek and V. Paidar <i>Non-planar Dislocation Cores: A Ubiquitous Phenomenon Affecting Mechanical Properties of Crystalline Materials</i>	439
<i>Author Index</i>	515
<i>Subject Index</i>	531

This page intentionally left blank

Contents of Volumes 1–13

VOLUME 1. The Elastic Theory

1979, 1st repr. 1980; ISBN 0-7204-0756-7

- J. Friedel, *Dislocations – an introduction* 1
1. A.M. Kosevich, *Crystal dislocations and the theory of elasticity* 33
 2. J.W. Steeds and J.R. Willis, *Dislocations in anisotropic media* 143
 3. J.D. Eshelby, *Boundary problems* 167
 4. B.K.D. Gairola, *Nonlinear elastic problems* 223

VOLUME 2. Dislocations in Crystals

1979, 1st repr. 1982; ISBN 0-444-85004-x

5. R. Bullough and V.K. Tewary, *Lattice theories of dislocations* 1
6. S. Amelinckx, *Dislocations in particular structures* 67
7. J.W. Matthews, *Misfit dislocations* 461

VOLUME 3. Moving Dislocations

1980; 2nd printing 1983; ISBN 0-444-85015-5

8. J. Weertman and J.R. Weertman, *Moving dislocations* 1
9. *Resistance to the motion of dislocations* (to be included in a supplementary volume),
10. G. Schöck, *Thermodynamics and thermal activation of dislocations* 63
11. J.W. Christian and A.G. Crocker, *Dislocations and lattice transformations* 165
12. J.C. Savage, *Dislocations in seismology* 251

VOLUME 4. Dislocations in Metallurgy

1979; 2nd printing 1983; ISBN 0-444-85025-2

13. R.W. Balluffi and A.V. Granato, *Dislocations, vacancies and interstitials* 1
14. F.C. Larché, *Nucleation and precipitation on dislocations* 135
15. P. Haasen, *Solution hardening in f.c.c. metals* 155
- H. Suzuki, *Solid solution hardening in body-centred cubic alloys* 191
- V. Gerold, *Precipitation hardening* 219
16. S.J. Basinski and Z.S. Basinski, *Plastic deformation and work hardening* 261
17. E. Smith, *Dislocations and cracks* 363

VOLUME 5. Other Effects of Dislocations: Disclinations

1980; 2nd printing 1983; ISBN 0-444-85050-3

18. C.J. Humphreys, *Imaging of dislocations* 1
19. B. Mutaftschiev, *Crystal growth and dislocations* 57
20. R. Labusch and W. Schröter, *Electrical properties of dislocations in semiconductors* 127
21. F.R.N. Nabarro and A.T. Quintanilha, *Dislocations in superconductors* 193
22. M. Kléman, *The general theory of disclinations* 243

- 23. Y. Bouligand, *Defects and textures in liquid crystals* 299
- 24. M. Kléman, *Dislocations, disclinations and magnetism* 349

VOLUME 6. Applications and Recent Advances

1983; ISBN 0-444-86490-3

- 25. J.P. Hirth and D.A. Rigney, *The application of dislocation concepts in friction and wear* 1
- 26. C. Laird, *The application of dislocation concepts in fatigue* 55
- 27. C.A.B. Ball and J.H. van der Merwe, *The growth of dislocation-free layers* 121
- 28. V.I. Startsev, *Dislocations and strength of metals at very low temperatures* 143
- 29. A.C. Anderson, *The scattering of phonons by dislocations* 235
- 30. J.G. Byrne, *Dislocation studies with positrons* 263
- 31. H. Neuhäuser, *Slip-line formation and collective dislocation motion* 319
- 32. J.Th.M. De Hosson, O. Kanert and A.W. Sleeswyk, *Dislocations in solids investigated by means of nuclear magnetic resonance* 441

VOLUME 7

1986; ISBN 0-444-87011-3

- 33. G. Bertotti, A. Ferro, F. Fiorillo and P. Mazzetti, *Electrical noise associated with dislocations and plastic flow in metals* 1
- 34. V.I. Alshits and V.L. Indenbom, *Mechanisms of dislocation drag* 43
- 35. H. Alexander, *Dislocations in covalent crystals* 113
- 36. B.O. Hall, *Formation and evolution of dislocation structures during irradiation* 235
- 37. G.B. Olson and M. Cohen, *Dislocation theory of martensitic transformations* 295

VOLUME 8. Basic Problems and Applications

1989; ISBN 0-444-70515-5

- 38. R.C. Pond, *Line defects in interfaces* 1
- 39. M.S. Duesbery, *The dislocation core and plasticity* 67
- 40. B.R. Watts, *Conduction electron scattering in dislocated metals* 175
- 41. W.A. Jesser and J.H. van der Merwe, *The prediction of critical misfit and thickness in epitaxy* 421
- 42. P.J. Jackson, *Microstresses and the mechanical properties of crystals* 461
- 43. H. Conrad and A.F. Sprecher, *The electroplastic effect in metals* 497

VOLUME 9. Dislocations and Disclinations

1992; ISBN 0-444-89560-4

- 44. G.R. Anstis and J.L. Hutchison, *High-resolution imaging of dislocations* 1
- 45. I.G. Ritchie and G. Fantozzi, *Internal friction due to the intrinsic properties of dislocations in metals: Kink relaxations* 57
- 46. N. Narita and J.-I. Takamura, *Deformation twinning in f.c.c. and b.c.c. metals* 135
- 47. A.E. Romanov and V.I. Vladimirov, *Disclinations in crystalline solids* 191

VOLUME 10. Dislocations in Solids

1996; ISBN 0-444-82370-0

- 48. J.H. Westbrook, *Superalloys (Ni-base) and dislocations* 1
- 49. Y.Q. Sun and P.M. Hazzledine, *Geometry of dislocation glide in $L1_2$ γ' -phase* 27
- 50. D. Caillard and A. Couret, *Dislocation cores and yield stress anomalies* 69
- 51. V. Vitek, D.P. Pope and J.L. Bassani, *Anomalous yield behaviour of compounds with $L1_2$ structure* 135
- 52. D.C. Chrzan and M.J. Mills, *Dynamics of dislocation motion in $L1_2$ compounds* 187
- 53. P. Veyssi re and G. Saada, *Microscopy and plasticity of the $L1_2$ γ' phase* 253
- 54. K. Maeda and S. Takeuchi, *Enhancement of dislocation mobility in semiconducting crystals* 443
- 55. B. Jo s, *The role of dislocations in melting* 505

VOLUME 11. Dislocations in Solids

2002; ISBN 0-444-50966-6

- 56. M. Zaiser and A. Seeger, *Long-range internal stress, dislocation patterning and work-hardening in crystal plasticity* 1
- 57. L.P. Kubin, C. Fressengeas and G. Ananthakrishna, *Collective behaviour of dislocations in plasticity* 101
- 58. L.M. Brown, *Linear work-hardening and secondary slip in crystals* 193
- 59. D. Kuhlmann-Wilsdorf, *The LES theory of solid plasticity* 211
- 60. H. Mughrabi and T. Ung r, *Long-range internal stresses in deformed single-phase materials: The composite model and its consequences* 343
- 61. G. Saada and P. Veyssi re, *Work hardening of face centred cubic crystals. Dislocations intersection and cross-slip* 413
- 62. B. Viguier, J.L. Martin and J. Bonneville, *Work hardening in some ordered intermetallic compounds* 459
- 63. T.M. Pollock and R.D. Field, *Dislocations and high-temperature plastic deformation of superalloy single crystals* 547

VOLUME 12. Dislocations in Solids

2004; ISBN 0-444-51483-X

- 64. W. Cai, V.V. Bulatov, J. Chang, J. Li and S. Yip, *Dislocation core effects on mobility* 1
- 65. G. Xu, *Dislocation nucleation from crack tips and brittle to ductile transitions in cleavage fracture* 81
- 66. M. Kleman, O.D. Lavrentovich and Yu.A. Nastishin, *Dislocations and disclinations in mesomorphic phases* 147
- 67. C. Coupeau, J.-C. Girard and J. Rabier, *Scanning probe microscopy and dislocations* 273
- 68. T.E. Mitchell and A.H. Heuer, *Dislocations and mechanical properties of ceramics* 339
- 69. R.W. Armstrong and W.L. Elban, *Dislocations in energetic crystals* 403
- 70. M.M. Chaudhri, *Dislocations and indentations* 447

VOLUME 13. Dislocations in Solids

2007; ISBN 0-444-51888-6

- 71. V.S. Deshpande, A. Needleman and E. Van der Giessen, *Discrete dislocation plasticity modeling of contact and friction* 1
- 72. J.P. Nowacki and V.I. Alshits, *Dislocation fields in piezoelectrics* 47
- 73. G. Ananthakrishna, *Statistical and dynamical approaches to collective behavior of dislocations* 81
- 74. R.C. Pond, X. Ma, Y.W. Chai and J.P. Hirth, *Topological modelling of martensitic transformations* 225
- 75. M. Niewczas, *Dislocations and twinning in face centred cubic crystals* 263
- 76. K. Edagawa and S. Takeuchi, *Elasticity, dislocations and their motion in quasicrystals* 365
- 77. J.C.H. Spence, *Experimental studies of dislocation core defects* 419

78. A.M. Minor, E.A. Stach and J.W. Morris, Jr., *In situ nanoindentation in a transmission electron microscope* 453
79. G.E. Ice and R.I. Barabash, *White beam microdiffraction and dislocations gradients* 499
80. D. Shilo and E. Zolotoyabko, *X-ray imaging of phonon interaction with dislocations* 603

Influence of Grain Boundary Structure on Dislocation Nucleation in FCC Metals

MARK A. TSCHOPP

School of Materials Science and Engineering, Georgia Institute of Technology, Atlanta, GA 30332-0245, USA

Air Force Research Laboratory (UTC), Wright-Patterson Air Force Base, Dayton, OH 45433, USA

DOUGLAS E. SPEAROT

Department of Mechanical Engineering, University of Arkansas, Fayetteville, AR 72701, USA

and

DAVID L. MCDOWELL

*Woodruff School of Mechanical Engineering, School of Materials Science and Engineering,
Georgia Institute of Technology, Atlanta, GA 30332-0405, USA*

Contents

1. Introduction	46
1.1. Overview of grain boundary geometry	48
1.2. The structural unit model	50
1.3. Modeling dislocation nucleation	53
2. Atomistic simulation methodology	54
2.1. Molecular statics	55
2.2. Molecular dynamics	56
2.3. Virial stress	57
2.4. EAM potentials	58
2.5. Bicrystal simulation geometry	59
3. Structure and energy of tilt grain boundaries in Cu and Al	61
3.1. Calculation of interface energy	61
3.2. Symmetric tilt grain boundaries	62
3.2.1. Interface energy	62
3.2.2. Interface structure	63
3.3. Asymmetric tilt grain boundaries	69
3.3.1. Interface energy	71
3.3.2. Interface structure	73
3.3.2.1. Inclination angles $\Phi < 70.53^\circ$	74
3.3.2.2. Inclination angles $\Phi \geq 70.53^\circ$	75
3.3.3. $\Sigma 3$ ATGB structure and faceting	77
4. Dislocation nucleation from symmetric and asymmetric tilt boundaries in Cu and Al	79
4.1. Symmetric tilt grain boundaries	81
4.1.1. $\Sigma 5$ (310) 36.9° interface	81
4.1.2. Grain boundaries with dissociated structure	85
4.1.3. Tensile stress required for dislocation nucleation	89
4.2. Asymmetric tilt grain boundaries	91
4.2.1. Stress required for dislocation nucleation	91
4.2.2. Low inclination angles ($\Phi \leq 35.26^\circ$)	93
4.2.3. Intermediate inclination angles ($35.26^\circ < \Phi < 70.53^\circ$)	95
4.2.4. High inclination angles ($\Phi \geq 70.53^\circ$)	97
4.2.5. Preferential dislocation nucleation in Cu	99
5. Models for dislocation nucleation: single crystals and GBs	100
5.1. Homogeneous dislocation nucleation in single crystal Cu	100
5.1.1. Influence of resolved stresses	100
5.1.2. Second generation model for dislocation nucleation in single crystals	106
5.1.3. Dislocation nucleation in single crystals under uniaxial compression	108
5.1.4. Effect of lattice distortion on resolved stress components	111
5.2. Model for dislocation nucleation from tilt grain boundaries	112
5.2.1. Symmetric tilt grain boundaries	112
5.2.2. Extensions to asymmetric tilt GBs	115
6. Insights and implications	117
6.1. Grain boundary dislocation sources	118
6.2. Disconnections and the description of GB defects	120
6.3. Tension-compression asymmetry in trailing partial emission in Cu	122
6.4. Activation volumes and energies for grain boundary dislocation nucleation	125

6.5. Influence of grain boundary free volume on dislocation nucleation	127
6.6. Continuum field theory	128
7. Concluding remarks	133
Acknowledgements	135
References	135

1. Introduction

According to materials scientist and philosopher Cyril Stanley Smith, the structure of materials is best described as a multilevel architecture, with “interplay of perfection and imperfection” among all length scales [1,2]. This point of view asserts that a clear understanding of material behavior at each length scale is imperative to elucidate the technological or economic value of a material [1]. However, many theories of macroscopic material behavior are not based on direct evaluation of micro- or nanoscale mechanisms. Two examples are the kinematic hardening model in continuum plasticity, which was posed to describe experimental observation of the Bauschinger effect [3], and the Hall–Petch relationship [4,5], which describes the increase in yield strength associated with the decrease in the grain size for metallic polycrystalline materials. Both Hall [4] and Petch [5] envisioned grain boundaries as obstacles to dislocation motion (resulting in dislocation pile-ups) and assumed that yield occurred once the stress exerted on the neighboring grain by the dislocation pile-up reached a critical value. Experimental observations of this type are of tremendous scientific importance; however, it is highly desirable to directly study the underlying material micro- and nanostructure with the aim of developing constitutive models that capture the activity and interaction of atomic-scale structure and associated mechanisms. For example, both experiments (cf. [6–8]) and simulations (cf. [9–12]) have reported that material softening occurs once the grain size is reduced below a critical grain diameter, which cannot be predicted by the classical Hall–Petch relationship. Moreover, it is understood that scale effects in plasticity occur over a range of mechanisms and scales.

This work focuses on modeling the atomic level mechanisms associated with the structure and inelastic behavior of homophase grain boundaries (GBs) on the nanoscale and developing structure–property relationships that incorporate these nanoscale observations. Several experimental studies on polycrystalline metallic samples have reported that interface structure has an effect on material properties, such as grain boundary energy, mobility, corrosion, crack nucleation and ductility (cf. [13,14]). Most of the published experimental investigations indicate that there is some correlation between the occurrence of “special” coincident site lattice boundaries and material properties; however, results published in the literature do not point to a universal relationship. In nanocrystalline materials, the grain boundaries play a more profound role in material behavior due to the increased interfacial area associated with the decrease in the grain size. In addition, nanoscale confinement severely limits the operation of traditional dislocation sources, such as Frank–Read sources [15], mandating that the grain boundaries participate directly in the accommodation of the applied strain. Thus, grain boundary dislocation emission and absorption [16–39], which may be coupled with atomic shuffling [38–40], stress assisted grain boundary sliding [38–45] and grain rotation [46], have all been observed in computational studies as potential grain boundary deformation mechanisms. Conceivably, the activation of

each grain boundary mechanism depends on several factors, including the electronic details of the material (intrinsic and unstable stacking fault energies), the grain size, the structure of the grain boundaries and the deformation conditions (strain state and strain rate).

The objective of this work is to use atomistic simulations to examine the structure and dislocation nucleation/emission behavior of symmetric and asymmetric tilt grain boundaries in FCC copper and aluminum. Discrete atomic scale mechanisms associated with dislocation nucleation are incorporated into a first-order constitutive model for the tensile strength of tilt grain boundaries. This atomistically motivated constitutive model explicitly incorporates the orientation dependence of the opposing lattice regions and the influence of porosity within the interface region through an average measure based on coordination. Furthermore, this work provides a detailed understanding of the influence of grain boundary structure on dislocation nucleation which is critical for the advancement of grain boundary engineering concepts. Recall that the objective of grain boundary engineering [47] is to increase the percentage of “special” grain boundaries and to reduce the connectivity of “random” grain boundaries through material processing. Reducing the connectivity of random boundaries is found to be particularly important, as polycrystalline samples with a properly oriented continuous path of weak boundaries would be susceptible to failure regardless of the percentage of special interfaces [48]. Schuh et al. [14] reported that the fraction of special grain boundaries can be increased through sequential cycles of straining and annealing. As a result, enhancements in corrosion resistance, creep resistance and crack nucleation and growth resistance under various loading conditions have been observed experimentally. Of particular effectiveness is the introduction of annealing twins [49], which are essentially highly coherent GBs. Molecular dynamics simulations in this work provide a more refined definition of “special” with regard to how grain boundary structure affects dislocation nucleation.

This chapter is organized as follows. The remainder of this section focuses on concepts related to grain boundary geometry and structure in metallic crystalline materials. Section 2 provides a brief overview of atomistic simulation techniques (equations of motion, interatomic potentials, etc.) and the specific simulation geometries used in this work to model grain boundary structure and dislocation nucleation. Section 3 discusses the dependence of grain boundary structure and energy on the misorientation angle/axis in the case of symmetric tilt grain boundaries and the inclination angle for asymmetric tilt grain boundaries. Section 4 investigates the relationship between interface structure and dislocation nucleation in symmetric and asymmetric tilt GBs. Section 5 presents a first-order, atomistically-inspired model designed to correlate the strength required for dislocation nucleation with interface structure via the interface free volume and the resolved stresses on the primary slip plane for uniaxial loading. To capture the influence of the lattice orientation, atomistic simulations of *homogeneous* dislocation nucleation in single crystals are also discussed. Section 6 discusses how atomic-level information of dislocation nucleation from grain boundaries can impact research in plasticity, micromechanics and grain boundary engineering techniques. A summary of major contributions in this work is provided in Section 7.

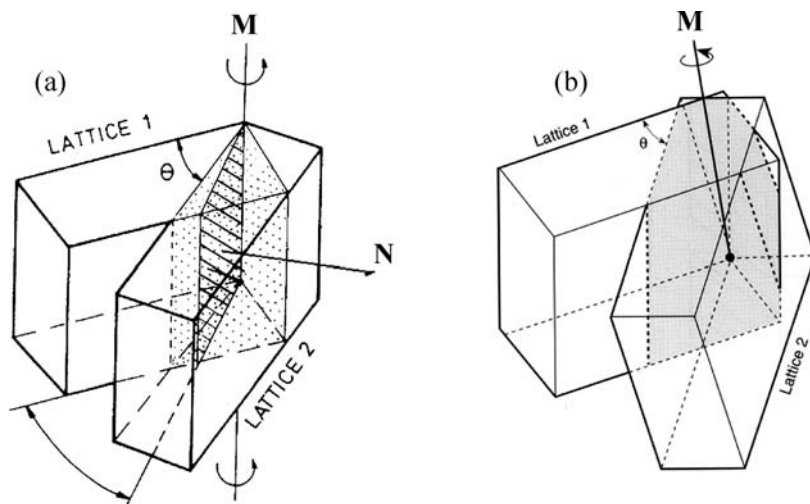


Fig. 1. Schematic representation of the grain boundary misorientation scheme for (a) tilt boundaries and (b) general boundaries. Reprinted from [13] with permission; © 1997 Maney Publishing.

1.1. Overview of grain boundary geometry

In general, solid–solid interfaces between crystalline regions may be classified into two categories: homophase and heterophase [50]. The set of homophase interfaces includes grain boundaries, twins and stacking faults in pure metals, whereas heterophase interfaces exist in binary and other material systems in which the composition and/or the Bravais lattice change across the interface plane. For homophase boundaries (such as those in this work), the degree of coherency is a function of the misorientation angle of the interface, the boundary plane orientation, and the nanoscale translations that exist to minimize the interface energy in the local neighborhood of the boundary. From a macroscopic perspective, planar interfaces between two crystal regions have five degrees of freedom [13,50,51], i.e., an interface is fully characterized by a misorientation angle, θ , a misorientation axis vector, \mathbf{M} , and the normal vector to the interface plane, \mathbf{N} . Fig. 1 shows a schematic of the misorientation scheme. Boundaries for which the normal to the interface plane is perpendicular to the misorientation axis ($\mathbf{M} \perp \mathbf{N}$) are defined as “tilt” interfaces, as shown in Fig. 1(a). Similarly, boundaries for which the normal to the interface plane is parallel to the misorientation axis are defined as “twist” interfaces. Grain boundaries in actual polycrystalline materials may have both tilt and twist character, as shown in Fig. 1(b). From a microscopic perspective, interfaces between crystal lattices have three additional degrees of freedom associated with the mutual nanoscale translation of the opposing lattice regions parallel and perpendicular to the interface plane. These translations exist to minimize the interface energy for a given misorientation. These microscopic degrees of freedom do not need to be explicitly prescribed when modeling grain boundary structures, as they are resolved naturally during the energy minimization procedure within the framework of the atomistic simulations performed in this work.

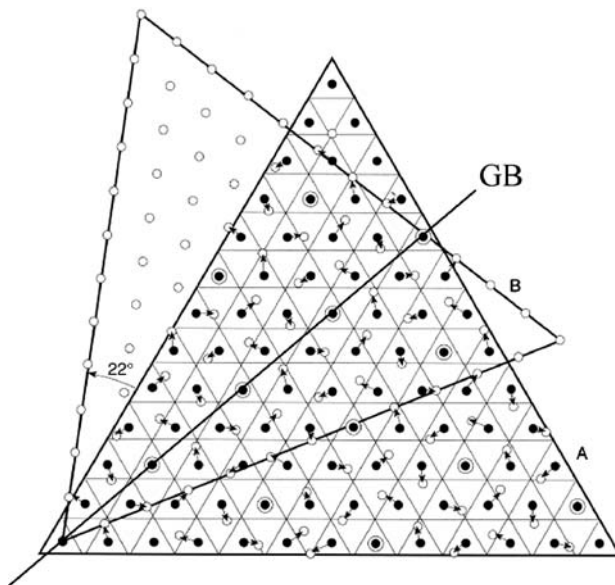


Fig. 2. Schematic of a $\Sigma 7$ coincident site lattice (CSL) model. 1 in 7 lattice sites are coincident between the two lattice regions. Reprinted from [13] with permission; © 1997 Maney Publishing.

A small subset of interface misorientations are considered geometrically “special” in the sense that the opposing lattice regions fit more closely across the interface plane [13,50,51]. To illustrate this concept, Fig. 2 shows a two-dimensional schematic of two interpenetrating FCC lattices. The two lattice regions, A and B, are rotated relative to one another around a common misorientation axis. Specific angle/axis combinations will result in an array of coincidence lattice points. This array of lattice points is known as the coincident site lattice (CSL), while the inverse density of coincident lattice points is defined as Σ . Specifically, in Fig. 2, lattice region B is rotated 22° around the $\langle 111 \rangle$ axis with respect to lattice region A. At this orientation, 1 in 7 lattice points is coincident between lattice regions A and B; thus, an interface with this angle/axis combination is defined as a $\Sigma 7$ misorientation using the CSL methodology. In general, the CSL methodology may be considered as a shorthand notation used to describe specific misorientation angle/axis combinations. However, the CSL methodology does not uniquely account for each of the five macroscopic degrees of freedom, i.e., the index of the interface plane (or planes in the case of asymmetric boundaries) must also be included with Σ to provide a complete description of the macroscopic grain boundary geometry. Furthermore, Σ does not provide a characterization of the microscopic degrees of freedom of a grain boundary. Two grain boundaries with the same Σ description can have very different grain boundary structures as observed in previous atomistic simulations [52,53]. This phenomenon will be discussed in greater detail in Section 3. Regardless, many authors have found that boundaries with low values of Σ typically have special geometric characteristics and material properties [13] and hence a complete understanding of the relationship between interface structure and material behavior is critical to the advancement of constitutive models in a wide range of material systems.

1.2. The structural unit model

The coherency of homophase low-angle tilt and twist grain boundaries ($\theta < 15^\circ$) may be described through dislocation based models [15,54] in which the degree of coherency can be directly related to the spacing between misfit dislocations within the interface plane. If the misorientation angle of the interface is greater than 15° , the cores of the interfacial dislocations become too densely packed to accommodate individual distinction, requiring a different description of the interface structure. Sutton and Vitek [55–57] proposed that the coherency and structure of homophase high-angle boundaries in FCC metals may be described via the identification of structural units along the interface plane. This methodology became known as the structural unit model (SUM) and can be envisioned as a consequence of the CSL description, because the mathematical pattern of coincident atomic sites leads directly to a repeating periodic structure at the interface, once the boundary plane is specified. Atomistic simulations by Sutton and Vitek [55–58] using a pair-potential showed that many interfaces in FCC metals may be viewed as a linear combination of structural units. Each structural unit is associated with a “favored” boundary for a given misorientation axis. For the $\langle 001 \rangle$ misorientation axis, Wang et al. [58] reported that the favored boundaries are the $\Sigma 1$ (110) (perfect lattice), $\Sigma 5$ (210), $\Sigma 5$ (310) and the $\Sigma 1$ (100) (perfect lattice) interfaces. The structural units associated with each of these boundaries were denoted A–D, respectively. The $\Sigma 5$ interface is the lowest order Σ boundary for the $\langle 001 \rangle$ misorientation axis; however, Sutton and Vitek surprisingly found that favored interfaces did not always correspond to the lowest value of Σ for a given misorientation axis. For the $\langle 110 \rangle$ misorientation axis, Sutton and Vitek [55] reported that favored boundaries exist at the $\Sigma 27$ (115) and $\Sigma 11$ (113) interfaces. Several other Σ boundaries exist around the $\langle 110 \rangle$ misorientation axis that have a lower Σ value. Rittner and Seidman [52,53] evaluated the entire range of $\langle 110 \rangle$ misorientations and found that the favored boundaries are the $\Sigma 1$ (001) (perfect lattice), $\Sigma 27$ (115), $\Sigma 11$ (113), $\Sigma 3$ (111), $\Sigma 9$ (221) and the $\Sigma 1$ (110) (perfect lattice) interfaces. The structural units associated with each of these boundaries were denoted A–E (with both $\Sigma 1$ ‘interfaces’ defined as A structural units). Note that the $\Sigma 3$ (112) interface is not found to be a favored boundary, even though it has a high density of coincident sites between lattice regions. This particular boundary is examined in detail in Sections 3 and 4.

There are, however, several limitations to the structural unit model. First, it is difficult to identify structural units with three-dimensional character, i.e., twist boundaries. Second, the SUM has limited applicability for interfaces with mixed tilt and twist character or if a high index misorientation axis is examined [59]. While only four structural units are required to characterize $\langle 001 \rangle$ tilt boundaries, for high index misorientation axes the number of independent structural units becomes extremely large. Third, the SUM fails to describe interfaces with delocalized structural units. Rittner and colleagues [52,53,60] showed that for materials with low stacking fault energies, the interface dislocations tend to dissociate, leading to short intrinsic stacking fault (ISF) facets that extend from the interface plane. Rittner and Seidman also revealed that if the delocalization of the interface is severe, the structural units may not change continuously between two favored boundaries, requiring several variations of a given structural unit to describe the interface geometry. Molecular statics calculations presented in Section 3 will show several examples of each type of in-

terface. Despite these limitations of the SUM, it is clear from many previous works that grain boundaries between two crystalline solids still have a repeating structure that can be identified over the length of the interface (even if it is extremely complex due to the dissociated nature of the interface structural units for example). Hence, the interface structure is not random or amorphous.

Disclinations were originally conceived as rotational lattice defects to complement dislocations in the classic work of Volterra [61] and have been used as a component in the description of the structure of grain boundary interfaces in crystalline materials [62,63]. Disclinations contribute to lack of closure over a Burgers circuit manifested by gradients of lattice curvature. In contrast, closure deficiencies due to dislocations arise from the first-order gradient of the deformation gradient. Tilt grain boundaries are closely associated with wedge disclinations because the Frank vector of the wedge disclination and the misorientation axis of the tilt boundary coincide, as shown in Fig. 3(g). Unlike dislocations, the displacement field around a disclination diverges and the stress field of a disclination dipole diverges with the separation of the dipole; thus, disclinations are commonly observed in closely spaced dipole or quadrupole configurations that effectively “screen” the divergent stress field [64]. The spacing between partial disclinations in dipole or quadrupole formations is defined as the dipole arm length. More recent work has combined the structural unit model with Li’s disclination-based description of the structure and energy of high-angle grain boundaries [65–68]. The disclination-structural unit model (DSUM) [65–68] identifies the junction between neighboring dissimilar structural units as a partial wedge disclination. The DSUM theory leverages the fundamental assumption in the SUM that non-favored boundaries consist of alternating regions of different structural units, each of which has a defined misorientation angle characteristic of a specific favored boundary, as shown in Fig. 3(h). The strength of each partial wedge disclination is calculated from the misorientation angle associated with each structural unit, for example $\omega = \pm(\theta_2 - \theta_1)$. The length of the disclination dipole arm is equivalent to the size of one of the structural units, which is related to the repeating period of the interface, L_p . Commonly, the minority structural unit (structural unit that appears less frequently) is represented as the disclination dipole, as shown in Fig. 3(i). Note that favored high-angle boundaries cannot be described in terms of disclination dipoles because the misorientation angle of the interface, θ , is equal to the misorientation angle associated with each structural unit, θ_1 or θ_2 . The DSUM is capable of predicting the interface energy as a function of misorientation for the complete range of $\langle 100 \rangle$ tilt boundaries in FCC metals [65]. Thus, it appears that the minimum energy structure of general high-angle boundaries can be described by repeating structural units associated with favored boundaries, connected by disclination dipoles to account for additional adjustments in misorientation at the boundary. Disconnections [69] may also be incorporated in the interface description to account for steps or other dislocations that create offset within the boundary. The equivalent dislocation representation of these disclination dipoles (in terms of discrete sets of Shockley partial dislocations) remains to be established, but it appears that they can be expressed in terms of general Somigliana dislocations [70]. In general, disclinations may be regarded as lattice defects that assist in accommodation of incompatibility between adjacent lattices. Results presented here show that disclination structural units deform as dislocations are nucleated, incorporating the change of the partial dislocation content of the boundary. In Section 6 we explore a more

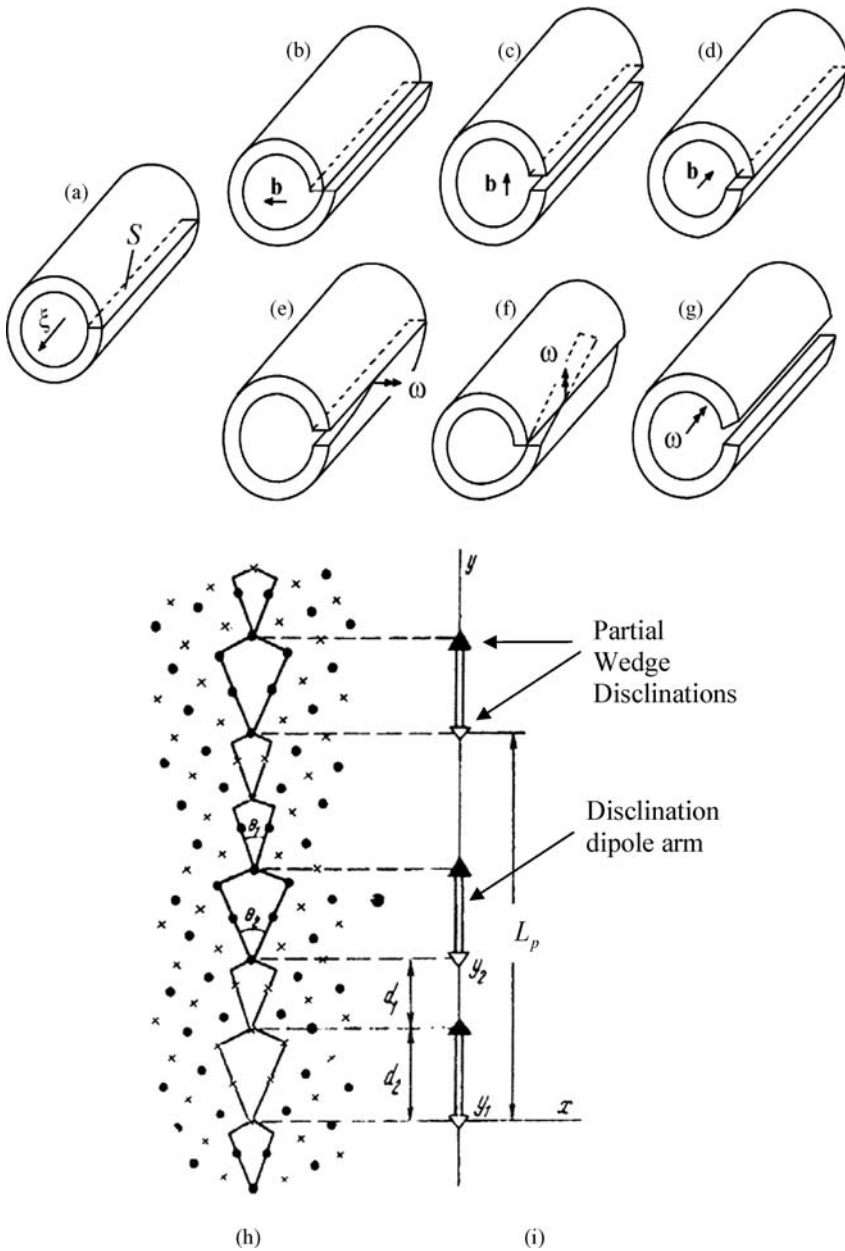


Fig. 3. Volterra's defects: (a) reference cylinder with defect line ξ and cut surface S ; (b, c) edge dislocations and (d) screw dislocation with Burgers vector \mathbf{b} ; (e, f) twist disclinations and (g) wedge disclination with Frank vector ω . A tilt grain boundary interface composed of two different structural units is shown in (h), with the disclination structural unit model representation appearing in (i); (h) and (i) reprinted from [68] with permission of the editorial board of *The Physics of Metals and Metallography*; © 1990 Springer.

precise concept of “disconnection” for describing general boundaries and boundaries that have experienced dislocation emission. We further comment on the issue of incorporating disclinations along with dislocations within the kinematics of defect field theory.

1.3. Modeling dislocation nucleation

The homogeneous nucleation of dislocations in perfect single crystals is a result of strain localization at the elastic limit, which signifies the onset of inelastic behavior [71]. Classically, stress-based criteria have been used to define the initiation of defects in crystalline materials, such as the critical resolved shear stress (CRSS). These criteria envision the CRSS as a material property which characterizes the magnitude of the projected stress state necessary to cause slip. Although this type of approach greatly simplifies the analysis of inelastic material behavior and may be quite accurate with respect to slip of pre-existing dislocations within a crystalline lattice, recent computational evidence indicates that the classical CRSS approach is not sufficient to model dislocation *nucleation* in metallic crystalline materials. For example, Ogata et al. [72] used *ab initio* calculations to show that stress components acting on the slip plane in non-glide directions play a strong role on the critical shear stress required for dislocation nucleation. Specifically, they find that compressive stresses acting normal to the slip plane or within the slip plane perpendicular to the slip direction can increase or decrease the critical shear stress for nucleation. Complementary results have been attained by Tschopp et al. [73] who studied the homogeneous nucleation of dislocations during uniaxial tensile deformation via molecular dynamics simulations. In particular, Tschopp et al. reported that the stress normal to the slip plane plays a commanding role in the nucleation process for copper single crystals. Precise relationships between the non-glide direction stress components and the stress required for dislocation nucleation are discussed in greater detail in Section 5. Results of this ilk have motivated the development of more advanced nucleation criteria, such as that by Zhu et al. [74] which is based on bifurcation analysis of the elastic instability in FCC crystals. Zhu et al. showed that the elastic bifurcation criterion is superior with respect to the accuracy of the predicted nucleation site and the slip character of the dislocation.

Molecular dynamics simulations can also serve as an effective tool to analyze heterogeneous dislocation nucleation and other related inelastic mechanisms from grain boundaries in nanocrystalline (NC) materials [9–12,20–37]. For example, molecular dynamics (MD) has been utilized to investigate the critical grain size associated with the transition between dislocation emission-mediated and GB-mediated deformation modes, which corresponds to the peak strength in FCC materials [11]. Above the critical grain size, MD simulations have shown that partial dislocation nucleation occurs at the grain boundaries and is often accompanied by atomic shuffling or other structural rearrangement within the GB plane [29,31]. For example, Schiotz [12] studied the formation of dislocation pileups at GBs in nanocrystalline Cu samples with grain sizes larger than 15–20 nm. Below the critical grain size, MD simulations have shown that GB sliding becomes the dominant deformation mechanism [10], giving rise to grain rotation. For example, Van Swygenhoven and Derlet [26] reported that GB sliding is triggered by atomic shuffling and stress-assisted

free volume migration from triple junctions. At very small grain sizes, MD simulations in their work showed that the emission of dislocations from GBs was limited.

It is clear from the literature that dislocation nucleation in NC materials involves a number of complex and interrelated mechanisms. The combined tilt and twist character of grain boundaries and the inclination of the boundary plane with respect to the tensile axis complicates the analysis of the role of specific GB structures in NC simulations. In addition, different boundaries may nucleate and emit dislocations at different stresses in NC simulations; thus, it becomes very difficult to separate out the individual effects of GB structural units on dislocation nucleation. An alternative method to study the role of specific grain boundaries in dislocation nucleation is to use bicrystal simulations (cf. [16–19]). This allows precise control of the grain boundary degrees of freedom. In this work, both symmetric and asymmetric tilt grain boundaries are examined. Symmetric tilt grain boundaries facilitate the analysis of a wide range of structures for a given misorientation axis by varying the misorientation angle between the adjoining lattices. Moreover, the lattice symmetry about the grain boundary plane generates well-defined structures and simplifies the analysis of dislocation nucleation at these boundaries. Asymmetric tilt boundaries also present an interesting case for studying dislocation nucleation behavior because of the faceted structure and dissimilar adjoining crystal orientations with different Schmid factors [15]. Bicrystal atomistic simulations are a valuable tool for examining the relationship between grain boundary structure and dislocation nucleation from boundaries.

2. Atomistic simulation methodology

Atomistic simulation refers to a suite of computational techniques used to model the interaction and configuration of a system of atoms. In this work, the term “atomistic simulation” will pertain to either molecular statics (MS) in which energy minimization is used to solve for a local minimum energy configuration or molecular dynamics in which Newton’s 2nd Law of Motion, which may be augmented by additional terms to control the dynamics of the system, is integrated numerically to solve for the trajectories of a set of atoms within a simulation cell. A brief overview of the atomistic simulation techniques utilized in this work is provided in this section. The reader is directed towards more detailed and comprehensive reviews in texts by Allen and Tildesley [75] and Haile [76].

In the atomistic framework, each atom is represented as a point mass in space while an interatomic potential is specified to provide a model for the potential energy of a system of atoms. Commonly, the total potential energy of the system is written solely as a function of the positions of the atomic nuclei. This simplification avoids having to specifically account for the motion and interaction of the individual electrons. Since interatomic forces are conserved, the force on a given atom, \mathbf{F}^i , is related to the interatomic potential, U , through the gradient operator, i.e.,

$$\mathbf{F}^i = -\frac{\partial U(\mathbf{r}_N)}{\partial \mathbf{r}^i}. \quad (1)$$

Here, \mathbf{r} is the atomic position vector. In this section, superscripts denote variables assigned to individual atoms, while subscripts denote variables associated with sets of atoms, directions or at specific time steps. Thus, \mathbf{r}_N represents the position vectors for the system of

N atoms while \mathbf{r}^i is the atomic position vector for the i th atom. The choice of the interatomic potential, U , depends on the material system of interest. For example, to study FCC transition metal systems, the embedded-atom method (EAM) is commonly employed. The details of the EAM and the accuracy of the selected interatomic potentials in this work with respect to material properties critical to the nucleation and motion of dislocations will be discussed in Section 2.4.

2.1. Molecular statics

In this work, it is critical that the initial interface structures are described accurately in order to draw quantitative conclusions regarding the role of individual structural features in the deformation process. Thus, the initial bicrystal interface structures are obtained using molecular statics calculations which utilize an energy minimization technique. In general, numerical techniques, such as steepest decent or the conjugate gradient method, can be used to find a local minimum in the potential energy surface, as long as $U(\mathbf{r}_N)$ is continuous, contains a lower bound and the gradient U' can be computed [77]. Recall from eq. (1) that the negative of the gradient of the potential energy U is the force vector. A local minimum in the potential energy surface is found by setting the gradient equal to zero and solving for the appropriate values of \mathbf{r}_N . In this work, energy minimization is achieved using a nonlinear conjugate gradient algorithm which incorporates the secant method to determine the appropriate step length and the Polak–Ribiere formulation for the search direction [77].

Unfortunately, there is no algorithm that guarantees determination of the global minimum energy configuration. Thus, this work follows previous bicrystal energy minimization calculations (cf. [52,60,78]) as a number of initial starting “positions” are used to increase the probability that the global minimum energy configuration is attained. One accomplishes this systematically by removing atomic layers at the interface or by manually translating the lattice regions normal and parallel to the interface plane and allowing the energy minimization procedure to rearrange the interface atoms as necessary (resolving the microscopic degrees of freedom of the grain boundary). For example, to access the minimum energy GB structures for the asymmetric tilt grain boundaries (ATGBs) discussed in Section 3.2, energy minimization calculations utilize over 2700 initial configurations with different in-plane rigid body translations and atom deletion criterion [79]. Tschopp and McDowell found that some asymmetric tilt grain boundaries have accessibilities [52] as low as 0.1%. To add an additional measure of certainty to the energy minimization calculations, we compare the interface structures obtained in this work to both high-resolution transmission electron microscopy images and electronic structure calculations of bicrystal configurations when available in the literature (cf. [80–85]). The methodology used in this work yields GB energies that are in agreement with both calculated and experimentally measured energies for $\Sigma 3$ ATGBs [82,83]. Moreover, the GB structures associated with these energies are also in agreement with several experimentally observed high-resolution TEM images of $\Sigma 3$ ATGB structures with 9R configuration (e.g., in Cu [83]). Further details of the simulation methodology used to obtain ATGB structures are given in Tschopp and McDowell [79].

2.2. Molecular dynamics

In this work, molecular dynamics simulations are performed to study the tensile deformation of grain boundary interfaces on the nanoscale. In the molecular dynamics method, the evolution of atomic positions is described using Newton's 2nd Law of Motion,

$$\dot{\mathbf{p}}^i = \mathbf{F}^i = m\dot{\mathbf{v}}^i, \quad (2)$$

where

$$\dot{\mathbf{r}}^i = \frac{d\mathbf{r}^i}{dt} = \frac{\mathbf{p}^i}{m}. \quad (3)$$

Here, m is the mass, \mathbf{p}^i is the momentum and \mathbf{v}^i is the velocity of the i th atom. The “dot” signifies the first derivative with respect to time. Eqs (2) and (3) represent the equations of motion for a system of atoms that is isolated from the environment (microcanonical ensemble). Of course, the vast majority of problems in the mechanics and materials science community require that the system interact with the surrounding environment. One method to accomplish this in the MD framework is to introduce the concept of an extended system [86]. Essentially, Newton's equations of motion are augmented and coupled to additional differential equations that characterize the relationship between the system and the environment. For example, to model the atomic trajectories within the constant pressure, constant temperature (NPT) ensemble, the following set of equations has been proposed [87],

$$\begin{aligned} \dot{\mathbf{r}}^i &= \frac{\mathbf{p}^i}{m} + \eta(\mathbf{r}^i - \mathbf{R}_0), \\ \dot{\mathbf{p}}^i &= \mathbf{F}^i - (\eta + \zeta\mathbf{I})\mathbf{p}^i, \\ \dot{\zeta} &= v_T^2 \left(\frac{T}{T_0} - 1 \right), \\ \dot{\eta} &= \frac{v_P^2}{NkT_0} V(\sigma - \mathbf{P}_0), \\ \dot{\mathbf{h}} &= \eta\mathbf{h}. \end{aligned} \quad (4)$$

Here, \mathbf{R}_0 is the center of mass of the system. The isobaric friction coefficient, η , is a function of the desired pressure or stress, \mathbf{P}_0 , Boltzmann's constant, k , and the constant pressure damping coefficient, v_P . The thermodynamic friction coefficient, ζ , is a function of the thermal reservoir temperature, T_0 , and the thermostating rate, v_T . The boundaries of the system are defined by a set of vectors, \mathbf{h} , that are aligned along the edges of the periodic unit cell. Melchionna et al. [87] showed that the equations of motion in eq. (4), which are derived from earlier versions by Nose and Hoover [88,89], correctly reproduce the NPT distribution function. Further, since the Melchionna et al. equations do not require scaling of the atomic positions or velocities to reproduce the NPT ensemble, they may be easily incorporated into the standard framework of a MD code.

2.3. Virial stress

The physical interpretation of stress in an atomistic system is one that has been argued from different points of view in the literature over the past thirty years [90–95]. Mathematically, the virial stress may be computed by first using the volume around a given atom, Ω^i , to form a point-wise measure of stress, i.e.,

$$\Pi^i = \frac{1}{\Omega^i} \left[\frac{1}{2} \sum_i \sum_{i \neq j} \frac{U'}{r_{ij}} r_{\alpha}^{ij} r_{\beta}^{ij} - \sum_i m \mathbf{v}^i \mathbf{v}^i \right], \quad (5)$$

with

$$\Omega^i = \frac{\lambda^3}{4}. \quad (6)$$

In eq. (5), r^{ij} is the distance between atoms i and j ; r_{α}^{ij} and r_{β}^{ij} are the components of the total distance in the α and β directions. The “prime” denotes the first derivative with respect to atomic position. In eq. (6), λ is the lattice parameter. Eq. (6) is derived as an approximation of the volume around an atom in a FCC lattice. The point-wise measure of stress, Π^i , does not have any physical interpretation unless it is averaged over a “representative” number of atoms, i.e.,

$$\sigma = \frac{1}{N} \sum_{i=1}^N \Pi^i. \quad (7)$$

Zimmerman et al. [95] investigated the concept of a representative number of atoms using two expressions for stress in an atomistic system (one of which is the stress derived from the virial theorem). They reported that for situations of non-zero deformation at finite temperature, fluctuations exist in the virial stress calculation when the summation is performed over small volumes around an arbitrary point within the simulation cell, i.e., when the calculation is not performed within the thermodynamic limit. As the size of the averaging region increases, the fluctuations in the stress calculation decrease. They also find that the fluctuations in the stress decrease at a faster rate if both spatial and temporal averaging is performed.

Several authors in the literature have attempted to develop expressions for stress in an atomistic system that are defined for a spatial point at an instant of time from the equation for balance of linear momentum for a dynamic continuum [92,94]. From this perspective, Zhou [94] showed that the virial stress expression is unable to handle simple cases of rigid body translation in atomic systems. More importantly, Zhou also showed that the point-wise virial stress expression in eq. (5) violates classical conservation of linear momentum. Zhou argued that in a dynamically deforming atomic system, the stress should be a function of only the force between particles in order to maintain equivalence with the classical definition of the Cauchy stress and asserts that the kinetic contribution to the stress is already accounted for through the force term and that the kinetic contribution to the point-wise virial stress is incorrect if stress is to be interpreted as a force interaction between material points. It is beyond the scope of this work to provide a full review and discussion of stress calculations in atomistic systems. In this work, the kinetic contribution to the virial stress is

retained, understanding that there are the possible ambiguities with regard to conservation of linear momentum if the virial expression is used to obtain highly localized measures of stress. Note that for solids, the kinetic energy term is small as compared with the inter-atomic force term. This observation is particularly true when calculations are performed at relatively low temperatures (10 and 300 K) and when the system is subjected to an external deformation. Furthermore, in this work, stress is averaged over a large volume around the region of interest to reduce the fluctuations in the virial stress response [95]. However, the stresses reported in this work are not time averaged, i.e., they are reported at defined instants in time during the simulation.

2.4. EAM potentials

Daw and Baskes [96,97] developed the embedded-atom method to describe atomic bonding in metallic systems. In the EAM, each atom is viewed as being embedded in the background electron density provided by neighboring atoms. Thus, the potential energy of a set of atoms is taken as the summation of the pair interaction energy between nuclei of atoms i and j and the embedding energy as a function of the local background electron density around i th atom. Since the background electron density is a local quantity, the embedded-atom method is applicable for examining systems with crystalline defects, such as dislocations and grain boundaries. However, an important assumption in the derivation of the EAM expression is that the electron cloud around each atom is spherical in shape. Thus, it is assumed that bond orientation is not important in the description of the potential energy. This approximation is valid for FCC crystal structures with either nearly empty or nearly full d -bands [98]; however, the EAM struggles to accurately describe systems where directional bonding is important, such as BCC, HCP and nonmetallic materials.

The Mishin et al. EAM interatomic potentials for aluminum [99] and copper [100] are utilized in this work. These potentials are numerically fit to give many correct physical properties for Cu and Al, including the equilibrium lattice parameter, the cohesive energy, elastic constants, and the vacancy formation energy. To model grain boundary structure and dislocation nucleation, Van Swygenhoven and colleagues [32,34] argued the importance of both the intrinsic and unstable stacking fault energies, γ_{SF} and γ_{US} . The intrinsic stacking fault energy is critical for atomistic simulations of fracture and deformation because it defines the width of partial dislocation dissociation; this not only affects full and partial dislocation emission, but also the grain boundary structure in crystalline materials. The unstable stacking fault energy is related to the barrier for dislocation nucleation events [101]. For NC materials, Van Swygenhoven et al. proposed that the transition between partial and full dislocation emission can be correctly understood in terms of the generalized planar fault energy curve, which considers both the intrinsic and the unstable stacking fault energies. They find that the ratio of intrinsic to unstable stacking fault energies is a critical parameter for determining whether a trailing partial dislocation is emitted from the GB in nanocrystalline materials; as this ratio approaches unity, the energy barrier for creating a trailing partial dislocation is very low. Mishin et al. reported excellent agreement between the intrinsic stacking fault energy computed with their Cu and Al potentials as compared with experimental and *ab initio* calculations. Moreover, an analysis by Boyer et al. [102]

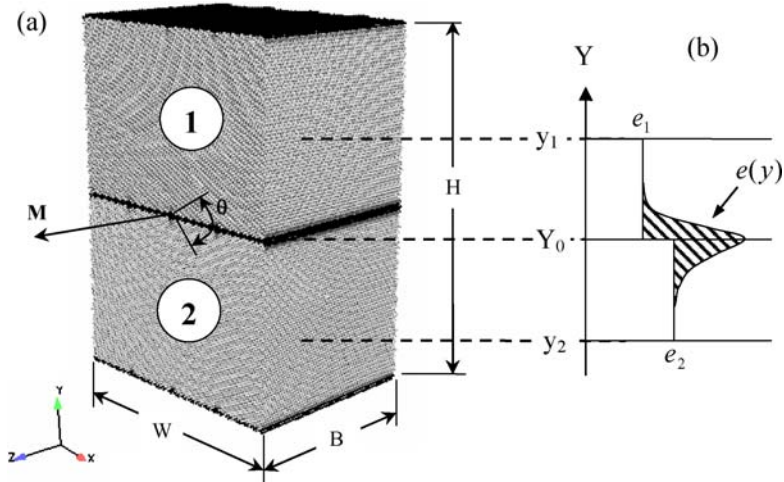


Fig. 4. (a) Three-dimensional periodic bicrystal computational cell employed in this work. Crystal regions 1 and 2 are separated by two interfaces: one at the center of the cell and one periodic interface at the lower/upper cell bounds. The misorientation axis, M , and misorientation, θ , are also shown. (b) Schematic illustration of the excess interface energy calculation.

and Zimmerman et al. [103] of stress–displacement, atomic relaxation, and the γ -surface for $\{111\}\{11\bar{2}\}$ shear indicated that the Mishin et al. Cu and Al potentials capture the essential characteristics of deformation, including the unstable stacking fault energy, in line with *ab initio* electronic structure calculations. Thus, the EAM potentials utilized in this work are considered sufficient to model the structure of symmetric and asymmetric tilt grain boundaries as well as the nucleation of dislocations from these boundaries.

2.5. Bicrystal simulation geometry

In this work, we develop bicrystal interface models using a combination of molecular statics (energy minimization) and molecular dynamics simulations. An example bicrystal interface model is shown in Fig. 4. For symmetric tilt grain boundaries, the interface misorientation is created by a symmetric rotation, θ , of opposing lattice regions around a misorientation axis, M . For asymmetric tilt grain boundaries, the misorientation angle remains fixed at a defined θ and the two lattices are rotated about the misorientation axis by the same angle, such that crystal region 1 and crystal region 2 (Fig. 4) are now asymmetric with respect to the boundary plane. For boundaries with a $[001]$ misorientation axis, the interface misorientation angle is measured using the $[100]$ direction as the reference (0°). For boundaries with a $[1\bar{1}0]$ misorientation axis, the interface misorientation angle is measured using the $[001]$ direction as the reference (0°). One of the inherent limitations of the atomistic method is that computational resources often demand that systems are limited to relatively small numbers of atoms. While the study of nanoscale surface effects is extremely important, the goal of this work is to examine atomic scale behavior that is rep-

representative of what would occur in a bulk sample with micro or nanoscale grain structure. Thus, periodic boundary conditions are used in all directions (X , Y and Z) to eliminate the influence of free surface effects. The bicrystal interface model dimensions are defined accordingly to properly enforce this boundary prescription.

Unfortunately, while periodic boundary conditions remove the effects of free surfaces, they impart image constraints on the system which must be taken into consideration when simulating defect behavior with long-range interactions. Such long-range interactions are characteristic of dislocations and grain boundaries with asymmetric structure, as will be modeled in this work. Specifically, the use of periodic boundary conditions in the Y -direction introduces a second interface into the model, which in turn gives rise to forces on dislocations. For symmetric tilt boundaries, the stress field decreases exponentially away from the interface [15]. In the symmetric case, the spacing between interfaces, $H/2$, is sufficiently large to minimize effects on nucleation of the first dislocation. However, this is not case for asymmetric tilt boundaries or symmetric boundaries with asymmetric interface structure. Furthermore, as these calculations will show, the nucleation of dislocations causes distortion in the interface structure. This is particularly true in the case of dissociated interfaces, where partial dislocation emission is inherent to the interface structure. If the interface distortion is idealized as a single dislocation positioned at the nucleation point [104], the magnitude of the shear stress on the primary slip planes due to the distorted boundary at a distance $H/2$ away from the interface is generally less than 10% of the ideal shear strength derived from first-principles calculations [72]. Accordingly, we consider the dimensions of the periodic model suitable for the study of dislocation nucleation phenomena at early stages. Moreover, because they employ periodic boundary conditions, the present bicrystal simulations are most appropriate for studying grain boundary structure and dislocation nucleation mechanisms, leaving the study of long-range field interactions of dislocations in a lattice with a boundary to other approaches, such as the CADD method [105,106] or matching atomistics near the boundary with a quasicontinuum far-field domain [107,108].

After the minimum energy configuration is attained via molecular statics calculations as discussed in Section 2.1, isobaric–isothermal molecular dynamics simulations are used to equilibrate the bicrystal interface model to a pressure of 0 bar and a temperature of either 10 or 300 K. The nucleation of dislocations at both temperatures will be discussed in Section 4. During this thermodynamic equilibration, the Melchionna et al. isobaric–isothermal equations of motion [87] govern the dynamics of the system. Upon completion of the equilibration process, molecular dynamics simulations are used to study the deformation of each interface model in uniaxial tension, which is applied normal to the interface plane (Y -direction). A constant strain rate of 10^9 s^{-1} is introduced by decoupling the vector which describes the dimensions of the periodic cell from the equations of motion in the loading direction and extending the length of this vector during the simulation [109]. Essentially, the time rate of change of the periodic cell length is prescribed in the loading direction in accordance with a desired strain rate. The motions of the boundaries in the transverse directions (X and Z) are calculated from the current and prescribed system stresses using the Melchionna et al. equations of motion. For all simulations in this work, the boundaries perpendicular to the interface plane are specified as stress-free. The 10^9 s^{-1} strain rate was chosen for its computational efficiency vs. lower strain rates and

to avoid the detrimental effects (e.g., inducing shock waves within the computational cell) that are introduced at higher strain rates. Atomistic simulations of grain boundary dislocation nucleation in uniaxial tension and compression under quasistatic loading conditions (as applied in Ref. [110]) have shown similar stress–strain responses and dislocation nucleation mechanisms to those of the dynamic strain rate used here. Therefore, this strain rate is deemed sufficient for investigating dislocation nucleation from grain boundaries.

3. Structure and energy of tilt grain boundaries in Cu and Al

As discussed in Sections 1 and 2, this work focuses on the nucleation of dislocations from symmetric and asymmetric tilt bicrystal interfaces with the aim of developing correlations between grain boundary structure and dislocation nucleation. Accordingly, it is critical that a thorough understanding of the underlying interface structure as a function misorientation or inclination angle is established. Of particular importance are natural connections between interface structure in symmetric and asymmetric boundaries. For example, this work reports that the asymmetry between adjoining lattice regions results in nanoscale faceting along the grain boundary plane. The structure of the facets and the structural features adjoining the facets in ATGBs can be correlated to the structural features observed in symmetric tilt grain boundaries with similar misorientation.

3.1. Calculation of interface energy

Interface energy is calculated by considering the energy at the boundary between the two crystalline regions that is in excess of the intrinsic energy of the bulk lattices [111–113]. This concept is schematically illustrated in Fig. 4(b) and is mathematically expressed as

$$\gamma^{\text{int}} = \int_{y_1}^{y_2} e(y) \, dy - e_1(y_1 - Y_0) - e_2(Y_0 - y_2). \quad (8)$$

In eq. (8), $e(y)$ is the energy profile normal to the interface, e_1 is the bulk energy in region 1 (upper crystalline region) and e_2 is the bulk energy in region 2 (lower crystalline region). The vertical locations Y_0 , y_1 and y_2 are defined schematically in Fig. 4(b). This definition does not require the introduction of an interface volume or region around the bicrystal boundary as long as y_1 and y_2 extend beyond the region which is distorted by the planar defect. Note that this work specifically addresses homophase interfaces; thus, the bulk energies of crystal regions 1 and 2 are identical after energy minimization and a rigorous separation of the energy profile normal to the interface into two regions is not necessary. Regardless, eq. (8) is posed in the general form to emphasize that the calculation of excess interface energy can be extended to heterophase boundaries.

Slight modifications are required in order to apply eq. (8) to discrete atomistic systems. Notably, the integral of the energy profile must be replaced by a summation over a set of atoms within each crystalline region, i.e.,

$$E^{\text{int}} = \sum_{i=1}^{N_1} [e_i - e_1] + \sum_{i=1}^{N_2} [e_i - e_2]. \quad (9)$$

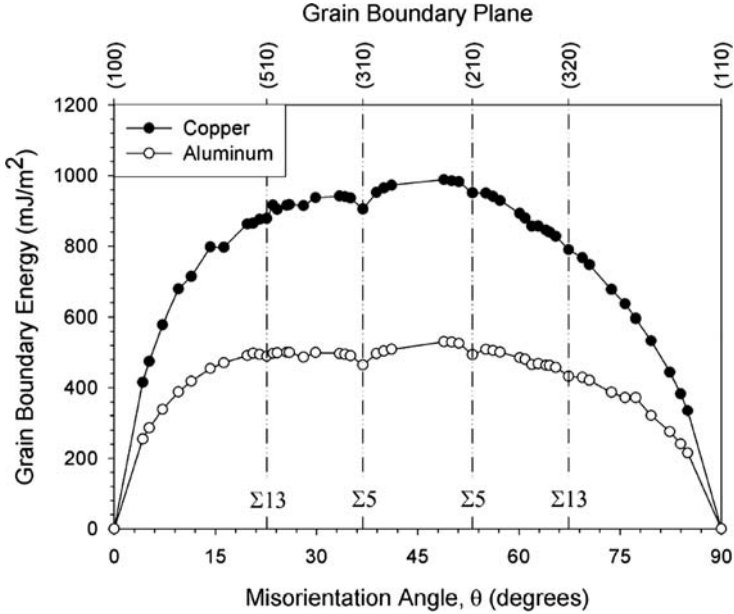


Fig. 5. Bicrystal interface energy for copper and aluminum tilt [001] interface models.

Here, N_1 and N_2 are the number of atoms in regions 1 and 2, respectively. The bulk energies, e_1 and e_2 , are determined by averaging the e_i of a group of atoms positioned sufficiently far away from the interface such that the presence of the boundary is not detected. Using e_1 and e_2 , an excess energy is computed for every atom within the interface model; the sum of these excess energies is defined as the total interface energy. In this work the bulk energies of regions 1 and 2 are identical after energy minimization ($e_1 = e_2 = e$); thus, the interface energy can be computed by summing the excess energy over all atoms (with appropriate treatment of the mirror image interface), which avoids the explicit assignment of atoms to either crystal regions 1 or 2.

3.2. Symmetric tilt grain boundaries

3.2.1. Interface energy

Fig. 5 shows interface energy versus misorientation angle for symmetric tilt [001] boundaries in both copper and aluminum. The energy of the aluminum $\Sigma 5$ (310) 36.9° interface is calculated as 465 mJ/m^2 , while the energy of the aluminum $\Sigma 5$ (210) 53.1° interface is calculated as 494 mJ/m^2 . Both values are very close to those reported by Mishin et al. of 467 and 495 mJ/m^2 , respectively [99]. In Fig. 5, small cusps appear in the energy–misorientation angle relationship at certain misorientations, which correspond to the $\Sigma 5$ (310) 36.9° and $\Sigma 5$ (210) 53.1° boundaries. Note that each of these boundaries is considered favored in the structural unit model for the [001] misorientation axis [58]. Other low-order Σ boundaries show only minor variation in the interface energy, corresponding

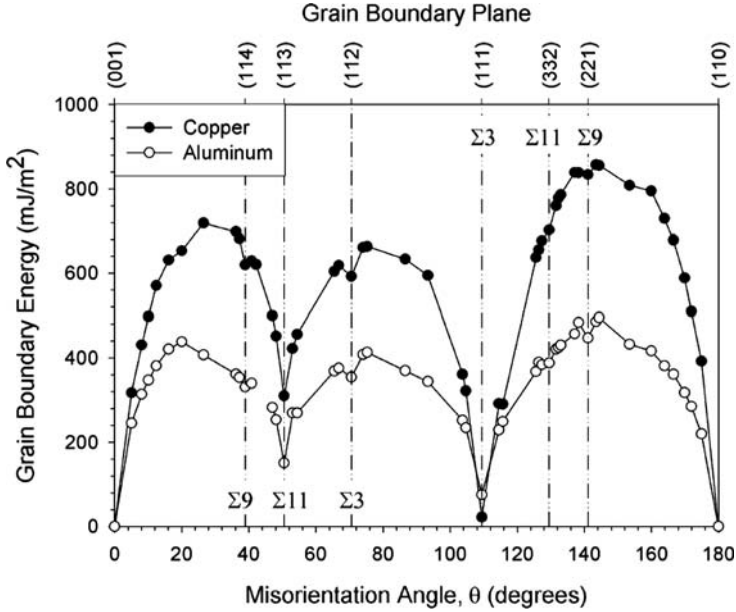


Fig. 6. Bicrystal interface energy for copper and aluminum tilt $[1\bar{1}0]$ interface models.

to small inflection points in the energy curve. Fig. 5 also shows a slight asymmetric character. While the interface energy appears to reach a maximum value between each of the $\Sigma 5$ boundaries (approximately around 45°), the energy–misorientation angle relationship does not possess mirror symmetry across the 45° centerline. Each of these observations is in agreement with those presented by Wolf [78] for other FCC metals (Cu, Ni and Au).

Fig. 6 shows interface energy versus misorientation angle for symmetric tilt $[1\bar{1}0]$ boundaries in copper and aluminum. Symmetric tilt grain boundaries (STGBs) created by rotations around the $[1\bar{1}0]$ axis show a more pronounced cusp behavior than boundaries formed around the $[001]$ misorientation axis. In both copper and aluminum, prominent cusps appear in the energy–misorientation angle relationship at the $\Sigma 3$ (111) 109.5° and $\Sigma 11$ (113) 50.5° boundaries. The energy of the $\Sigma 3$ (111) 109.5° boundary is calculated as 22 mJ/m^2 in copper and 75 mJ/m^2 in aluminum. Other low-order Σ boundaries show only small reductions in the interface energy. Furthermore, Fig. 6 shows a pronounced asymmetric character. While the $\Sigma 3$ (111) 109.5° and $\Sigma 11$ (113) 50.5° boundaries have very low interface energies, their reciprocal boundaries, $\Sigma 3$ (112) 70.5° and $\Sigma 11$ (332) 129.5° , have much larger interface energies by comparison.

3.2.2. Interface structure

Fig. 7 shows a detailed view of several $\Sigma 5$, $\Sigma 13$ and $\Sigma 17a$ interface structures in copper after the energy minimization procedure. Each of these interfaces is created by a symmetric tilt rotation around the $[001]$ misorientation axis. The viewing direction is along the $[001]$ crystallographic direction (Z-axis) and atom positions are projected into the X–Y plane for clarity. Atoms are shaded by their respective $\{001\}$ atomic plane in order to identify the

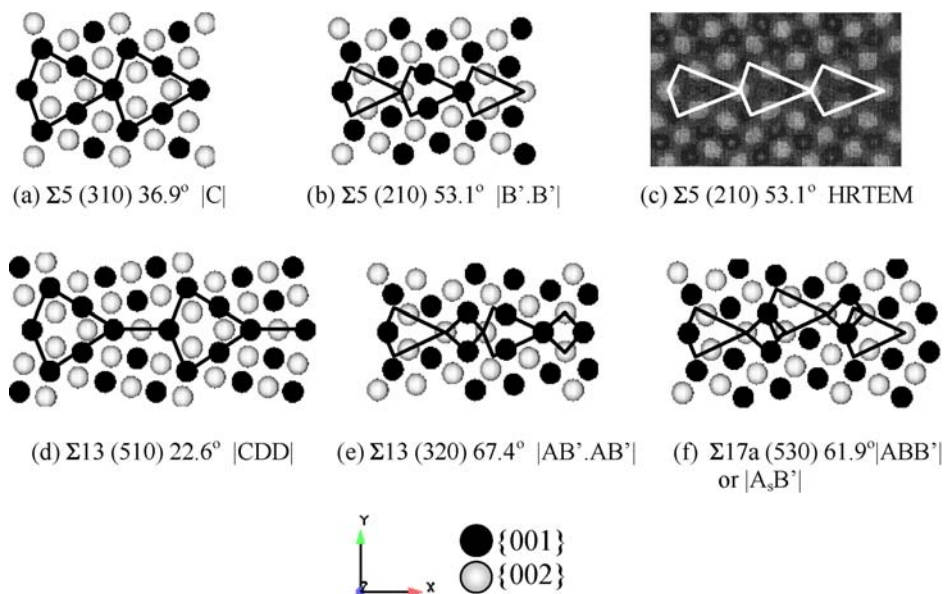


Fig. 7. Bicrystal interface structures for copper [001] interface models. The structural unit model notation is given. Figure (c) is reprinted from [113] with permission; © 1999 Trans Tech Publications.

interface structural units. The $\Sigma 5$ (310) 36.9° interface in Fig. 7(a) is composed of C type structural units along the entire length of the interface. Similarly, the $\Sigma 5$ (210) interface in Fig. 7(b) is composed entirely of B' structural units. The B' structural unit is a slightly modified version of the B structural unit originally proposed by Sutton and Vitek [55] that is shown via molecular dynamics calculations to have a slightly lower energy in FCC materials [65]. The configuration of the B' structure has also been confirmed experimentally in copper via high-resolution transmission electron microscopy (HRTEM) as shown in Fig. 7(c) [114]. Bicrystal boundaries with non-favored misorientations are composed of two (or more) different types of structural units. For example, the structure of the $\Sigma 13$ (510) boundary in Fig. 7(d) is composed of one C unit and two D units per interface period, with the SUM notation |CDD|. The vertical "bars" denote one period of the interface structure. Similarly, the $\Sigma 13$ (320) boundary in Fig. 7(e) is composed of two A units and two B' units per interface period, with the SUM notation |AB'.AB''|. Here, the "dot" signifies that the structural unit has shifted from the {001} lattice plane to the neighboring {002} plane. Sutton and Vitek [55] define this type of interface structure as being "centered."

The $\Sigma 17a$ (530) interface in Fig. 7(f) shows a slightly different behavior. The minimum energy configuration of this boundary is not mirror symmetric about the interface plane, as in the case with the other low-order CSL boundaries in Fig. 7. Two representations are proposed to describe the interface structure: |ABB'| or |A_sB'|, the latter of which is shown in Fig. 7(f). The A_s structural unit includes a step in the interface plane between B' structural units. The energy of the |A_sB'| boundary in copper is calculated as 856 mJ/m². This particular misorientation requires several variations of a given structural unit to describe

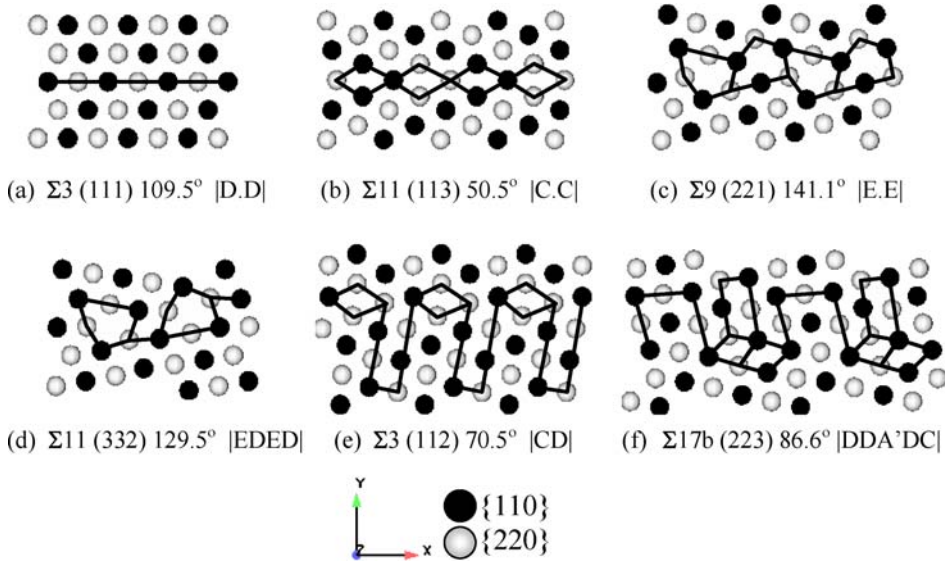


Fig. 8. Bicrystal interface structures for copper $[1\bar{1}0]$ interface models. The structural unit model notation is given.

the interface geometry; hence, the classical SUM is only loosely applicable. Note that by using a different initial configuration during the energy minimization procedure, a mirror symmetric $\Sigma 17a$ (530) interface may be created. This interface has an $|AB'B'|$ structure, which is in agreement with the theoretical prediction using the SUM. However, the energy of this interface is calculated as 906 mJ/m^2 , which is higher than that of the stepped boundary. Thus, the structure of the $\Sigma 17a$ (530) interface shown in Fig. 7(f) is considered the appropriate structure.

Fig. 8 shows a detailed view of several $\Sigma 3$, $\Sigma 9$, $\Sigma 11$ and $\Sigma 17b$ interface structures in copper after the energy minimization procedure. Each of these interfaces is created by a symmetric tilt rotation around the $[1\bar{1}0]$ misorientation axis. The viewing direction is along this same axis, which is aligned with the Z-direction. The structure of each interface is identified by shading atoms by their respective $\{110\}$ atomic plane through the thickness of the interface model, while the structural units outlined are based on those proposed in the literature by Rittner and Seidman [52], who used an EAM potential for nickel for their energy minimization calculations. Three of the boundaries presented in Fig. 8 are considered favored in the structural unit model representation of interfaces [55]. For example, the $\Sigma 3$ (111) 109.5° coherent twin boundary in Fig. 8(a) is composed entirely of D structural units with centered interface structure. Similarly, the $\Sigma 11$ (113) 50.5° interface [Fig. 8(b)] and the $\Sigma 9$ (221) 141.1° interface [Fig. 8(c)] are composed entirely of C and E structural units, respectively. Several of the bicrystal interface structures created by symmetric tilt rotations around the $\langle 110 \rangle$ misorientation axis can be characterized by the structural unit model, even though the interface structures are not mirror symmetric about the interface

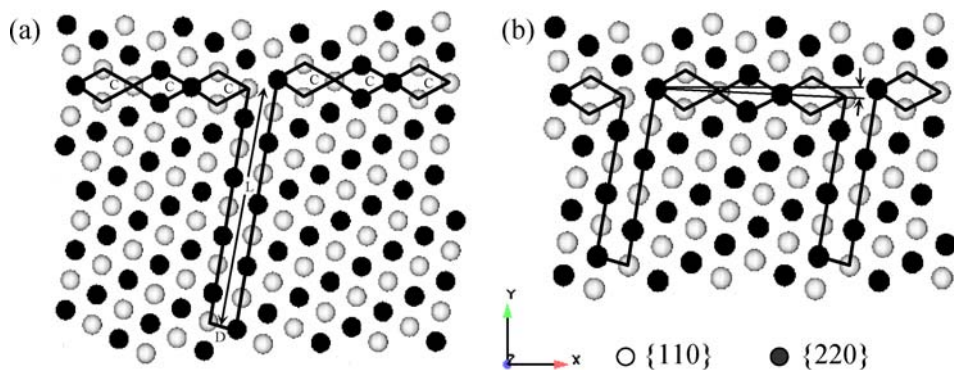


Fig. 9. Bicrystal interface structures for dissociated (a) 53.1° and (b) 59.0° copper $[1\bar{1}0]$ interface models. Reprinted from [17] with permission; © 2007 Elsevier.

plane. For example, the $\Sigma 11$ (332) 129.5° interface in Fig. 8(d) is composed of two E and two D structural units per interface period.

However, several $\langle 110 \rangle$ STGBs show a dissociated interface structure. For example, the $\Sigma 3$ (112) interface in Fig. 8(e) is composed of both C and D type structural units. The C type structural unit is representative of the $\Sigma 11$ (113) 50.5° interface. The D type structural unit is associated with the $\Sigma 3$ (111) 109.5° twin boundary. The D structural unit in this interface lies at the termination of an intrinsic stacking fault that extends from the bicrystal interface. The delocalized structure occurs as a result of the asymmetric dissociation of secondary interface dislocations [60]. For other misorientations, the delocalization of the interface structure can have a more advanced form, such as that for the $\Sigma 17b$ (223) 86.6° interface in Fig. 8(f). Here, energy minimization predicts intrinsic stacking fault facets of various lengths and widths along the interface plane. In addition, at least three structural units are identified using the centrosymmetry parameter [115], including the A' structural unit, which should not exist for this misorientation according to the SUM. Thus, the structural unit model fails to characterize boundaries with dissociated structure because the SUM is unable to predict the length, width or spacing between delocalized structural units. However, images in Fig. 8 and results in the literature clearly show that even highly delocalized interfaces in FCC metallic materials can still be defined in terms of a repeating structure.

The observation of intrinsic stacking fault facets that extend from the interface plane is particularly intriguing, because these facets could potentially play a strong role in the deformation process (since they are in essence pre-nucleated partial edge dislocations). Fig. 9 shows a detailed view of the interface structures for 53.1° and 59.0° $\langle 110 \rangle$ misorientations in copper after energy minimization. Note that neither of these boundaries are considered favored in SUM or have a low-order CSL description. The ISF facet is formed due to the asymmetric dissociation of secondary interface dislocations and is positioned on the $(11\bar{1})$ slip plane in the lower lattice region in Figs 9(a) and 9(b). Rittner and colleagues [52, 60] define the termination of each ISF facet as the D structural unit; the remainder of the boundary is composed of C structural units, which are associated with the $\Sigma 11$ (113) 50.5° favored interface [Fig. 8(b)]. To accommodate the ISF facet, the C structural units are tilted

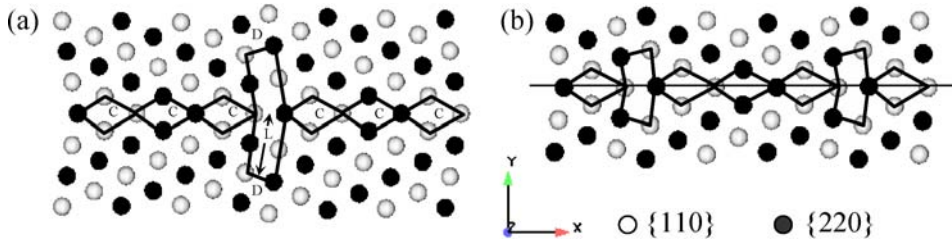


Fig. 10. Bicrystal interface structures for dissociated (a) 53.1° and (b) 59.0° aluminum $[1\bar{1}0]$ interface models. Reprinted from [17] with permission; © 2007 Elsevier.

downward relative to the positive X -axis, as shown in Fig. 9(b). The spacing between ISF facets decreases as the misorientation angle of the interface is increased between 53.1° and 59.0°. Specifically, the 53.1° boundary has 11 C units for each dissociated D unit [the entire boundary is not shown in Fig. 9(a)], while the 59.0° interface has only 3 C units for each dissociated D unit.

Rittner and Seidman [52] also showed that interface structures can vary significantly between materials with appreciably different intrinsic stacking fault energies. Specifically, Rittner and Seidman showed that delocalized structural units do not occur in materials with high stacking fault energies. Each of the interface structures presented in their work showed a mirror symmetric interface configuration for the high ISF energy material. As a result, they concluded that the structural unit model representation of high-angle interfaces becomes more applicable for materials with high ISF energy. Figs 10(a) and 10(b) show that the ISF facet that extends from the 53.1° or 59.0° interfaces is significantly shorter in aluminum, a material with higher stacking fault energy. Furthermore, in aluminum the dissociation of secondary interface dislocations is mirror symmetric on opposing $\{111\}$ slip planes. Specifically, the facet occurs on the $(11\bar{1})$ slip plane in the lower lattice region and on the (111) slip plane on the upper lattice region. Similar to copper, the termination of the ISF facet is identified as the D structural unit, with the remainder of the boundary composed of C structural units, as shown in Fig. 10(a). The spacing between each dissociated facet decreases as the misorientation angle of the interface is increased over the range considered. The same ratio of C:D interface structural units occurs in both copper and aluminum. In aluminum, the C structural units are not distorted by the dissociation of secondary dislocations, i.e., the entire interface is mirror symmetric about the boundary plane, as shown in Fig. 10(b).

Accordingly, energy minimization calculations are performed over the entire range of $\langle 001 \rangle$ and $\langle 110 \rangle$ symmetric tilt boundaries using the Mishin et al. EAM potential for aluminum [99]. All of the aluminum $\langle 100 \rangle$ interface structures presented in Fig. 11 are identical to those presented in Fig. 7. The higher stacking fault energy of aluminum does not appear to affect the interface structures for the low-order CSL boundaries created around the $\langle 001 \rangle$ misorientation axis. The $\Sigma 5$ (310) and $\Sigma 5$ (210) interfaces are composed entirely of C and B' structural units, respectively. Of particular interest is the stepped $\Sigma 17a$ (530) interface in Fig. 11(e). Analogous to that in copper, this boundary does not have a mirror symmetric interface structure. The energy of the $\Sigma 17a$ (530) boundary in aluminum shown in Fig. 11(e) is calculated as 465 mJ/m², while supplemental energy minimization

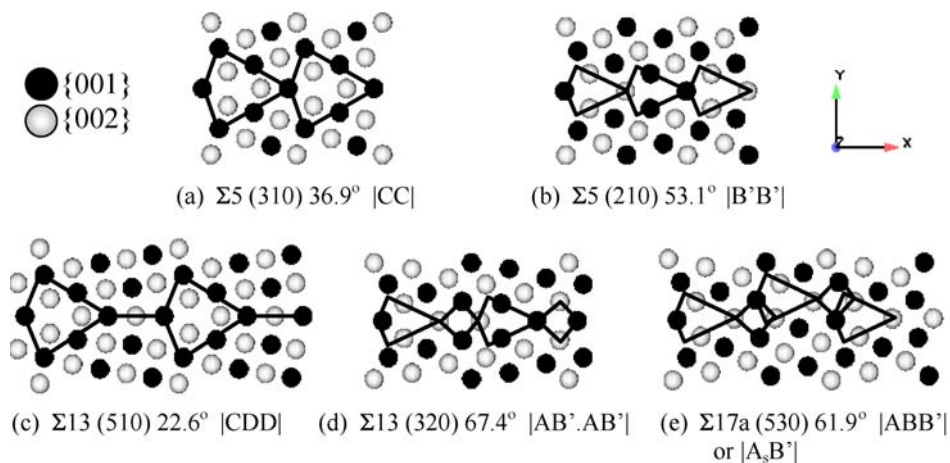


Fig. 11. Bicrystal interface structures for aluminum [001] interface models. The structural units and SUM notation are given.

calculations calculate that a $\Sigma 17a$ (530) interface with a |AB'B'| structure has an interface energy of 493 mJ/m^2 . Thus, the appropriate structure for this boundary is again the stepped interface.

Fig. 12 shows a detailed view of several $\Sigma 3$, $\Sigma 9$, $\Sigma 11$ and $\Sigma 17b$ interface structures in aluminum indicating that many of $\langle 110 \rangle$ STGB structures in aluminum are different than those in copper (Fig. 8). This is due to the difference in intrinsic stacking fault energies between copper and aluminum. It is unclear exactly why the ISF energy affects the interface structure more severely for the $[1\bar{1}0]$ misorientation axis than for the [001] misorientation axis; however, we speculate that it has to do with the orientation of the interface with respect to the primary slip systems. The favored $\langle 110 \rangle$ STGBs in aluminum [$\Sigma 3$ (111), $\Sigma 11$ (113) and $\Sigma 9$ (221)] are identical to those presented for copper, as shown in Figs 12(a)–12(e). For example, the $\Sigma 11$ (113) interface is composed of C type structural units along the entire length of the interface. The $\Sigma 11$ (113) and $\Sigma 9$ (221) boundaries are verified via HRTEM results in the literature [116]. However, the interface structures of many other $\langle 110 \rangle$ symmetric tilt misorientations are notably different than those in copper. The aluminum $\Sigma 3$ (112) interface in Fig. 12(g) shows that short stacking fault facets are nucleated between C structural units. However, the length of each of the ISF facets is much shorter in aluminum than in copper, which is in agreement with the results shown in Fig. 10. This observation is also validated by HRTEM images from Medlin et al. [80]. For the $\Sigma 17b$ (223) symmetric tilt interface misorientations, the stacking faults that are prominent in copper do not appear in aluminum. Instead, the E structural unit is observed, separated by different numbers of A' structural units depending on the misorientation angle. This result quite intriguing since in copper the E structural unit does not appear until the misorientation angle of the interface is increased beyond 109.5° . Again, the SUM fails to describe this situation, as the structural units change discontinuously over the misorientation range.

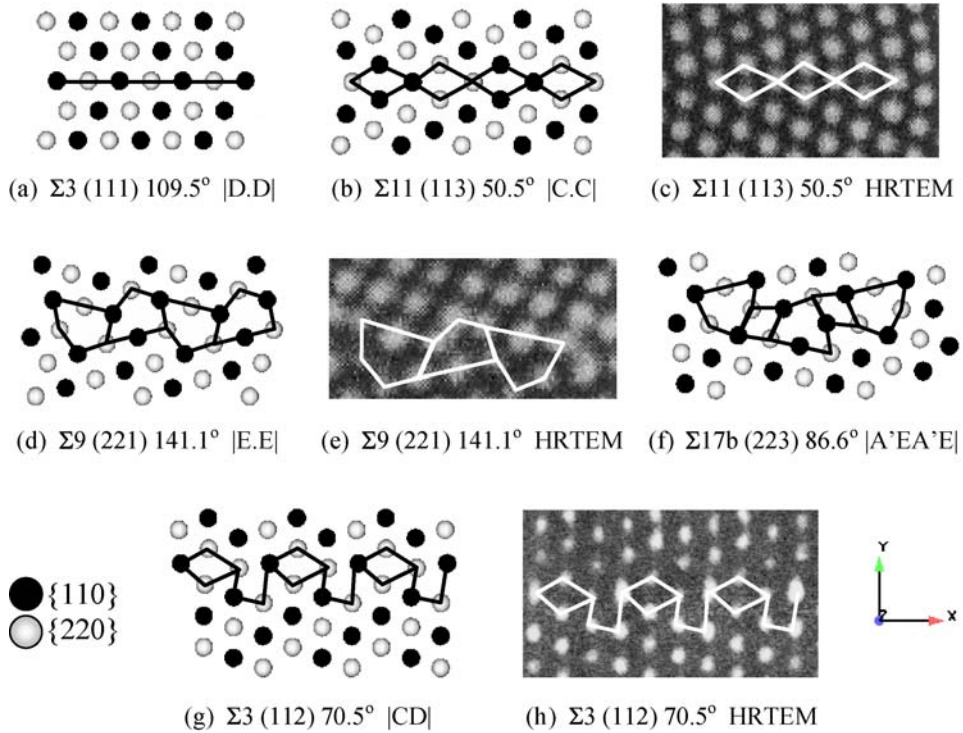
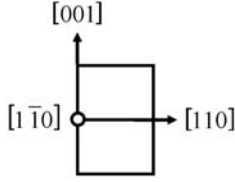


Fig. 12. Bicrystal interface structures and SUM notation for aluminum $[1\bar{1}0]$ interface models. Figures (c) and (e) are reprinted from [116] with permission; © 1992 Elsevier. Figure (h) is reprinted from [80] with permission; © 1993 Materials Research Society.

3.3. Asymmetric tilt grain boundaries

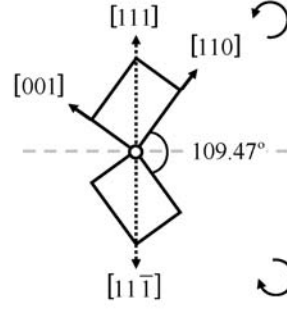
The recent ability to experimentally measure all five grain boundary degrees of freedom [117] has shown that asymmetric tilt grain boundaries are observed in polycrystals in higher frequency than symmetric tilt grain boundaries (except the coherent twin boundary) and twist grain boundaries [118–122]. Therefore, it is possible that asymmetric tilt grain boundaries are present in high frequencies in nanocrystalline materials as well. As discussed in Section 1.1, symmetric tilt grain boundaries are formed by rotating the opposing lattice regions about a misorientation axis that lies perpendicular to the grain boundary plane normal. Asymmetric tilt grain boundaries are formed by subsequent rotations of the grain boundary plane with the misorientation angle of the opposing lattice regions held fixed, such that the adjoining lattices are asymmetric about the interface. The grain boundary rotation angle is defined as the inclination angle of the boundary. Previous studies have shown that the orientation of the grain boundary plane (inclination angle) for $\Sigma 3$ grain boundaries can have a strong effect on material properties such as the GB energy [82], GB diffusion [123] and intergranular corrosion resistance [124]. In this section, the structure

$$\Sigma = 1/(001)/0^\circ \text{ STGB}$$



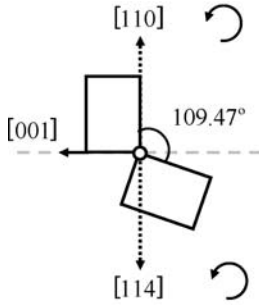
(a)

$$\Sigma = 3/(111)/109.47^\circ \text{ STGB}$$

Rotate (a) by $-54.74^\circ, +54.74^\circ$

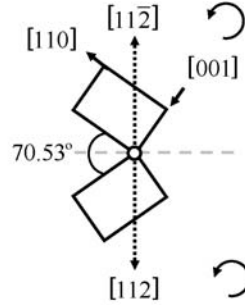
(b)

$$\Sigma = 3/(110)_1/(114)_2 \text{ ATGB}$$

Rotate (b) by $+35.26^\circ$

(c)

$$\Sigma = 3/(112)/70.53^\circ \text{ STGB}$$

Rotate (b) by 90°

(d)

Fig. 13. Schematic showing the effect of misorientation and inclination angle for four $\langle 110 \rangle$ tilt grain boundaries: (a) $\Sigma 1 (001) \theta = 0^\circ$ STGB, (b) $\Sigma 3 (111) \theta = 109.47^\circ$ coherent twin boundary, (c) $\Sigma 3 (110)_1/(114)_2 \Phi = 35.26^\circ$ ATGB, (d) $\Sigma 3 (112) \theta = 70.53^\circ$ incoherent twin boundary. In this study, the inclination angles for (b–d) are 0° , 35.26° , and 90° , respectively.

and energy of $\Sigma 3$ ATGBs inclined about the $\langle 110 \rangle$ tilt axis is presented. This understanding is vital for proper interpretation of the dislocation nucleation behavior in Section 4.

Fig. 13 shows a schematic depicting the change in inclination angle from the $\Sigma 3 (111) \Phi = 0^\circ$ symmetric tilt grain boundary to the $\Sigma 3 (110)_1/(114)_2 \Phi = 35.26^\circ$ ATGB to the $\Sigma 3 (112) \Phi = 90^\circ$ STGB. The subscripts for the ATGB denote the grain boundary normal directions for the upper and lower lattices [see Fig. 13(c)]. In this work, the $\Sigma 3 (111) \Phi = 0^\circ$ interface is referred to as the coherent twin boundary (CTB), while the $\Sigma 3 (112) \Phi = 90^\circ$ will be referenced as the symmetric incoherent twin boundary (SITB) to

maintain consistency with the previous literature [82]. However, note that the homophase $\Sigma 3$ (112) $\Phi = 90^\circ$ STGB is considered semi-coherent in many descriptions of interface structure due to slip system compatibility within each crystalline region. The term incoherent is often used explicitly to characterize interfaces which have a mismatch in both the orientation and the lattice structure (number and character of available slip systems) across the boundary [50]. In Fig. 13, the grain boundary plane is represented by the long dotted horizontal line, the grain boundary normals are the short vertical dotted lines, and the lattice is shown as a rectangle for the (1 $\bar{1}$ 0) plane of the FCC unit cell. Consequently, Fig. 13(a) represents the perfect single crystal since the crystal orientation of regions 1 and 2 are identical. Fig. 13(b) shows the $\Sigma 3$ (111) $\Phi = 0^\circ$ CTB which is obtained by rotating the lattice regions in (a) by $+54.74^\circ$ and -54.74° . Fig. 13(c) shows the $\Sigma 3$ (110)₁/(114)₂ $\Phi = 35.26^\circ$ ATGB which is obtained by rotating both crystal lattices in (b) by 35.26° in the counterclockwise direction. Finally, the $\Sigma 3$ (112) $\Phi = 90^\circ$ SITB in Fig. 13(d) is obtained by rotating both lattices in (b) by 90° in the counterclockwise direction. Note that all counterclockwise rotations applied to both lattices between 0° and 90° [Figs 13(b) and 13(d), respectively] result in $\Sigma 3$ ATGBs. Thus, an alternative representation of inclination angle is to view the grain boundary as fixed and the lattice regions as rotating.

3.3.1. Interface energy

Fig. 14(a) shows the calculated $\Sigma 3$ asymmetric tilt grain boundary relative energy as a function of the inclination angle from the $\Sigma 3$ (111) 109.5° coherent twin boundary. The relative $\Sigma 3$ grain boundary energies which are calculated and measured by thermal grooving experiments are also included in Fig. 14(a) [82]. The relative energies are obtained by dividing the grain boundary energy, γ_{GB} , by the (111) surface energy, $\gamma_{Surface}$ (1476 mJ/m^2 for the EAM potential in this study). The error between the calculated and experimental asymmetric tilt grain boundary energies is most significant for inclination angles above 70.53° . This region corresponds to a different phase at the boundary in Cu, which is termed the 9R phase. The rhombohedral 9R phase is formed from an intrinsic stacking fault on every third plane in an FCC structure. The presence of the 9R phase may explain the larger difference in relative boundary energies in this region. Other potential reasons [82] for the discrepancy between calculated and experimental values may be due to the temperature difference (i.e., the experimental values were 1313 K). However, while the magnitude of the calculated energies deviates slightly from experimental energies, the trend of the calculated energies agrees well with the experimental data. Fig. 14(b) shows the bicrystal interface energy versus the interface inclination angle for $\Sigma 3$ asymmetric tilt grain boundaries in copper and aluminum. Two relative minimum energy grain boundary structures in Cu are observed at the coherent twin boundary [$\Sigma 3$ (111) $\Phi = 0^\circ$] and at an inclination angle approximately 5° to 8° from the incoherent twin boundary. In contrast to copper, the aluminum minimum energy configurations are associated with the coherent and incoherent twin boundaries. The low stacking fault energy of copper results in the formation of the 9R phase; however, the 9R phase is not observed in aluminum, a material with a much higher stacking fault energy.

The calculated $\Sigma 3$ ATGB energies in Fig. 14(b) are compared to a theoretical description of asymmetric tilt interface energy which is based on the decomposition of $\Sigma 3$ asymmetric tilt boundaries into facets associated with the $\Sigma 3$ symmetric tilt grain boundaries [82].

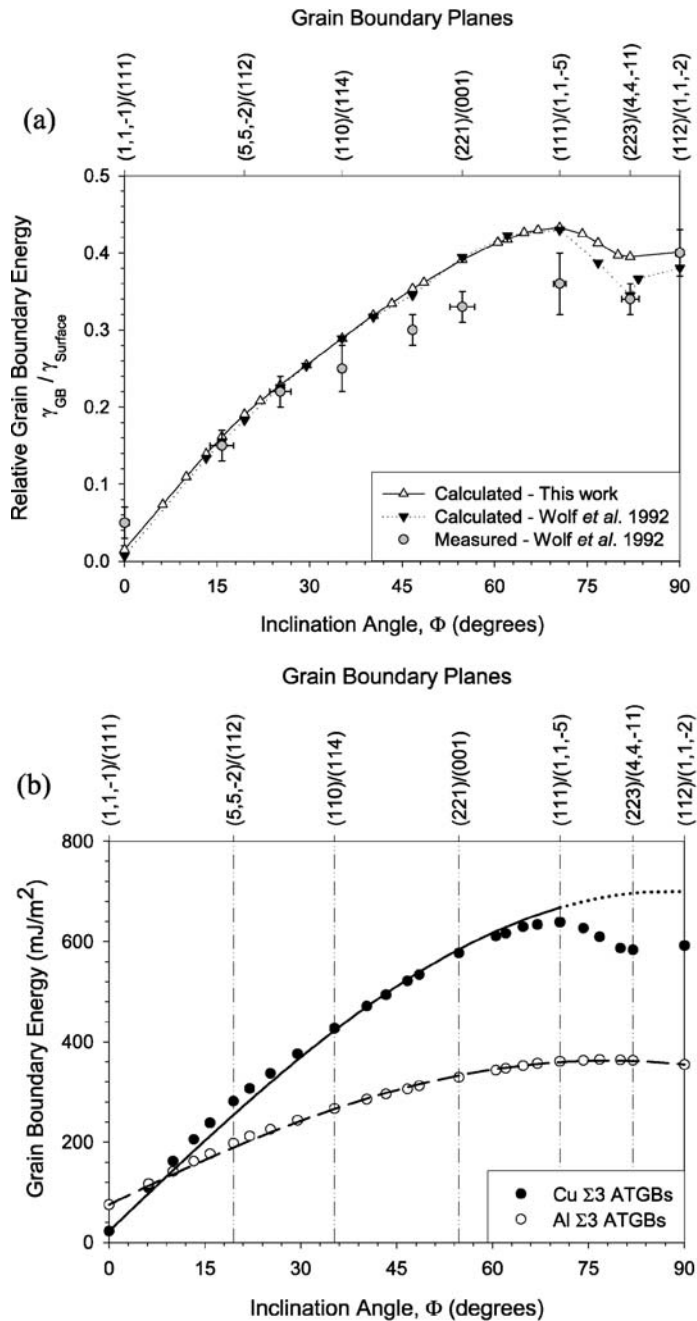


Fig. 14. (a) Relative grain boundary energy, $\gamma_{GB}/\gamma_{Surface}$, as a function of inclination angle for Cu. The values calculated in this work are compared with both calculated values and experimental measurements [82]. (b) Grain boundary energy as a function of inclination angle for Cu and Al.

Note that this decomposition is possible for all asymmetric tilt grain boundaries; however, it may not always be energetically favorable [56]. First, we assume that the boundary energies of the individual facets corresponding to the coherent and incoherent twin boundaries contribute additively (i.e., no interaction energy). Next, the relation between the inclination angle (Φ) and the lengths of the coherent and incoherent twin boundary facets (L_{CTB} and L_{SITB} , respectively), which are perpendicular to each other, is $\tan \Phi = L_{SITB}/L_{CTB}$. Therefore, the $\Sigma 3$ asymmetric tilt grain boundary energy for an arbitrary inclination angle, γ_Φ , is given by

$$\gamma_\Phi = \gamma_{CTB} \cos \Phi + \gamma_{SITB} \sin \Phi, \quad (10)$$

where γ_{CTB} and γ_{SITB} correspond to the coherent and incoherent twin boundary energies. Fig. 14(b) shows that the aluminum curve fits the calculated asymmetric tilt grain boundary energies very well with constants that correspond to the calculated coherent and incoherent twin boundary energies: $\gamma_{CTB} = 75.2 \text{ mJ/m}^2$ and $\gamma_{SITB} = 354.4 \text{ mJ/m}^2$ (recall Fig. 6). The copper curve correlates reasonably well with the calculated GB energies with constants that correspond to the calculated coherent twin boundary energy, $\gamma_{CTB} = 22.2 \text{ mJ/m}^2$, and the hypothetical, unrelaxed incoherent twin boundary energy, $\gamma_{SITB} = 700 \text{ mJ/m}^2$. The hypothetical, unrelaxed energy for Cu is utilized as a fitting parameter that corresponds to the incoherent twin boundary energy without the dissociation of grain boundary dislocations, as discussed in Schmidt et al. [125]. Of course, energy minimization shows the emission of ISF facets as shown in Fig. 8(e). The curves predicted using eq. (10) fit both the calculated asymmetric tilt grain boundary energies for Al and the calculated asymmetric tilt grain boundary energies for Cu with inclination angles $\Phi < 70.53^\circ$ very well. However, the calculated energies deviate from the predicted curve in Cu for inclination angles $\Phi > 70.53^\circ$ (the 9R phase). Additional information on the energy of $\Sigma 3$ asymmetric tilt grain boundaries informed by both experiments [82,83,125,126] and atomistic calculations [79,82] can be found elsewhere.

Tschopp and McDowell have also calculated the asymmetric tilt grain boundary energies for other low order CSL systems with $\langle 100 \rangle$ ($\Sigma 5$ and $\Sigma 13$) and $\langle 110 \rangle$ ($\Sigma 9$ and $\Sigma 11$) tilt axes as a function of grain boundary inclination [127]. They found that not all asymmetric tilt grain boundaries follow a relation based on the ideal faceting into symmetric tilt grain boundaries. In particular, the agreement with a relation similar to eq. (10) depends on the inclination angle separating two STGBs of the same CSL system (45° for the $\langle 100 \rangle$ system and 90° for the $\langle 110 \rangle$ system), the anisotropy in the STGB energies, and the stacking fault energy of the material. The $\langle 100 \rangle$ ATGBs followed an ideal faceting relation very well, while the $\Sigma 9$ ATGBs about the $\langle 110 \rangle$ tilt axis deviated the most from a relation similar to eq. (10).

3.3.2. Interface structure

To characterize the structure of ATGBs, interface atoms with a distorted local environment are identified using the centrosymmetry parameter [115]. A threshold of 0.25 is used as a guideline to delineate atoms belonging to interface structural units from those belonging to the bulk lattice. Once interface atoms are identified, structural units consistent with the coherent and incoherent twin boundaries are used to describe the $\Sigma 3$ asymmetric tilt grain boundary structures. The presence of the 9R phase in Cu necessitates that the GB structures

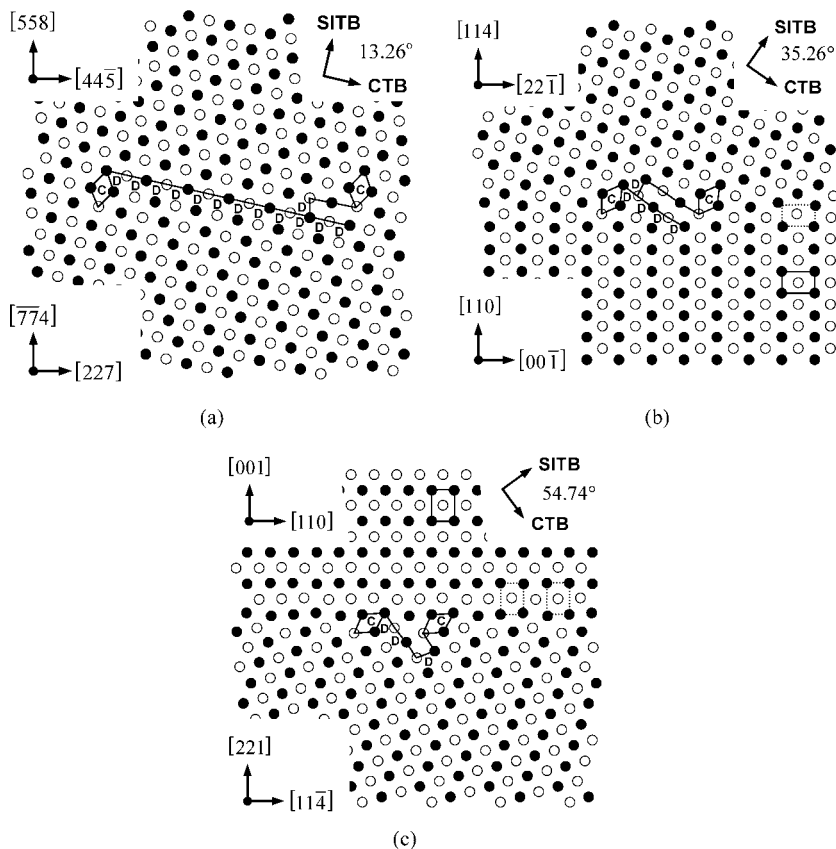


Fig. 15. Three $\Sigma 3$ grain boundary structures in Cu for various inclination angles $\Phi < 70.53^\circ$. The structures are viewed along the $[1\bar{1}0]$ tilt axis; atoms on two consecutive $(2\bar{2}0)$ planes are shown as black and white. The grain boundary normal and period vectors for the lower and upper crystal are shown in the corner boxes on the left-hand side for each grain boundary. The inclination angle is shown in the upper right corner.

for Cu should be separated into two distinct groups, those with inclination angles $\Phi < 70.53^\circ$ and those with $\Phi \geq 70.53^\circ$. The structures for these two groups are presented for copper.

3.3.2.1. Inclination angles $\Phi < 70.53^\circ$ Figs 15(a)–15(c) show the equilibrium 0 K GB structures in Cu for three boundaries with inclination angles $\Phi < 70.53^\circ$. The structures are viewed along the $[1\bar{1}0]$ tilt axis and the atoms on two consecutive $(2\bar{2}0)$ planes are shown as black and white. The GB normal and period vectors for the lower and upper crystal are shown in the corner boxes on the left-hand for each GB. The two arrows in the upper right corner correspond to the ideal location of the coherent and incoherent twin boundary facets based on the inclination angle (also shown). There are two facets for each $\Sigma 3$ ATGB: one facet corresponds to the structural units (SUs) of the CTB (D) and one facet corresponds to structural units associated with the SITB (C). Apparently, the structure of

the $\Sigma 3$ ATGB can be described using structural features that are characteristic of those that comprise the $\Sigma 3$ symmetric tilt grain boundaries [see Figs 8(a) and 8(e) in Cu and Figs 12(a) and 12(g) in Al]. As discussed in the previous section, the D SU is closely related to a Shockley partial dislocation and is frequently found terminating an intrinsic stacking fault [e.g., in the $\Sigma 3$ (112) SITB] [60].

Images in Fig. 15 indicate that the number of D structural units on the coherent twin boundary facet decreases as the inclination angle increases; the $\Sigma 3$ $(77\bar{4})_1/(558)_2$ $\Phi = 13.26^\circ$ ATGB contains 12 D SUs on every CTB facet while the $\Sigma 3$ $(110)_1/(114)_2$ $\Phi = 35.26^\circ$ ATGB only contains 4 D SUs on every CTB facet. The SITB facet contains both C and D structural units. All $|\text{DC}|$ units for ATGBs with $\Phi < 70.53^\circ$ are separated by at least one D SU on the CTB facet; i.e., a $|\text{DCDC}|$ structure could occur on the SITB facet, but this would be a metastable atomistic configuration. Also, notice that the D SU associated with the SITB dissociates in a direction parallel to the coherent twin boundary facet. In Fig. 15(a), the D SU dissociates in a direction alongside the coherent twin facet. However, for inclination angles $\Phi \geq 54.74^\circ$ [Figs 15(b) and 15(c)] the D SU dissociates in the opposite direction. The transition of the dissociated D structural unit from one side of the C structural unit to the other side depends on the relative proximity of the facets. For $\Sigma 3$ ATGBs, the spacing between the coherent and incoherent twin boundary facets determines the local strain state, which then influences the directionality of dissociation of the D structural unit. In asymmetric boundaries with inclination angles immediately below this transition, the dissociated D structural unit approaches the C structural unit on the adjacent SITB facet. The dislocation content of the C structural unit may then exert a force on the partial dislocation associated with the D structural unit, which causes the dissociation to proceed in the opposite direction. It is also interesting to note that all D structural units associated with the SITB dissociate, while none of the D structural units associated with the low energy coherent twin boundary facet dissociate.

3.3.2.2. Inclination angles $\Phi \geq 70.53^\circ$ Figs 16(a)–16(c) show the equilibrium 0 K GB structures in Cu for three asymmetric tilt boundaries with inclination angles $\Phi \geq 70.53^\circ$. This particular set of boundaries has attracted a significant amount of interest due to the 9R phase transformation that occurs in several low SFE materials, e.g., Cu [82], Ag [84,85], and Au [128]. In this work, we investigate the effect of inclination angle on the GB structure by comparing numerous GB structures within the 9R region.

The maximum in GB energy occurs at the $\Sigma 3$ $(111)_1/(11\bar{5})_2$ $\Phi = 70.53^\circ$ ATGB [Fig. 16(a)], which is a transitional GB structure for the 9R phase in the $\Sigma 3$ system in Cu. For this structure, the number of $|\text{DC}|$ units on the SITB is equal to the number of D units on the coherent twin boundary; all ATGBs with inclination angles greater than 70.53° have a larger ratio of SITB structural units than coherent twin boundary features. All D structural units for ATGBs with $\Phi > 70.53^\circ$ are separated by at least one $|\text{DC}|$ unit on the SITB facet; i.e., only a metastable 0 K configuration contains two D units on the same coherent twin boundary facet. For each of these structures, the D structural unit on the SITB facet dissociates to the same side of the adjacent C structural unit continuing the trend shown in Fig. 15(c). The intrinsic stacking fault caused by the dissociation of the D structural unit on every third plane creates the 9R phase. The ratio of the D features on the CTB facets to the $|\text{DC}|$ units on the SITB facets decreases as the inclination angle increases.

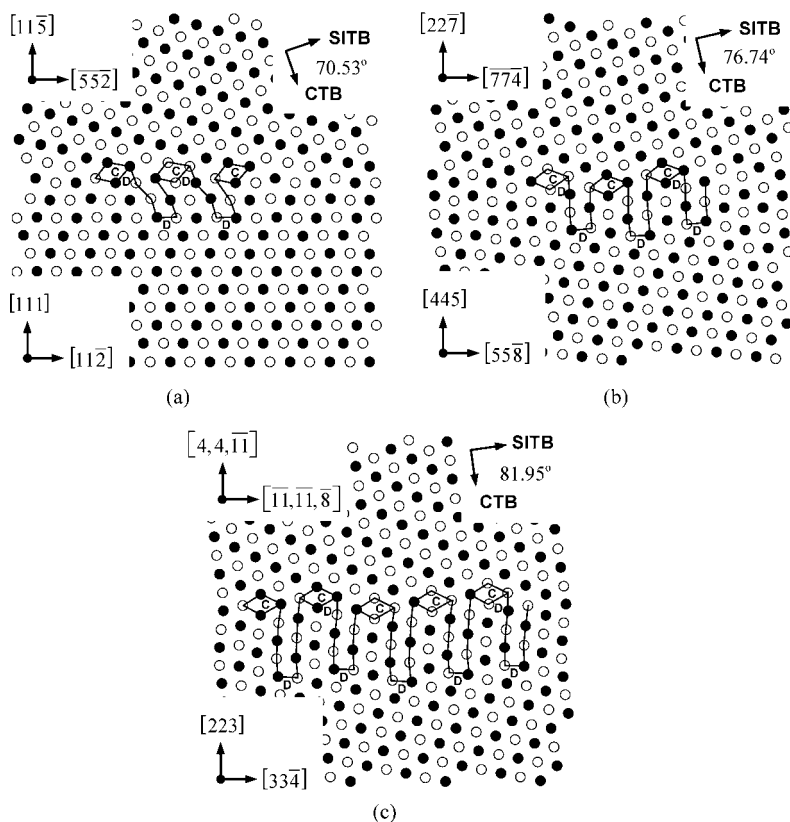


Fig. 16. Three $\Sigma 3$ grain boundary structures in Cu for various inclination angles $\Phi \geq 70.53^\circ$. The same format as Fig. 15 is used for illustrating the grain boundary structures.

All ATGBs with the 9R phase are separated by two boundaries. The misorientation change across these GBs occur along the two sub-boundaries that contain the 9R phase [viewed from upper to lower crystal of Figs 16(a)–16(c)]. The upper boundary of C structural units rotates the upper lattice to coincide with the 9R phase lattice. The dissociation of the D features from the SITB facet allows the C structural units to rearrange to minimize strain at this upper boundary; this allows only a partial rotation of the lattice to occur. The lower boundary of the 9R phase is a small angle dislocation boundary composed of the dissociated partial dislocations (D structural units). This sub-boundary provides additional lattice rotation to coincide with the given misorientation between the upper and lower crystals.

The width of the 9R phase is a function of the degree of dissociation of the D structural unit on the SITB facet and this width changes as a function of the inclination angle for ATGBs with $\Phi > 70.53^\circ$. As shown in Fig. 16, the dissociation width increases with $\Phi > 70.53^\circ$ until the $\Sigma 3 (223)_1/(4, 4, \bar{1}\bar{1})_2$ $\Phi = 81.95^\circ$ ATGB and then decreases to meet the width calculated in the SITB [recall Fig. 8(e)]. All of these GBs, including the SITB, contain the correct 9R phase stacking sequence caused by the intrinsic stacking faults on

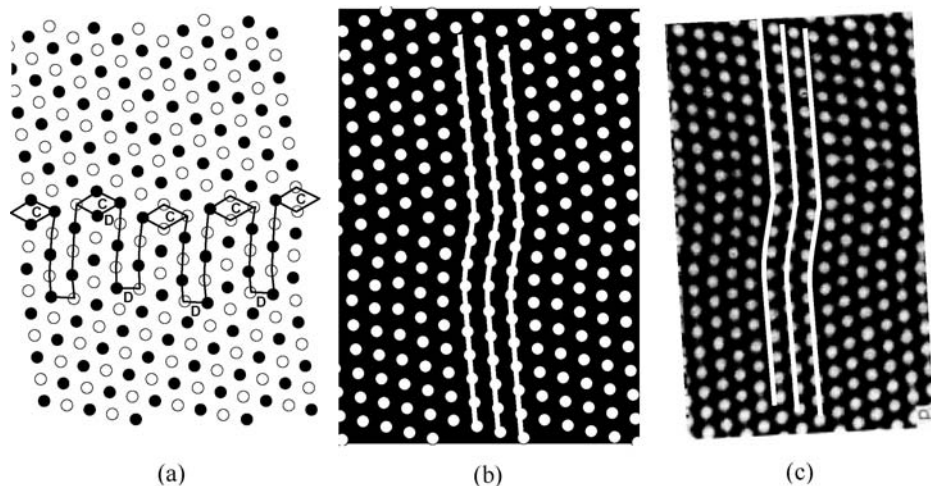


Fig. 17. Comparison of calculated $\Sigma 3 \Phi = 81.95^\circ$ asymmetric tilt grain boundary structure with the 9R phase in Cu with experimental HRTEM image of the 9R phase in Ag. (a) Interface structure with structural units outlined, (b) simulated image using atom positions from (a), and (c) HRTEM image of Ernst and coworkers [84]. The white lines correspond to the $\{111\}$ planes in the adjoining crystals and at the interface. Figure (c) reprinted from [84] with permission; © 1992 The American Physical Society.

every third plane. However, this 9R phase may not be present in some boundaries (e.g., the SITB), because there is an energetic penalty to dissociate the D structural unit further and expand the 9R phase. In Fig. 16(a), notice the distortion of the intrinsic stacking fault associated with the dissociated D structural units, which potentially restricts the expansion of the 9R phase. However, as the lattices and structural units are rotated with increasing inclination, the width of the dissociation and the 9R phase increase.

Fig. 17 compares the calculated $\Sigma 3 \Phi = 81.95^\circ$ asymmetric tilt grain boundary structure containing the 9R phase in Cu with an experimental HRTEM image of the 9R phase in Ag [84]. Although different materials, both Cu and Ag have low stacking fault energies and an FCC crystal structure, which enables the 9R phase to form. Fig. 17(a) shows the structural unit description of the ATGB used to generate a simulated image in Fig. 17(b), which is compared with the experimentally observed HRTEM image in Fig. 17(c). The 2D projected view of the $\{111\}$ planes, in white, shows the agreement between the simulated and experimental images. In fact, these images also have similar widths of the 9R phase, despite the finding by Medlin and coworkers [129] that the width of the 9R phase often increases with time in the HRTEM.

3.3.3. $\Sigma 3$ ATGB structure and faceting

In a method analogous to the structural unit model, the structural units and their corresponding facets can be predicted for $\Sigma 3$ ATGBs [130]. Fig. 18 shows how the calculated $\Sigma 3$ ATGB structures for Cu and Al can be predicted based upon the coincidence plot [131] and the atomistic GB structures of the two $\Sigma 3$ STGBs. In this respect, the following method used for predicting the $\Sigma 3$ ATGB structure is very similar to the decomposition lattice

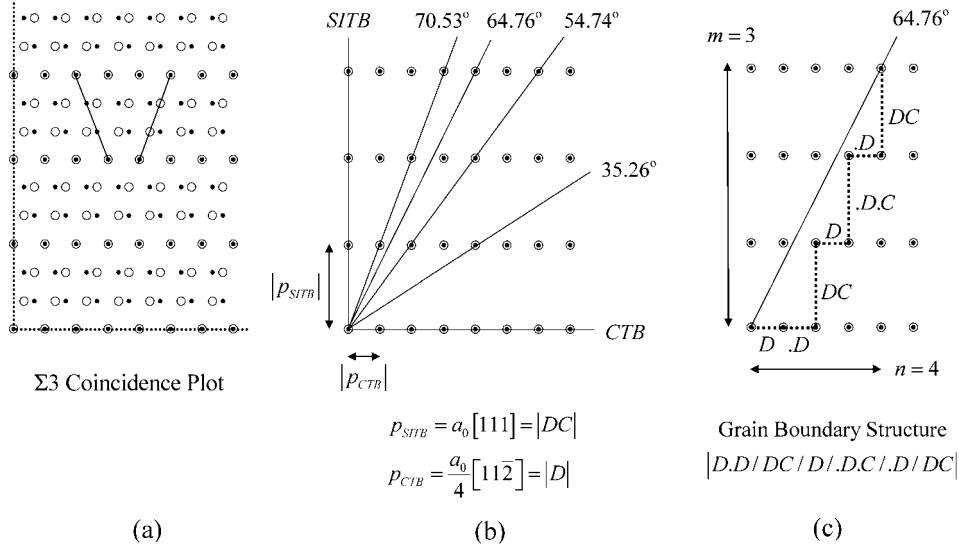


Fig. 18. A model describing the structural units and faceting in $\Sigma 3$ ATGBs. (a) Coincident plot for the $\Sigma 3$ system rotated around the $[1\bar{1}0]$ tilt axis. (b) Schematic of the coincident points from (a) along with several GB planes of varying inclination angles. The GB periods of the CTB and SITB correlate to specific atomic SUs. (c) The SU description of the $\Sigma 3 \Phi = 64.76^\circ$ ATGB is predicted based solely on the coincident points from (a) and the SUs from the two $\Sigma 3$ STGBs.

method [55] or strip method of quasicrystallography [132,133]; the strip method is used to determine the structural unit sequence for rational symmetric tilt boundaries. First, as shown in Fig. 18(a), the coincidence plot is created by defining a misorientation angle ($\theta = 70.53^\circ$ in this case) and allowing the two crystal lattices to overlap. In this plot, atoms from the two lattices are shown as small black and large white circles; the coincident sites are a combination of both circles. The coincidence plot visually illustrates the CSL concept for symmetric and asymmetric tilt grain boundaries; notice that one in every three points is coincident, as denoted by the solid lines in Fig. 18(a). The GB plane is then realized by connecting any two coincident points, as shown in Fig. 18(b). Several GB planes are shown: the CTB, the SITB, and some intermediate ATGBs with different inclination angles. The GB periods for the CTB and SITB can be defined from either crystal lattice; in this case, the periods for the CTB and SITB are $p_{CTB} = a_0/4[11\bar{2}]$ and $p_{SITB} = a_0[111]$, respectively. The relationship between the inclination angle and the GB periods is defined geometrically as

$$\Phi = \tan^{-1} \left(\frac{m |p_{SITB}|}{n |p_{CTB}|} \right), \quad (11)$$

where m and n are integers defining the number of CTB and SITB period vectors required to link any two coincident points. An alternative expression is that the ATGB period vector decomposes into the period vectors of the two facets, i.e., $p_{ATGB} = mp_{SITB} + np_{CTB}$. Utilizing the atomistic simulations presented in Section 3.2, we can define the structure of

the CTB either as a series of repeating D features with interface period $p_{\text{CTB}} = a_0/4[11\bar{2}]$ or as $|\text{D.D}|$ with an interface period $p_{\text{CTB}} = a_0/2[11\bar{2}]$. The latter description contains additional information about the translation of SUs with respect to each other; the dot preceding a SU denotes a relative translation in the direction of the tilt axis by $a_0/4[11\bar{0}]$. This description requires n to be an even integer. Fig. 18(c) shows how the coincident lattice site from Fig. 18(a), the GB plane from Fig. 18(b), and the STGB structural units from the previous section are combined to predict the configuration of the $\Sigma 3 (554)_1/(11\bar{8})_2$ $\Phi = 64.76^\circ$ ATGB that agrees with the calculated structure. Moreover, the ATGB structural unit and faceting description [130] accurately predicts the GB structural unit description for all 25 $\Sigma 3$ ATGBs in this study, even with the 9R phase formed for ATGBs with $\Phi \geq 70.53^\circ$ in Cu. This result emphasizes the well-defined ordering of structural units and facets for some low order CSL ATGB systems at the atomistic scale.

Tschopp and McDowell concluded that this structural unit and faceting description for ATGBs may also apply to $\Sigma 5$ and $\Sigma 13$ ATGBs about the $\langle 100 \rangle$ tilt axis [127]. They reported that these CSL systems also facet into the structural units of the corresponding $\Sigma 5$ and $\Sigma 13$ STGBs. However, this description does not apply to all CSL systems. For example, in the same study, the ATGB structure of the $\Sigma 9$ and $\Sigma 11$ ATGBs about the $\langle 110 \rangle$ tilt axis deviated from this faceted description. The boundary rearranged such that a large fraction of GB atoms (identified via centrosymmetry [115]) bounding the structural units were correlated with the $\{111\}$ planes, presumably due to the low energy of the $\{111\}$ surfaces [134]. Additional factors included the large free volume of the E structural unit for ATGBs with inclination angles near the $\Sigma 9 (221)$ and $\Sigma 11 (332)$ STGBs and the proximity of ATGBs to the $\{111\}/\{110\}$ ATGB.

4. Dislocation nucleation from symmetric and asymmetric tilt boundaries in Cu and Al

The computational materials science community has made considerable progress towards understanding the atomic scale mechanisms associated with inelastic deformation in metallic crystalline materials via the use of atomistic simulations. In particular, atomistic simulation has been used to model the nucleation of partial dislocations from interfaces in FCC metals using bicrystal [16–19,38,39] and nanocrystalline geometries [20–37]. The work of Sansoz and Molinari [38,39] represented an important advancement because they were able to directly correlate individual failure mechanisms to the presence of certain structural units along the interface plane using the quasicontinuum method. In tension, failure of the interface occurred through partial dislocation nucleation and grain boundary cleavage. In shear, Sansoz and Molinari reported that three different failure modes could exist depending on the initial boundary configuration: grain boundary sliding by atomic shuffling, nucleation of partial dislocations from the bicrystal interface and grain boundary migration. Atomic shuffling occurred during a shear deformation only for interfaces that contained the E structural unit, which is associated with the $\Sigma 9 (221)$ interface [recall Fig. 8(c)]. Sansoz and Molinari proposed that the free volume inherent to this structural feature was responsible for triggering the atomic shuffling event during shear. Results in the literature

typically do not provide such detailed information regarding the role of individual interface features in the deformation process.

Recently, there has been some debate in the literature regarding the emission of full dislocations from grain boundaries in nanocrystalline materials. Initial work by Van Swygenhoven and coworkers [25,27] in nanocrystalline pure nickel and copper with a grain size of approximately 12 nm showed that the leading (first) partial dislocation could be emitted from a grain boundary. In their work, the first partial dislocation would sweep across the nanosize grain and become absorbed into the opposing interface. The trailing (second) partial dislocation was not emitted from the grain boundary; as a result, an extended intrinsic stacking fault (which was typically longer than the equilibrium spacing between partial dislocations) remained within the grain. Through detailed analysis of the grain boundary structure [25,29,31] the nucleation of the first partial dislocation in nanocrystalline metals was shown to be assisted by local atomic shuffling within the interface and stress-assisted free volume migration. Van Swygenhoven and coworkers suggested initially that the nucleation of the first partial dislocation and the associated atomic rearrangement along the interface was sufficient to lower the grain boundary energy such that the emission of the second partial dislocation was unnecessary.

MD simulations by Yamakov et al. [20–23] showed that the trailing partial dislocation may be emitted from grain boundary interfaces in aluminum. Aluminum was chosen for their simulations with the hypothesis that the higher intrinsic stacking fault energy (as compared with copper and nickel), which leads to a shorter stacking fault width, would facilitate the emission of the trailing partial dislocation. Yamakov et al. used a columnar microstructure with a thickness of only 10 (110) atomic planes in order to simulate larger nanoscale grain sizes. They identified the stacking fault width as a critical length scale parameter necessary to describe the cross-over between extended partial dislocation and full dislocation deformation regimes in nanocrystalline metals. However, more recent work by Van Swygenhoven and coworkers [32,34] has argued that interpreting the cross-over between deformation regimes in terms of only the intrinsic stacking fault energy is insufficient. They emphasized that the entire generalized stacking fault curve must be taken into consideration and proposed that the ratio of the unstable and intrinsic stacking fault energies is more appropriate to describe the observed dislocation activity in nanocrystalline samples. If this ratio is close to unity, full dislocations are anticipated during the deformation process; conversely, if this ratio is high, extended partial dislocations are expected within the nanocrystalline grains.

In this work, the atomic scale mechanisms associated with dislocation nucleation from symmetric and asymmetric tilt interfaces in aluminum and copper are studied using molecular dynamics simulations. Whereas most previous MD work has used columnar and 3D nanocrystalline geometries, this work examines the nucleation of full dislocation loops from well-defined high-angle interfaces using a bicrystal configuration (recall Section 2.5). Calculations are performed on several distinct sets of symmetric and asymmetric interfaces. The primary goal of this work is to map the evolution of the interface structure during the dislocation nucleation process. We do not consider absorption of partial dislocations into an interface or dislocation–dislocation interactions after multiple nucleation events.

4.1. Symmetric tilt grain boundaries

4.1.1. $\Sigma 5$ (310) 36.9° interface

Fig. 19 shows the uniaxial tensile deformation of a $\Sigma 5$ (310) 36.9° interface in aluminum at 10 K. Figs 19(a)–19(d) are colored¹ according to the centrosymmetry parameter [115]; atoms with a centrosymmetry parameter close to zero are removed to facilitate viewing of the defect structures. Figs 19(e)–19(g) show atomic positions at the same time step as Figs 19(b)–19(d) with atoms colored by the magnitude of the atomic slip vector [135]. The atomic slip vector is designed to identify atoms that have been displaced relative to their reference neighbors, even if they reside in a perfect FCC environment. This includes both stacking fault (partial slip) regions and regions of full slip. In this work, the atomic slip vector is calculated using the isobaric–isothermal equilibrium positions of the atoms as the reference configuration. In Figs 19(b)–19(d), full dislocation loops are nucleated from the bicrystal interface during uniaxial tensile deformation. Initially, partial dislocations are nucleated from the interface, indicated by arrows in Fig. 19(b). In the lower lattice region, slip occurs on the (111)[$\bar{1}01$] and (11 $\bar{1}$)[101] slip systems, which are the most favorable slip systems according to a Schmid factor analysis. Likewise, the most favorable slip systems are activated in the upper lattice region. The tensile stress required to nucleate the first partial dislocation at 10 K from the $\Sigma 5$ (310) boundary is calculated as 5.74 GPa. For the given orientation, this corresponds to a critical resolved shear stress of approximately 2.81 GPa, which is comparable to the ideal shear strength of aluminum obtained from first-principles calculations of 2.84 GPa [72].

In Fig. 19(c), the leading partial dislocations have moved further away from the interface, leaving behind an intrinsic stacking fault. The trailing partial dislocation has been emitted for the defect marked with an arrow, resulting in a dislocation loop. As deformation proceeds, several dislocation loops are emitted from each interface in Fig. 19(d). In Figs 19(c) and 19(d), the width of the stacking fault ribbon of the dislocation loops appears to be greater in one direction than the other. The thicker direction corresponds to the edge component of the dislocation loop. Byun [136] showed that at equilibrium, the stacking fault widths of edge and screw dislocations will differ, even though the intrinsic stacking fault energy is the same. Byun reported that the equilibrium intrinsic stacking fault width of an edge dislocation is approximately twice that of a screw dislocation. However, the intrinsic stacking fault width can depend on applied stresses, particularly in materials with low intrinsic stacking fault energies. Byun [136] showed that as the intrinsic stacking fault energy is increased to 100 mJ/m², the influence of applied stresses on the partial dislocation spacing becomes minimal. In this work, the intrinsic stacking fault energy of aluminum predicted by the interatomic potential is 146 mJ/m²; thus, the separation distance between partial dislocations is not expected to vary far from the equilibrium spacing. Fig. 19(d) shows that the calculations in this work are in agreement with this result.

In Figs 19(e)–19(g), atoms with an atomic slip vector magnitude less than half of the Burgers vector for a partial dislocation, $\lambda/\sqrt{6}$, are removed for clarity. Dislocations at two distinct points during the nucleation process are identified in Fig. 19(f). The dislocation

¹ For interpretation of the references to color in this figure the reader is referred to the web version of this chapter.

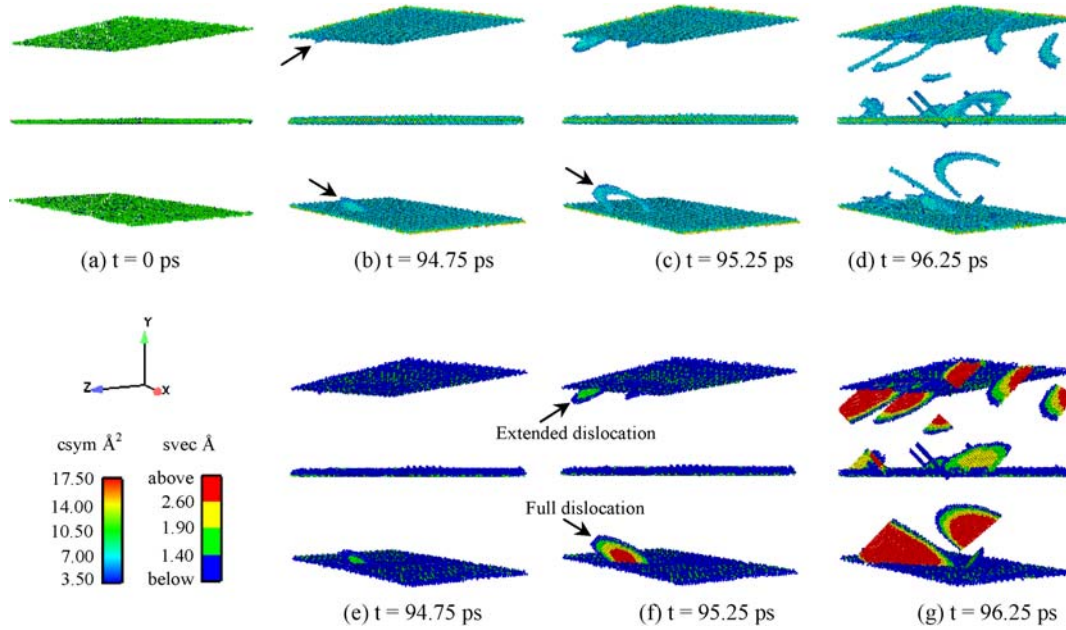


Fig. 19. Nucleation of full dislocation loops during uniaxial tension of a $\Sigma 5$ (310) 36.9° interface at 10 K; (a)–(d) atoms are colored by the centrosymmetry parameter and (e)–(g) atoms are colored by the atomic slip vector. Reprinted from [16] with permission; © 2005 Elsevier.

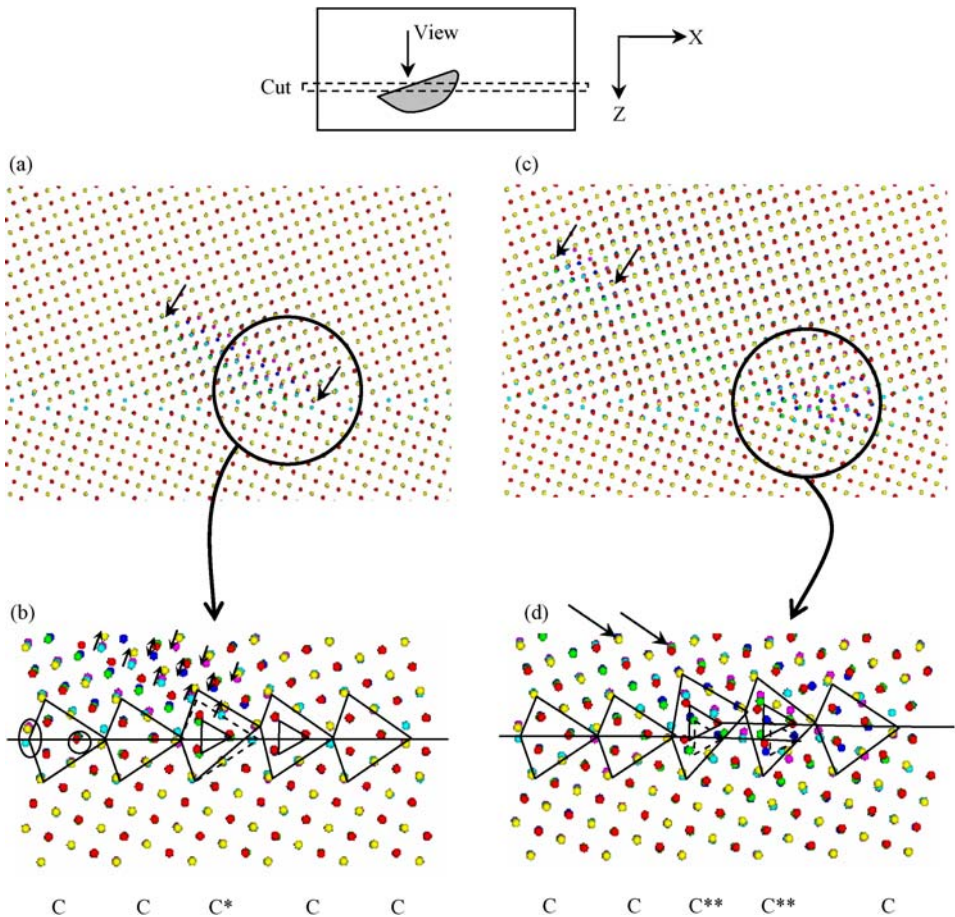


Fig. 20. Nucleation of full dislocation loops during uniaxial tension of a $\Sigma 5$ (310) 36.9° interface at 10 K; (a)–(d) atoms are colored by the centrosymmetry parameter and (e)–(g) atoms are colored by the atomic slip vector. Reprinted from [16] with permission; © 2005 Elsevier.

within the upper lattice region shows an extended formation, as the trailing partial dislocation has not yet been emitted from the interface. Atoms that are shaded green have an atomic slip vector magnitude that ranges between 0.15 and 0.18 nm, which brackets the theoretical value for partial slip of 0.165 nm for aluminum. The dislocation within the lower lattice region has emitted the trailing partial dislocation and has formed a dislocation loop. Full slip has occurred in the wake of the trailing partial dislocation as atoms that are shaded red have an atomic slip vector magnitude between 0.28 and 0.30 nm, which again brackets the theoretical value of 0.286 nm. In Figs 19(f) and 19(g), atoms that are shaded blue and yellow indicate transitions between perfect lattice, intrinsic stacking fault and full slip regions, i.e., the positions of the leading and trailing partial dislocations.

The structure of the $\Sigma 5$ (310) 36.9° interface at two critical points during the dislocation nucleation process is shown in Fig. 20. Here, six {001} atomic planes are cut from

the thickness of the interface model *through* the dislocation loop identified in Fig. 19(c) to illustrate the dislocation nucleation process. This dislocation loop lies in the $(11\bar{1})[101]$ slip system. Atoms are colored² by their respective $\{001\}$ plane and projected into the X - Y plane. Prior to dislocation nucleation, this boundary has an ABAB stacking sequence in the Z -direction. In Fig. 20(a), only the first partial dislocation has been emitted from the interface. This is clearly identified by a shift in the atomic layers at the point of dislocation nucleation. Atoms that once aligned perfectly in an ABAB stacking sequence have been displaced relative to one another. The length of the extended partial dislocation at this time step is approximately 3.16 nm (which is longer than the equilibrium partial dislocation spacing in aluminum) and is shown with arrows in Fig. 20(a). Fig. 20(b) shows a detailed view of the dislocation nucleation point. First, notice that interface expansion during the uniaxial deformation allows some atoms to migrate in the direction of the load. However, the atom that is coincident between lattice regions remains stationary. The dislocation slip process involves atoms that were originally identified as belonging to the structural units. One of the structural units (in the second layer of atoms) is irreversibly deformed as a result of the partial dislocation slip, labeled as C^* . The C structural units surrounding this defect unit appear to be only slightly modified to accommodate the slip process. The centerline of the interface is shown in Fig. 20(b). Even though the structural units are being deformed by the slip process, the interface still remains planar after the emission of the first partial dislocation.

As deformation continues in Fig. 20(c), the second partial dislocation is emitted from the interface, creating a dislocation loop. The loop itself is not visible in this view; however, it is clear that the second partial has been emitted because the atomic layers associated with full slip have aligned on top of each other. The positions of the leading and trailing partial dislocations are marked with arrows in Fig. 20(c) with a separation of approximately 1.08 nm. Fig. 20(d) shows a detailed view of the interface after the emission of the trailing partial dislocation. Two deformed structural units are identified along the interface plane, labeled as C^{**} . The C^{**} deformed unit appears only after the emission of the second partial dislocation and involves a small step or ledge within the interface plane. The shape of the C^{**} unit is similar to that of the C^* structural unit; however, additional slip from the trailing partial dislocation has further amplified the asymmetric expansion. The ledge has a peak magnitude in the Y -direction of approximately 0.18 nm and is stable, because it involves atoms that are associated with the full slip event. The remainder of the interface accommodates the development of this ledge by smoothly shifting in opposite directions on either side of the dislocation nucleation point, as shown in Fig. 20(d). For the C^{**} structural unit shown on the left in Fig. 20(d), the ledge occurs between the first and third atomic layers; in contrast, the ledge occurs between the third and fifth atomic layers for the C^{**} structural unit shown on the right. This indicates that the ledge occurs at the intersection of the slip plane and the interface. The angle depends on the orientation of the slip plane relative to the misorientation axis. Calculations in Spearot et al. [16] confirm that the ledge is formed during uniaxial tensile deformation of other boundaries in Al which contain the C structural unit, such as $\Sigma 109$ $(10\ 3\ 0)$ 33.4° and $\Sigma 73$ (830) 41.1° . Thus, the formation of the ledge is not restricted to the low-order CSL boundary. Fig. 21 shows a schematic of the dislocation nucleation process and the resulting interface ledge after

² See footnote 1.

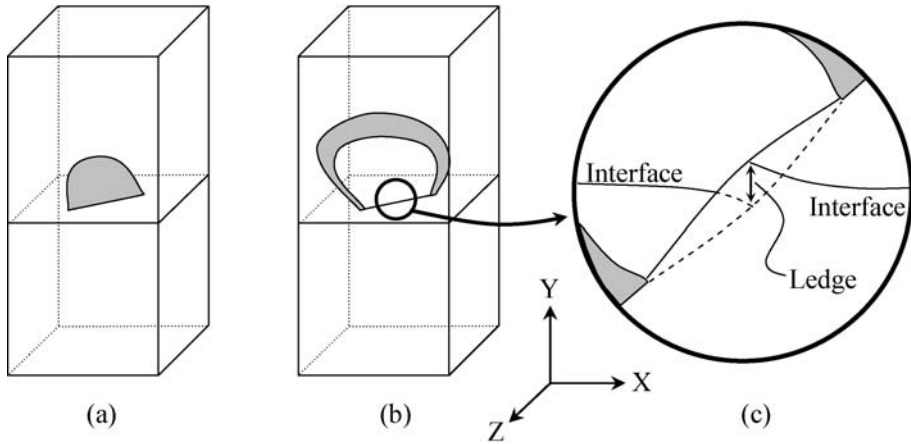


Fig. 21. Schematic of the dislocation nucleation process: (a) after emission of the first partial dislocation, (b) after emission of the trailing partial dislocation creating a dislocation loop and (c) resulting interface structure showing formation of a ledge. Reprinted from [16] with permission; © 2005 Elsevier.

the emission of the full dislocation. In Section 6, the formation and geometry of the ledge created during the dislocation nucleation process will be discussed in terms of disclinations and disconnections [69].

4.1.2. Grain boundaries with dissociated structure

Molecular dynamics simulations are used to study the process of dislocation nucleation from bicrystal interfaces with dissociated structure. Fig. 22 shows a $\Sigma 361$ (6 6 17) 53.1° interface in copper at 10 and 300 K subjected to a uniaxial tensile deformation normal to the interface plane. A detailed characterization of the interface structure during the tensile deformation process is presented in Fig. 23. The specific points of interest are circled and labeled A–D in Fig. 22. When subjected to a tensile deformation, Figs 22(b) and 22(f) show that the bicrystal interface structure evolves prior to the dislocation nucleation event. Specifically, tensile deformation applied normal to the interface plane causes the ISF facet to become shorter in length. In Fig. 23(a), at an interface model strain of 5.0%, the length of the intrinsic stacking fault facet is approximately 40% of its length after energy minimization [recall Fig. 9(a)]. Additional tensile strain causes partial edge dislocations to be nucleated from the bicrystal interfaces, as shown in Figs 22(c) and 23(b). Initially, a partial edge dislocation is nucleated from the interface at the intersection of the ISF facet and the bicrystal boundary. The core of the partial dislocation is not shown in Fig. 23(b), only the extrinsic stacking fault (ESF) that extends from the partial dislocation core back to the interface. Because dislocation nucleation involves the entire slip plane through the thickness of the interface model, the ABAB stacking sequence in the Z-direction is preserved. In the upper lattice region, slip occurs initially on the (111) plane, which is a secondary slip plane according to the Schmid factor. Likewise, the secondary (111) slip plane is activated in the lower lattice region. This indicates that the ISF facet promotes slip activity on the secondary slip systems. This result is due to the configuration of the ISF facet which potentially acts as a stress riser.

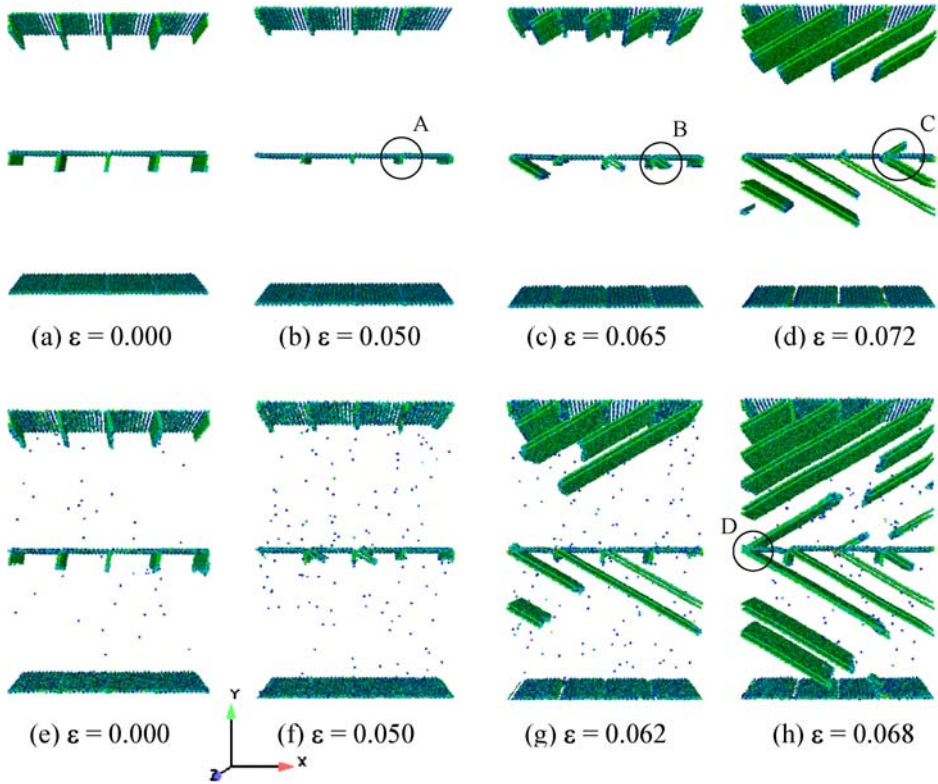


Fig. 22. Uniaxial tensile deformation of the 53.1° copper interface model at (a)–(d) 10 K and (e)–(h) 300 K. Dislocations are nucleated from the intersection of the ISF facet and the bicrystal boundary. Reprinted from [17] with permission; © 2007 Elsevier.

Continued tensile strain leads to the nucleation of partial edge dislocations from the ISF facet into the opposing lattice region, as shown in Figs 22(d) and 22(h). The additional dislocation nucleation is accompanied by a second decrease in the length of the ISF facet, which is shown in Fig. 23(c). As the leading partial edge dislocations glide away from the interface, Fig. 22(h) shows that the ESF will transform into an ISF. This indicates that one trailing partial dislocation is nucleated from each side of the interface during the tensile deformation process. At this point, the ISF facet has become completely absorbed by the interface to facilitate this final transition, as shown in Fig. 23(d). Although not shown in Fig. 22, this transition will occur during simulations at both 10 and 300 K. In copper, the leading partial edge dislocations remain connected to the interface by an intrinsic stacking fault. Throughout the entire deformation process, the interface structural units away from the dislocation nucleation site are largely unaffected.

In Spearot et al. [17] additional calculations are presented which explore the nucleation of dislocations from other boundaries with dissociated structure. It was found that as the misorientation angle of the interface is increased from 53.1° to 59.0°, leading to a decrease in the spacing between ISF facets (recall Fig. 9), the failure mode changes from

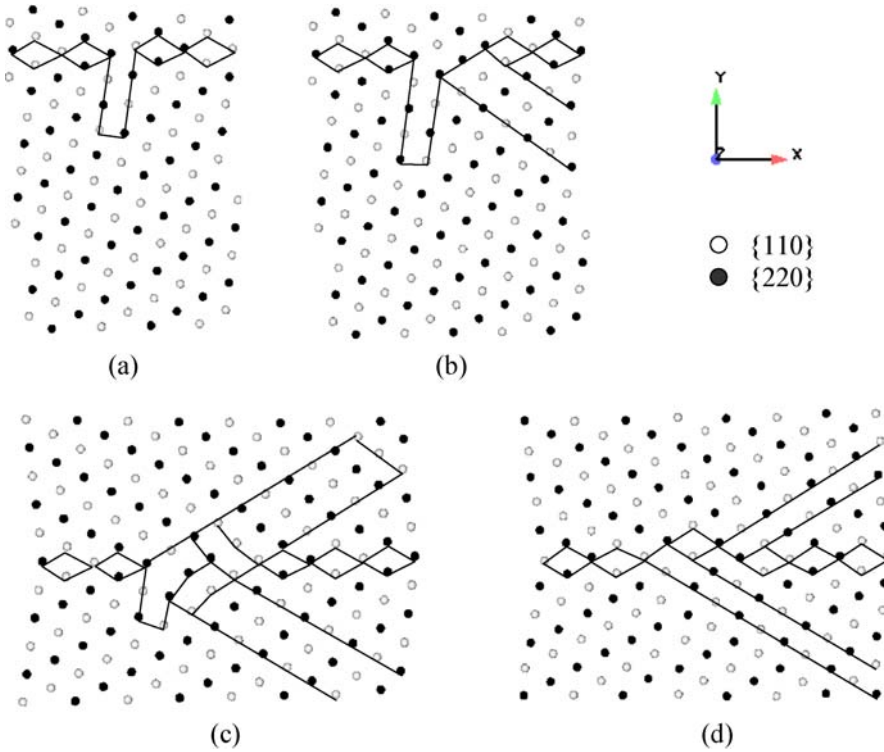


Fig. 23. Detailed examination of the 53.1° copper interface structure during the uniaxial tensile deformation process. Images (a)–(d) correspond to circled regions in Fig. 22. Reprinted from [17] with permission; © 2007 Elsevier.

one that is dominated by dislocation nucleation on secondary slip systems at the ISF facet to that which is a mixture of dislocation nucleation on both primary and secondary slip systems [17]. Specifically, for the 54.4° boundary the spacing between ISF facets is just barely sufficient to allow the nucleated partial dislocation to pass into the lattice region. However, this is not the case with the 59.0° boundary. Here, the spacing between ISF facets critically inhibits the nucleation of partial edge dislocations on the secondary slip planes; the ISF facet blocks the motion of the nucleated partial edge dislocation. Consequently, additional interface structural rearrangement is required, facilitating dislocation activity on other slip systems.

Based on the molecular dynamics result presented above, Fig. 24 shows a schematic of the evolution of an asymmetrically dissociated interface under the application of a uniaxial tensile deformation. Specifically, images in Fig. 24 illustrate the positions of partial edge dislocations at critical stages during the tensile deformation process. Here, we assume that the ISF facets are sufficiently far apart that interaction effects do not play a strong role. Fig. 24(a) shows the initial interface structure, with an ISF facet on the (11 $\bar{1}$) slip plane. Tensile stress applied normal to the interface planes causes the ISF to become shorter in length and promotes dislocation nucleation on the (111) slip plane, as shown in Fig. 24(b).

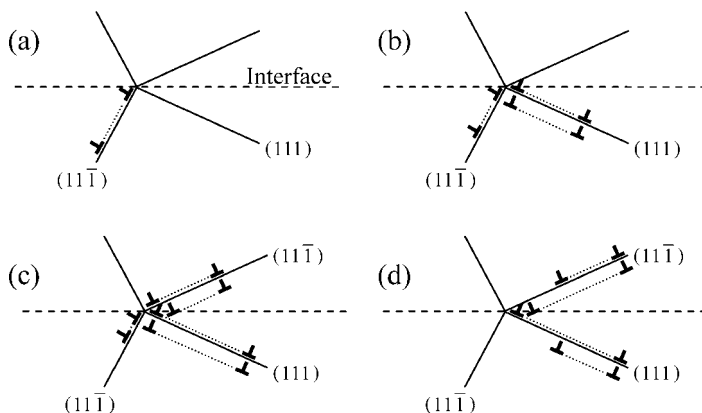


Fig. 24. Schematic of the dislocation nucleation process during tensile deformation from an interface with an asymmetric dissociated structure. See text for additional details on the emission events at each stage of deformation. Reprinted from [17] with permission; © 2007 Elsevier.

Initially, the emitted dislocation is connected back to the interface via an extrinsic stacking fault. Additional tensile strain leads to dislocation nucleation on the secondary slip plane in the opposing crystal region, as shown in Fig. 24(c). Initially, dislocations in both lattices are connected back to the interface via an extrinsic stacking fault. Finally, the ISF facet is completely absorbed by the interface and the extrinsic stacking faults are transformed into intrinsic stacking faults by the emission of trailing partial dislocations from the interface.

The interface transformations described above are remarkably similar to that discussed by Baskes et al. [137] concerning the stress dependence of a lock formation consisting of a stair rod dislocation in nickel. The stair rod dislocation is the sessile product of two partial edge dislocations on intersecting $\{111\}$ slip planes [15]. The parallels between deformation in our simulations and those of Baskes et al. are logical due to the similarities between the stair rod dislocation and the dissociated structural unit. Specifically, Baskes et al. [137] considered a stair rod symmetrically located between two Shockley partial edge dislocations. In our work, the termination of the ISF facet accounts for one of the partial dislocations, while the other partial dislocation is initially positioned at the interface. Baskes et al. showed that the stair rod goes through several transitions, associated with the sequential nucleation of partial dislocations from the lock. First, the separation distance between each Shockley partial dislocation and the stair rod is reduced. Next, one of the Shockley partial dislocations passes through the lock to a position on the other side of the stair rod, with an extrinsic stacking fault. For increased stress, one of the partial dislocations escapes the stair rod lock, transforming the extrinsic stacking fault into an intrinsic stacking fault. Finally, the other Shockley partial dislocation passes through the stair rod resulting in a symmetric formation of extrinsic and intrinsic stacking faults in either side of the lock. While, the sequence of nucleation events is slightly different, the structural similarities between the dislocation configurations described in this work and those in Baskes et al. [137] are evident.

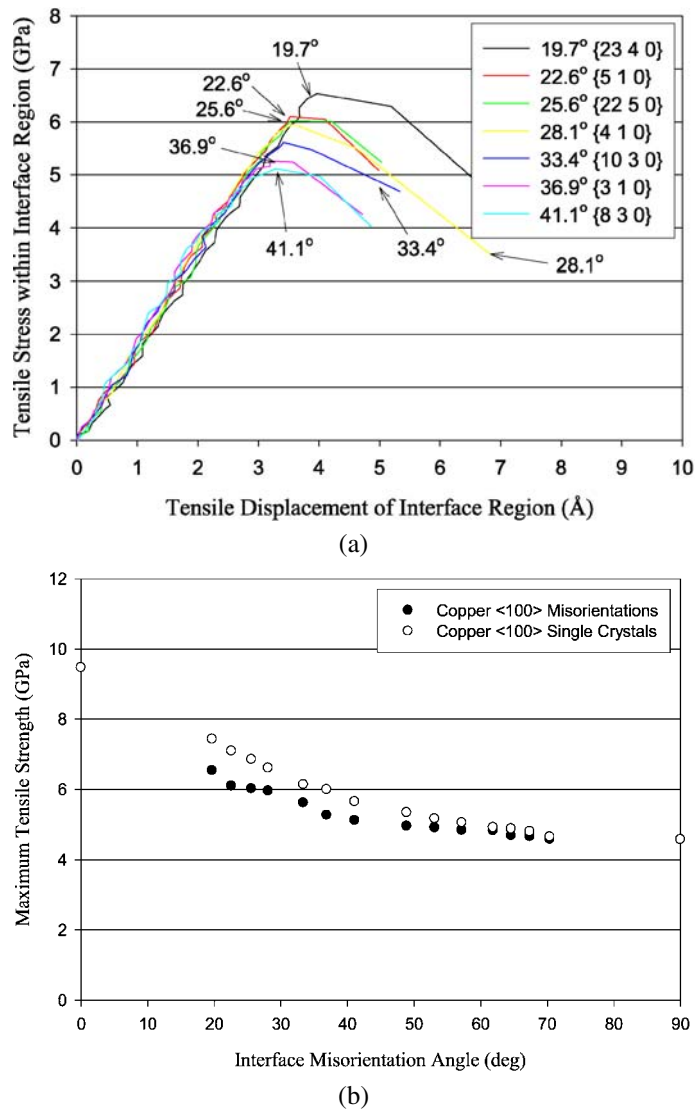


Fig. 25. (a) Stress–displacement diagram for selected $\langle 100 \rangle$ symmetric tilt grain boundaries, and maximum tensile strength versus misorientation angle for (b) $\langle 100 \rangle$ and (c) $\langle 110 \rangle$ interface misorientation. Single crystal data are presented for comparison. Reprinted from [18] with permission; © 2007 Elsevier.

4.1.3. Tensile stress required for dislocation nucleation

Fig. 25(a) shows the tensile stress–displacement response for bicrystal interface models with $\langle 100 \rangle$ tilt axis and misorientations between 19.7° ($23\ 4\ 0$) and 41.1° (830). This range encompasses both $\Sigma 5$ (310) and $\Sigma 13$ (510) boundaries, which are two low Σ boundaries for the $\langle 100 \rangle$ misorientation axis. Clearly, as the misorientation angle increases, the maximum tensile stress achieved during deformation decreases. Contrary to the experimental

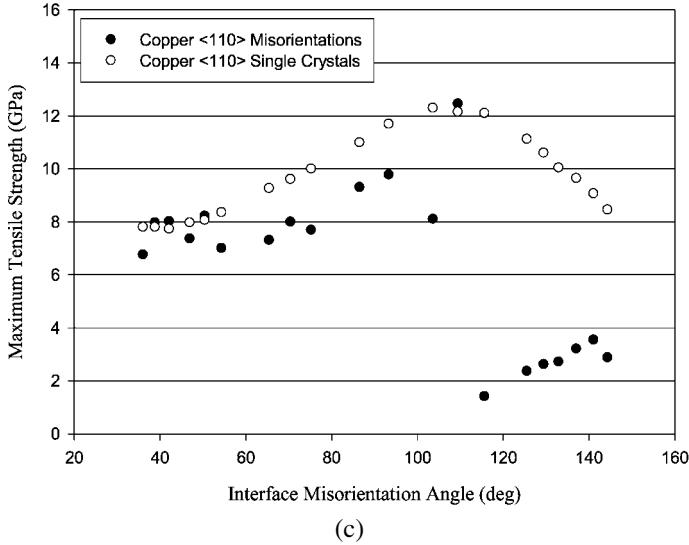


Fig. 25. (Continued)

evidence discussed in the introduction (cf. [13,14]), the low-order Σ boundaries within this misorientation range do not show any special behavior with regard to maximum tensile interface strength. Visual inspection of the MD simulation results indicates that partial dislocations are nucleated from the bicrystal interface at the displacement associated with maximum tensile stress nearly simultaneously on two different slip systems for each misorientation. The activated slip systems in each case are in agreement with those predicted using a Schmid factor analysis. Trailing partial dislocations are not nucleated from the interface during deformation, in agreement with the work of Van Swygenhoven et al. [32].

Fig. 25(b) shows the maximum tensile stress achieved during the deformation process as a function of interface misorientation angle. To isolate the influence of lattice orientation on the magnitude of the peak tensile stress, single crystal (SC) calculations are also presented in Fig. 25(b) for comparison. These calculations will be discussed in greater detail in Section 5. The orientation of each SC model is identical to that of the lower lattice region of the corresponding interface model; because the interfaces are of symmetric tilt character, the same geometric slip factors apply to the upper lattice region as well. The reference single crystal orientations have the same tilt axis relative to the direction of applied stress, with the same reference values for zero misorientation as the interface models to facilitate a direct comparison. For single crystal models, MD simulations indicate that dislocations are nucleated on the primary slip systems at the uniaxial tensile deformation associated with maximum tensile stress. Fig. 25(b) indicates that the orientation of the lattice with respect to the applied uniaxial tension is important for modeling the tensile strength of tilt interfaces with a $\{100\}$ misorientation axis. Note that the tensile stress required for dislocation nucleation for single crystal models is greater than that for bicrystal interface models, demonstrating the role of the interface in promoting dislocation nucleation.

Fig. 25(c) shows the maximum tensile stress achieved during uniaxial tension for interface models with a $\langle 110 \rangle$ misorientation axis as a function of interface misorientation angle.

Again, several single crystal calculations are reported to determine the role of the lattice orientation on the magnitude of the peak tensile stress. Fig. 25(c) shows that the coherent $\Sigma 3$ boundary has the highest tensile strength as compared with the other misorientations considered. This observation may be contrasted with the case of shear in which the coherent $\Sigma 3$ boundary showed a high propensity to migrate at low applied shear stresses [39]. An abrupt decrease is observed in the tensile strength as the misorientation angle of the interface is increased beyond 109.5° . Interfaces with misorientations greater than 109.5° are different from the other $\langle 110 \rangle$ boundaries in two respects: (i) boundaries in this range deform via dislocation nucleation on coplanar slip systems [138] and (ii) visual inspection indicates that boundaries in this range of $\langle 110 \rangle$ misorientations contain the E structural unit. Recall that Sansoz and Molinari concluded that boundaries that contained the E structural unit are prone to atomic shuffling when subjected to a shear deformation [39]. In this work, we find that symmetric tilt boundaries with a $\langle 110 \rangle$ misorientation axis that contain the E structural unit emit partial dislocations at low applied tensile stresses applied normal to the interface. Furthermore, the drop in tensile strength clearly is related directly to the interface structure, as the single crystal calculations do not indicate a discontinuous reduction in the stress required for dislocation emission as the misorientation angle of the interface is increased beyond 109.5° .

4.2. Asymmetric tilt grain boundaries

A full understanding of the dislocation nucleation behavior for $\Sigma 3$ ATGBs in Cu requires a discussion of the salient mechanisms. Three distinct mechanisms of dislocation nucleation occur for $\Sigma 3$ ATGBs, which can be categorized by inclination angle: low inclination angles ($\Phi \leq 35.26^\circ$), intermediate inclination angles ($35.26^\circ \leq \Phi \leq 70.53^\circ$), and high inclination angles ($\Phi \geq 70.53^\circ$). The dislocation nucleation mechanisms for Cu $\Sigma 3$ ATGBs provide similar observations for temperatures of 10 and 300 K. In this work, the authors present results for 10 simulations to minimize the thermal component on the observation of dislocation nucleation and emission from these boundaries. All boundaries in Section 4.2 have identical misorientations and only the GB plane (inclination angle) is altered. The following results show that GB plane can heavily influence dislocation nucleation mechanisms.

4.2.1. Stress required for dislocation nucleation

The stress–strain curves for Cu and Al under an applied uniaxial tensile strain were calculated at temperatures of 10 and 300 K for 11 $\Sigma 3$ boundaries. Fig. 26(a) shows stress–strain curves for Cu $\Sigma 3$ ATGBs at 300 K with inclination angles $\Phi < 45^\circ$. Since nucleation of the first partial at the GB coincides with the maximum tensile stress, $\sigma_{\max}^{\text{bc}}$, the simulations are stopped shortly after reaching the peak stress. Several other quantitative parameters can be calculated from the stress–strain response: the elastic stiffness K^{bc} , the maximum tensile stress $\sigma_{\max}^{\text{bc}}$, the strain corresponding to that stress $\varepsilon_{\max}^{\text{bc}}$, and the work per unit volume required for dislocation emission W^{bc} , where the superscript bc refers the bicrystal configuration. However, the focus of the following discussion is on the change in the dislocation nucleation stress as a function of inclination angle.

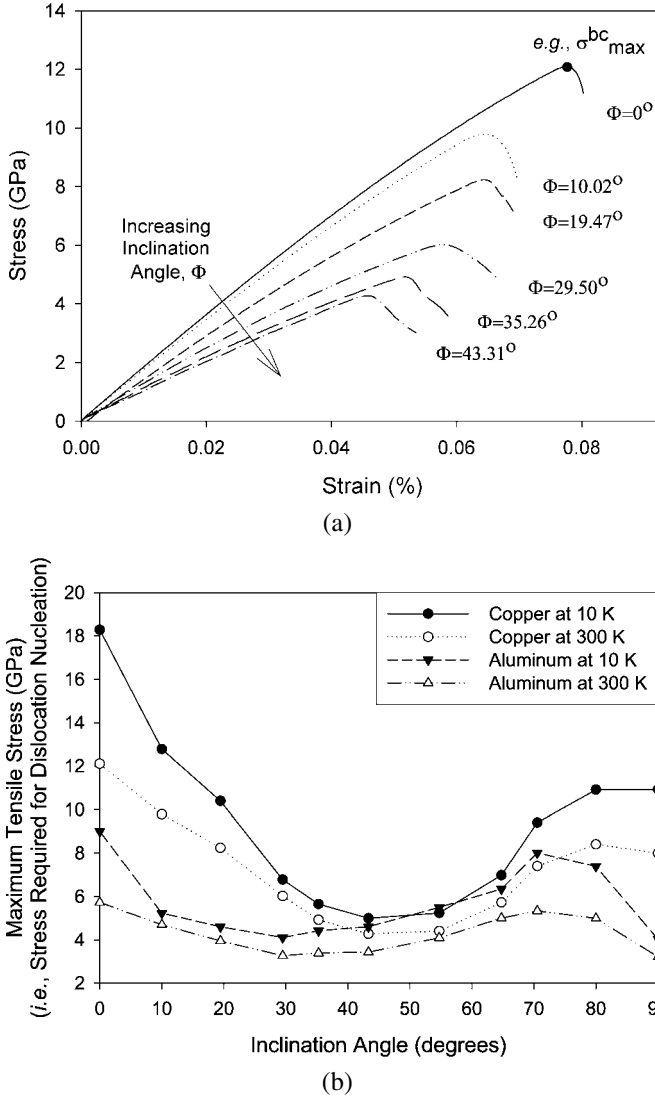


Fig. 26. (a) Example of stress–strain curves for $\Sigma 3$ grain boundaries with inclination angles below 45° at 300 K. (b) The change in the stress required for dislocation nucleation as a function of inclination angle for Cu and Al at 10 and 300 K. Reprinted from [19] with permission; © 2007 Elsevier.

Fig. 26(b) shows the peak stress values for all simulations. Recall that the peak stress σ_{\max}^{bc} is directly related to dislocation nucleation from the GB. First, the stress required for dislocation nucleation changes as a function of inclination angle. The magnitude of the change in stress values is greater as a function of inclination angle in Cu than in Al. The highest stress σ_{\max}^{bc} for both Al and Cu is at the $\Phi = 0^\circ$ coherent twin boundary. The lowest stress for Cu is at the $\Phi = 43.31^\circ$ GB while the lowest stress in Al is at the $\Phi = 29.50^\circ$

GB; both are boundaries of intermediate inclination angles. The $\Phi = 90^\circ$ incoherent twin boundary is between these values for Cu, and is near the low value in Al. This graph also shows a decrease in $\sigma_{\max}^{\text{bc}}$ with increasing temperature, especially near the symmetric twin boundaries ($\Phi = 0^\circ$ and $\Phi = 90^\circ$). The thermal component is expected to contribute to the dislocation nucleation process via the activation energy and activation volume associated with dislocation nucleation [139]. Of course, the 300 K case is overdriven in terms of kinetics, so in reality the drop of stress may be somewhat more pronounced at low strain rates (on the order of experimental strain rates). For example, at strain rate of 1 s^{-1} the number of atomic vibrations relative to the strain increment is 10^9 higher than that for a strain rate of 10^9 s^{-1} . However, MD simulations require time step increments on the order of femtoseconds, which commonly results in strain rates on the order of 10^9 s^{-1} for the calculation of dislocation nucleation phenomena. Due to the probabilistic nature of dislocation nucleation [140], when the number of dislocation nucleation attempts associated with thermal vibrations is increased, the probability of nucleating dislocations at a lower stress is increased for lower strain rates.

4.2.2. Low inclination angles ($\Phi \leq 35.26^\circ$)

At low inclination angles, the boundary is composed of large coherent twin boundary facets separated by smaller incoherent twin boundary facets, as shown in Fig. 15(a). Fig. 27 shows the $\Phi = 10.02^\circ$ Cu ATGB subjected to uniaxial tensile deformation normal to the interface plane at 10 K. In these images, only atoms with a centrosymmetry value greater than 0.25 are shown (i.e., distorted GB atoms, dislocations, and stacking faults). The x -direction is along the GB normal and the direction of the applied stress, the y -direction is along the GB period tangent to the interface, and the z -direction is along the tilt axis. Recall that the crystals adjoining the ATGBs have different lattice orientations in global coordinates. For the images in Fig. 27, the two boundaries contain crystal 1 [upper crystal in Fig. 4(a)]; crystal 2 is both above and below these boundaries (periodic with respect to simulation cell bounds in the x -direction). Finally, the images below the three-dimensional views correspond to projections of the lower interface onto the xy plane, with z normal to the view. A detailed characterization of the GB structure of the upper boundary in Figs 27(a)–27(c) is shown in Figs 28(a)–28(c).

Fig. 27(a) shows an oblique view of the interface after isobaric–isothermal equilibration, but prior to deformation. Notice the ledges formed by the intersection of coherent twin facets with incoherent twin facets, as in Fig. 28(a). Figs 27(b) and 28(b) show that the interface structure evolves prior to dislocation nucleation and emission from the boundary. Specifically, the D structural unit on the incoherent twin facet (the GB Shockley partial dislocation) dissociates into crystal lattice 1 on the $(11\bar{1})$ plane, leaving an intrinsic stacking fault. The arrows in Fig. 28(b) show the shift (slip) of atoms on the plane relative to their nearest neighbors, as visualized with the slip vector [135]. A Schmid factor analysis [138] of the slip systems in crystal 1 shows that this is a secondary slip plane for this crystal ($\text{SF}_{(111)}^{\max} = 0.148$) below all other possible slip planes ($\text{SF}_{(111)}^{\max} = \text{SF}_{(111)}^{\max} = 0.223$, $\text{SF}_{(111)}^{\max} = 0.371$), where $\text{SF}_{(hkl)}^{\max}$ is the maximum Schmid factor for all three slip directions on slip plane (hkl) . Additional tensile strain causes partial edge dislocations to nucleate where the dissociated Shockley partial dislocation intersects the coherent and incoherent

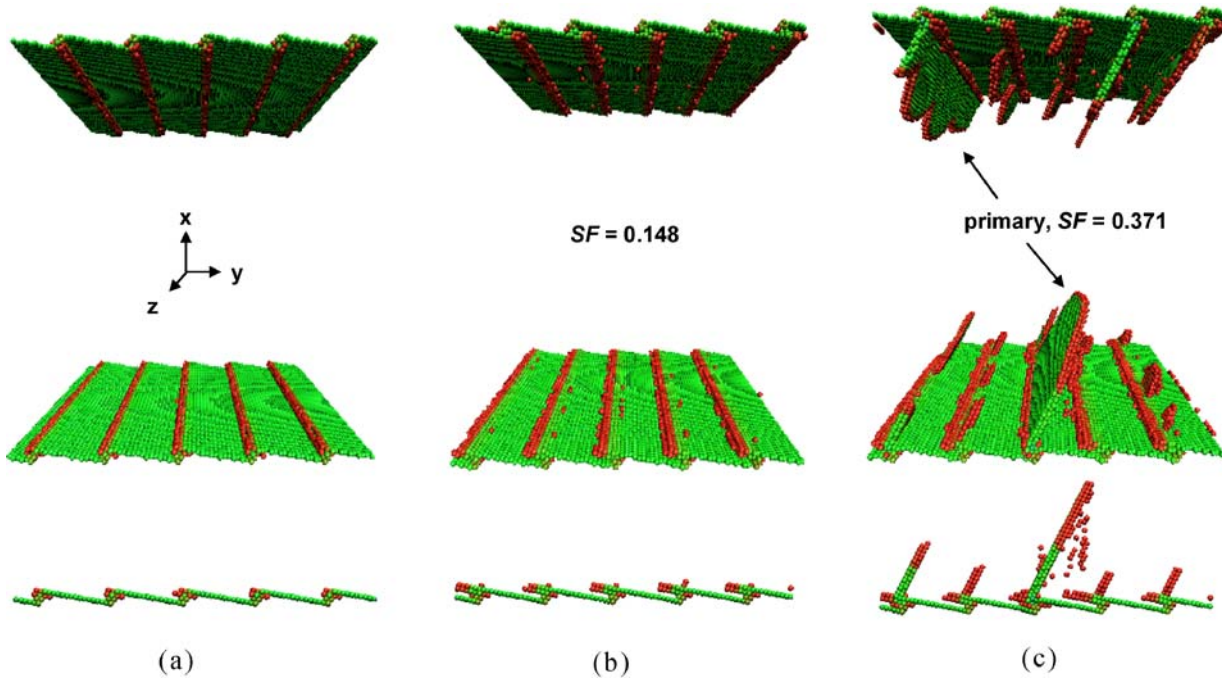


Fig. 27. Uniaxial tensile deformation of the $\Sigma 3$ $\Phi = 10.02^\circ$ asymmetric tilt grain boundary in Cu at 10 K. The different views represent (a) the faceted structure prior to deformation, (b) the dissociation of partial dislocations prior to dislocation nucleation, and (c) the nucleation of partial dislocation loops that are emitted into crystal 1. Only atoms in a non-centrosymmetric environment are shown. The top image is a three-dimensional oblique view and the bottom image is an orthonormal view from the $[1\bar{1}0]$ direction. Reprinted from [19] with permission; © 2007 Elsevier.

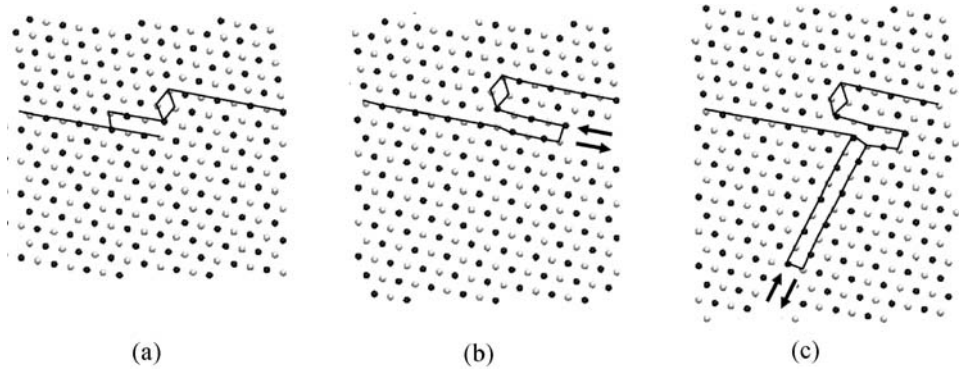


Fig. 28. Detailed view of the evolution of structure for the $\Sigma 3 \Phi = 10.02^\circ$ asymmetric tilt grain boundary in Cu at 10 K. The images correspond to the upper boundary in Figs 27(a)–27(c). The structures are viewed along the $[1\bar{1}0]$ direction and the atoms on two consecutive $\{220\}$ planes are shown as black and white. The arrows correspond to the relative shift in atoms compared to their nearest neighbors as measured by the slip vector [135]. Notice that the dislocation nucleates on a different $\{111\}$ plane than the dissociated glissile partial dislocation from the boundary. Reprinted from [19] with permission; © 2007 Elsevier.

twin facets, as shown in Figs 27(c) and 28(c). The partial dislocations nucleate as a dislocation loop on the (111) plane with both edge and screw character, unlike the planar dissociation of the GB partial edge dislocations in Fig. 27(b). Since the primary slip plane for dislocation nucleation is different from the dissociative plane, the change in slip planes may serve as a nucleation barrier resulting in high peak stresses $\sigma_{\max}^{\text{bc}}$ required for dislocation nucleation in low inclination angle $\Sigma 3$ ATGBs [cf. Fig. 26(b)]. Further tensile strain leads to the dislocation loops merging to form a continuous dislocation line as well as propagating further into the lattice. Although not shown, this is also accompanied by a decrease in the length of the dissociated GB Shockley partial and ISF.

Interestingly, upon closer examination of the dislocation nucleation mechanism for this boundary, we find that the dissociated glissile partial dislocation does not cross slip onto the high resolved shear stress slip plane. In fact, a partial dislocation loop homogeneously nucleates on the (111) slip plane near the dissociated D structural unit. This is most likely associated with a local stress concentration near the intersection of the two facets, which may act similarly to a boundary ledge in this respect. Due to the close proximity, the partial dislocation is quickly absorbed into the nearby boundary, giving the appearance of heterogeneous dislocation nucleation. However, this mechanism requires a very high stress, which may preclude most grain boundaries. The implications of this mechanism on grain boundary sources in nanocrystalline copper are discussed further in Section 6.1.

4.2.3. Intermediate inclination angles ($35.26^\circ < \Phi < 70.53^\circ$)

Fig. 29 shows dislocation nucleation and emission from the $\Phi = 54.74^\circ$ ATGB in Cu at 10 K. The images for Fig. 29 are presented in an identical manner to those in Fig. 27. The magnified view of the GB structure is also shown in Figs 30(a)–30(c). At intermediate inclination angles, the ratio of the length of the coherent twin facet to the incoherent twin facets is around unity [cf. Fig. 15(c)]. Additionally, the short length of the facets leads to

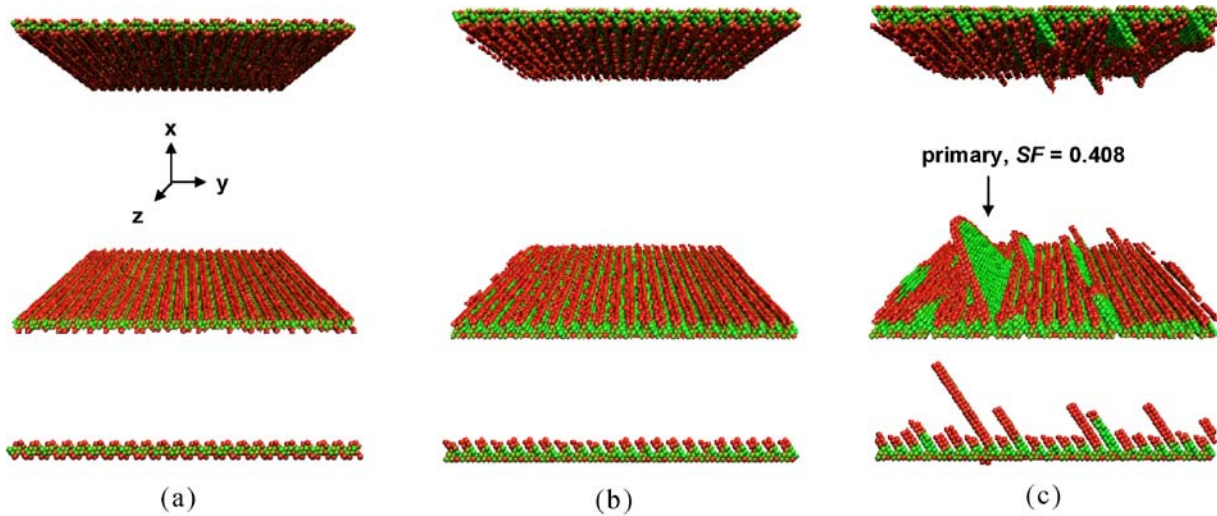


Fig. 29. Uniaxial tensile deformation of the $\Sigma 3$ $\Phi = 54.74^\circ$ asymmetric tilt grain boundary in Cu at 10 K. The images are rendered the same as those in Fig. 27. Reprinted from [19] with permission; © 2007 Elsevier.

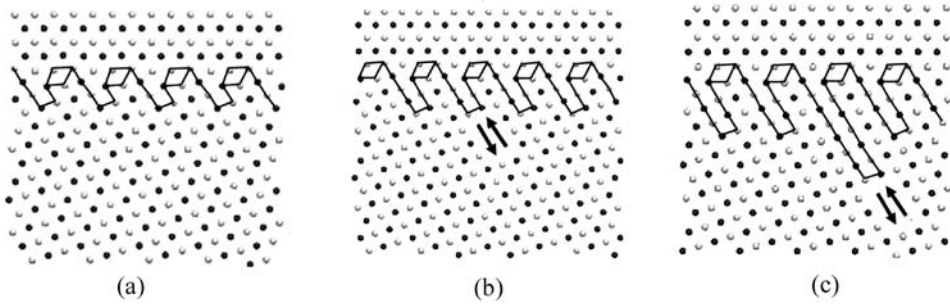


Fig. 30. Detailed view of the evolution of structure for the $\Sigma 3 \Phi = 54.74^\circ$ asymmetric tilt grain boundary in Cu at 10 K. These images correspond to the upper boundary in Figs 29(a)–29(c) and are viewed as in Fig. 28. Note that the dislocation nucleates on the same $\{111\}$ plane as the dissociated glissile partial dislocation from the boundary. Reprinted from [19] with permission; © 2007 Elsevier.

a higher number of facet intersections, or ledges, in the boundary. This is evident from the oblique view of the interface after isobaric–isothermal equilibration in Fig. 29(a).

In Figs 29(b) and 30(b), prior to dislocation nucleation, the application of a tensile strain perpendicular to the boundary causes the glissile partial dislocations (i.e., D structural units) to further dissociate from the incoherent twin facet into crystal lattice 1 on the $(11\bar{1})$ plane. This is similar to the pre-nucleation behavior observed at low inclination angles for $\Sigma 3$ ATGBs. However, for intermediate inclination angles, this is the primary slip plane for crystal 1 ($SF_{(11\bar{1})}^{\max} = 0.408$). Prior to the peak stress, the dissociation is planar, i.e., the dislocations each dissociate an equal distance (approximately) from the boundary. As the stress reaches the peak tensile stress, Figs 29(c) and 30(c), the first partial dislocations are nucleated on the $(11\bar{1})$ slip plane, the same slip plane onto which partial dislocations dissociated. Notice that not all dissociated partial dislocations are emitted from the boundary; some are retained. The spacing between dissociated structural units may serve as a critical length scale that influences the number of partial dislocations nucleated on the primary slip system. As with the low inclination angle $\Sigma 3$ ATGBs, the partial dislocations emitted into the lattice are dislocation loops with edge and screw dislocation character and the trailing partial is not observed in Cu. In addition, since the primary slip plane for dislocation nucleation is the same as the dissociative plane, the barrier for nucleation is lower which results in a low peak stresses σ_{\max}^{bc} required for dislocation nucleation in $\Sigma 3$ ATGBs within this inclination range [cf. Fig. 26(b)].

4.2.4. High inclination angles ($\Phi \geq 70.53^\circ$)

Fig. 31 shows dislocation nucleation for the $\Phi = 79.98^\circ$ ATGB in Cu at 10 K. Recall that at inclination angles $\Phi \geq 70.53^\circ$, the structure exhibits the 9R phase in Cu, as shown in Fig. 16. The 9R phase structure in Fig. 16 is identical to the 9R structure in Fig. 31(a), after isobaric–isothermal equilibration, which is rendered using the centrosymmetry parameter as in Figs 27 and 29. Fig. 31(b) shows that the 9R phase structure evolves prior to dislocation nucleation in the $\Phi = 79.98^\circ$ ATGB. Again, tensile strain perpendicular to the boundary causes the dissociation width for the glissile partial dislocations (D structural

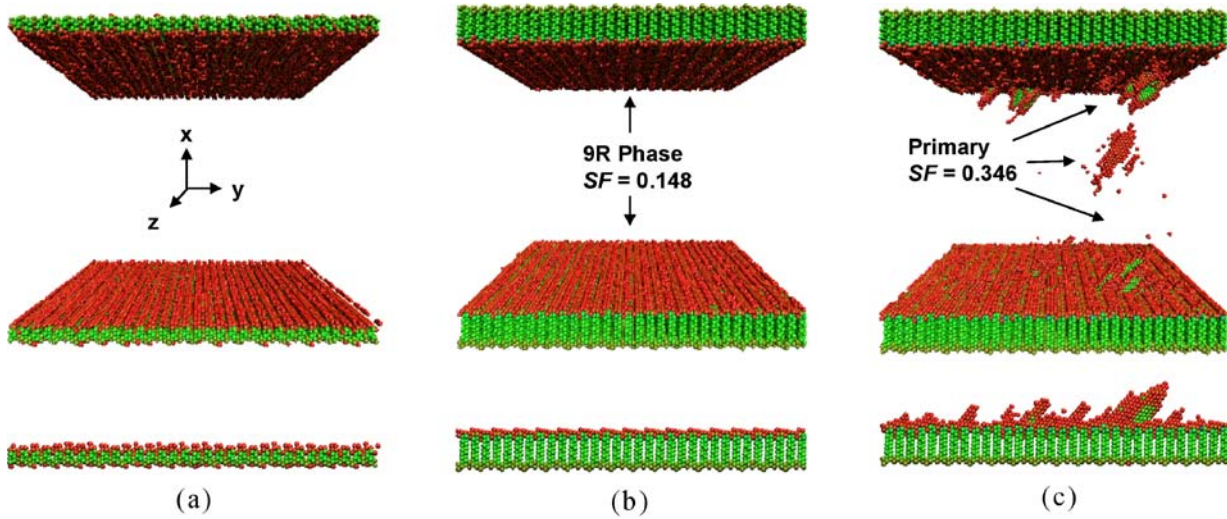


Fig. 31. Uniaxial tensile deformation of the $\Sigma 3\Phi = 79.98^\circ$ asymmetric tilt grain boundary in Cu at 10 K. The images are rendered the same as those in Figs 27 and 29. Reprinted from [19] with permission; © 2007 Elsevier.

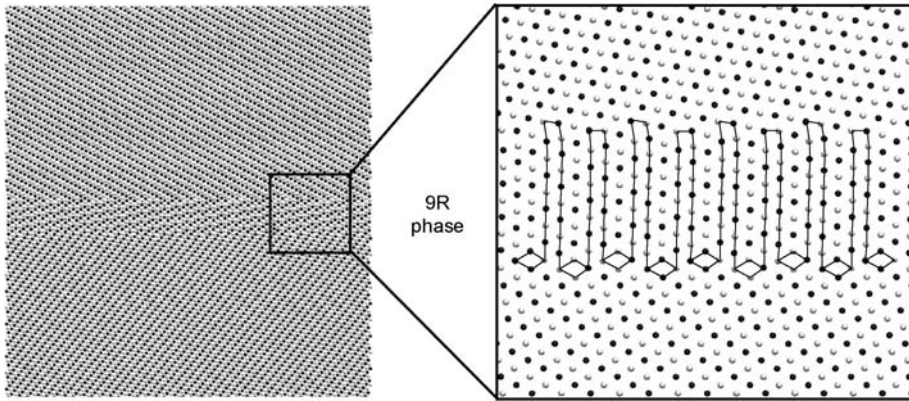


Fig. 32. Detailed images of the structure of the $\Sigma 3 \Phi = 79.98^\circ$ asymmetric tilt grain boundary in Cu at 10 K. These images show the interface structure just prior to dislocation nucleation. The images are viewed similarly to Figs 15 and 16 where black and white atoms represent consecutive $(2\bar{2}0)$ planes. The magnified view (on right) shows the extended dissociation of the glissile partial dislocation (i.e., D structural unit), which expands the 9R phase. Reprinted from [19] with permission; © 2007 Elsevier.

units) to increase towards crystal lattice 1 on the $(11\bar{1})$ plane. This is similar to the pre-nucleation behavior observed at low and intermediate inclination angles for $\Sigma 3$ ATGBs, but the dissociation width perpendicular to the boundary is larger due to the presence of the low energy 9R phase.

Fig. 32 shows images of the 9R phase on the lower boundary just prior to dislocation nucleation in the lattice. This image is rendered similarly to Figs 15 and 16, where black and white atoms represent successive $(2\bar{2}0)$ planes and distorted atoms are identified using the centrosymmetry parameter. In the enlarged view of the boundary (right), the expansion of the 9R phase results from partial dislocations further dissociating from the incoherent twin facet. The 9R phase is clearly visible in this view, with an intrinsic stacking fault on every third $(11\bar{1})$ plane, resulting in an ABCBCACAB stacking sequence. Unlike intermediate inclination angles, the dissociation plane is not the primary slip plane for crystal 1. Schmid factor analyses shows that this is a secondary slip plane ($SF_{(11\bar{1})}^{\max} = 0.148$); the primary slip planes ($SF_{(\bar{1}11)}^{\max} = SF_{(1\bar{1}1)}^{\max} = 0.346$) have normal vectors that are not orthogonal to the $[1\bar{1}0]$ tilt axis, unlike boundaries with lower inclination angles (Figs 27–30). For high inclination angles, partial dislocations nucleate both at the low angle boundaries *and* within the lattice on the $(\bar{1}11)$ and $(1\bar{1}1)$ slip planes; the partials propagate as dislocation loops. Interestingly, the dislocations nucleate nearly simultaneously on both primary slip planes at the nucleation sites. Furthermore, the dislocation loop contains a longer intrinsic stacking fault along the direction contained by both slip planes, although this direction has a slightly lower Schmid factor ($SF_{(\bar{1}11)[110]}^{\max} = SF_{(1\bar{1}1)[110]}^{\max} = 0.289$).

4.2.5. Preferential dislocation nucleation in Cu

Partial dislocations preferentially nucleate into only one crystal lattice; this is characteristic of all $\Sigma 3$ ATGBs. In fact, all $\Sigma 3$ ATGBs nucleate partial dislocations into crystal 1 [see

Fig. 4(a)]. This phenomenon is as expected for ATGBs with inclination angles $\Phi < 25.24^\circ$, for which $SF_{(hkl)}^{\max}$ is highest in crystal 1. However, the preferential dislocation nucleation in crystal 1 is observed for all ATGBs in this study, despite a higher $SF_{(hkl)}^{\max}$ in crystal 2 for all inclination angles $\Phi > 25.24^\circ$. This preferred nucleation is in contrast to the dislocation nucleation simulations in symmetric tilt GBs [16,17] with $\langle 100 \rangle$ and $\langle 110 \rangle$ tilt axes. With lattice orientations that are symmetric with respect to the GB plane, Spearot and coworkers showed that partial dislocations are nucleated and emitted into both lattices once the peak tensile stress is reached. For $\Sigma 3$ ATGBs, dislocation emission into crystal 2 only occurs at high strains after excessive dislocation emission severely alters the initial GB structure.

The observation of preferential dislocation nucleation depends on the arrangement of glissile partial dislocations within the boundary and their character. For all $\Sigma 3$ ATGBs in this study, the glissile partial dislocation (dissociated D structural unit) dissociates into crystal 1 for the minimized energy grain boundary structure. These dissociated partial dislocations are integral to dislocation nucleation in $\Sigma 3$ ATGBs. The uniaxial tensile strain merely resolves into stress components acting to overcome the stacking fault energy penalty that restricts glide of these partial dislocations into the lattice. So it appears that the preferential dislocation nucleation event can be traced back to the minimum energy structure. Perhaps the most important question is why does this partial dislocation dissociate into crystal 1 for the minimum energy grain boundary structure? Interestingly, the elastic modulus is higher in crystal 1 for all inclination angles. The local relaxation of the dislocation content of the ATGBs may result in any glissile partial dislocation content dissociating into the adjoining crystal with the higher elastic modulus. The boundary structure, particularly the dissociated glissile partial dislocation, serves as the impetus for dislocation nucleation in $\Sigma 3$ ATGBs.

5. Models for dislocation nucleation: single crystals and GBs

A simple model is proposed to correlate tensile interface strength, which is associated with the emission of partial dislocations, and certain first-order characteristics of the interface structure. The aim of the proposed model is to illustrate the impact of interfacial porosity and non-glide direction stresses on tensile interface strength. This model is developed through the following two step process. First, MD simulation results for uniaxial tensile deformation of *single crystal* models are used to isolate the influence of lattice orientation on the maximum tensile stress associated with *homogeneous* dislocation nucleation (Section 5.1). Once the effect of lattice orientation has been isolated, the second step in the development of the interface strength model is to incorporate a dependence on inherent GB properties, such as the free volume content of the interface, to predict the maximum tensile stress associated with *heterogeneous* dislocation nucleation (Section 5.2).

5.1. Homogeneous dislocation nucleation in single crystal Cu

5.1.1. Influence of resolved stresses

Fig. 33 illustrates on a stereographic triangle the single crystal orientations which are deformed in uniaxial tension to capture the role of lattice orientation on dislocation nucleation

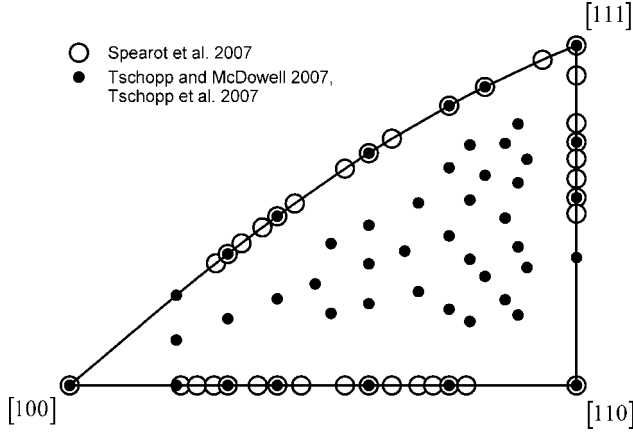


Fig. 33. Stereographic triangle showing the uniaxial loading axis orientations investigated in the single crystal deformation simulations.

strength [18]. Several orientations along the [100]–[110], [100]–[111], and [111]–[110] boundaries (open circles) are selected, which relate directly to the orientations associated with the $\langle 100 \rangle$ and $\langle 110 \rangle$ STGBs (recall Fig. 25). Specifically, the [100]–[110] boundary of the stereographic triangle corresponds to the lattice orientations of the $\langle 100 \rangle$ STGBs, while the [100]–[111] and [111]–[110] boundaries correspond to the $\langle 110 \rangle$ STGBs. The filled-in circles in Fig. 33 refer to subsequent MD studies that examine the effect of single crystal orientation on the stress required for dislocation nucleation over a wider range of orientations [73,141], which are discussed in Section 5.1.2.

Single crystal calculations by Spearot et al. [18] have clearly shown that the partial dislocation *nucleation* process in single crystal (SC) models shows non-Schmid character, as the critical resolved shear stress varies as a function of orientation. These observations are in agreement with *ab initio* calculations by Ogata et al. [72] who performed a systematic study of the effect of non-Schmid components on dislocation nucleation and reported that compressive stresses acting normal to the slip plane can affect the shear stress required for dislocation emission. To characterize the evolution of the resolved shear stress required for dislocation nucleation, non-glide direction stress components acting on the slip plane must be taken into consideration [72,142–144]. Accordingly, the relationship

$$\sigma_{\max}^{\text{sc}} = \frac{\tau_{\text{ideal}}}{\mu_s \text{SF} + \mu_n \text{NF} + \mu_p \text{PF}} \quad (12)$$

was initially proposed [18] for *single crystals* subjected to uniaxial tensile stress, where

$$\text{SF} = \ell_{y'y} \ell_{x'y}, \quad \text{NF} = \ell_{y'y}^2, \quad \text{PF} = \ell_{y'y} \ell_{z'y}. \quad (13)$$

Here, $\ell_{i',j}$ are the direction cosines relating a coordinate axis fixed to the slip plane (X' is the slip direction, Y' is normal to the slip plane and Z' lies within the slip plane, perpendicular to the slip direction [138]) to a fixed specimen coordinate system (X , Y loading direction, and Z). These direction cosines pertain to the initial (undeformed) configuration of the crystal. Thus, SF projects the uniaxial applied stress into the resolved shear stress

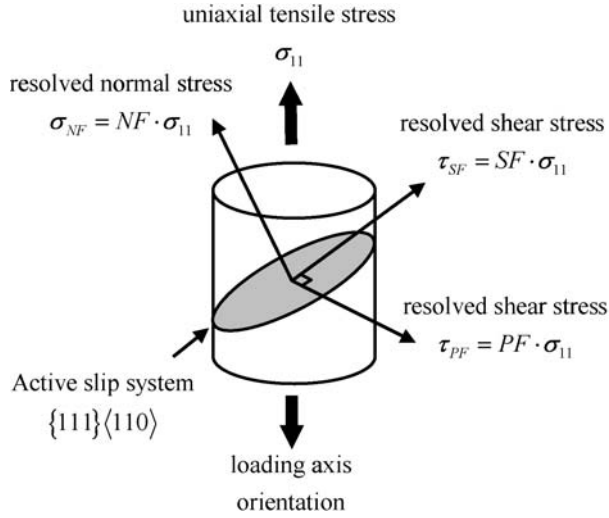


Fig. 34. Schematic showing how the uniaxial tensile stress is resolved into stress components acting upon the active slip system.

acting on the slip plane in the slip direction (the conventional Schmid factor), NF projects the uniaxial stress into the stress normal to the slip plane, and PF projects the uniaxial stress into a shear stress acting on the slip plane perpendicular to the slip direction (co-slip direction). The active slip system is defined by the maximum SF among all possible slip systems. Fig. 34 shows a schematic of how the uniaxial tensile stress is resolved onto the active slip system given the above definitions. Fig. 35 shows the change in the Schmid factor SF and the normal factor NF as a function of loading orientation within a stereographic triangle. The maximum $SF = 0.5$ occurs within the interior of the stereographic triangle, while the maximum $NF = 0.666$ occurs for the $[110]$ loading direction. The minimum Schmid factor, $SF = 0.272$, and normal factor, $NF = 0.111$, both occur for the $[111]$ orientation.

In eq. (12), the ideal shear strength, τ_{ideal} , is defined as the resolved shear stress required for partial dislocation nucleation when all other stress components acting on the slip plane are zero. *Ab initio* calculations by Ogata et al. [72] find that $\tau_{ideal} = 2.16$ GPa for copper. The parameters μ_s , μ_n and μ_p are positive scalars used to characterize the degree of non-Schmid behavior. Therefore, an increase in any of the coefficients μ_s , μ_n or μ_p reduces the predicted peak stress required for dislocation nucleation by increasing the weight of the corresponding stress component. If $\mu_s = 1$ and $\mu_n = \mu_p = 0$, the proposed model reduces to Schmid's law for single crystal slip, i.e., $\sigma_{max} = \tau_{ideal}/SF$.

Least squares regression is used to determine appropriate values for μ_s , μ_n and μ_p for loading axis orientations along the $[100]$ – $[110]$ boundary of the misorientation triangle ($\langle 100 \rangle$ STGBs) as well as the $[100]$ – $[111]$ and $[111]$ – $[110]$ boundaries ($\langle 110 \rangle$ STGBs). Parameters are fit separately for models with $\langle 100 \rangle$ and $\langle 110 \rangle$ misorientation axes by minimizing the sum of the squares of the residual error between the calculated peak tensile stress data and the values predicted via eq. (12). This analysis indicates that dislocation

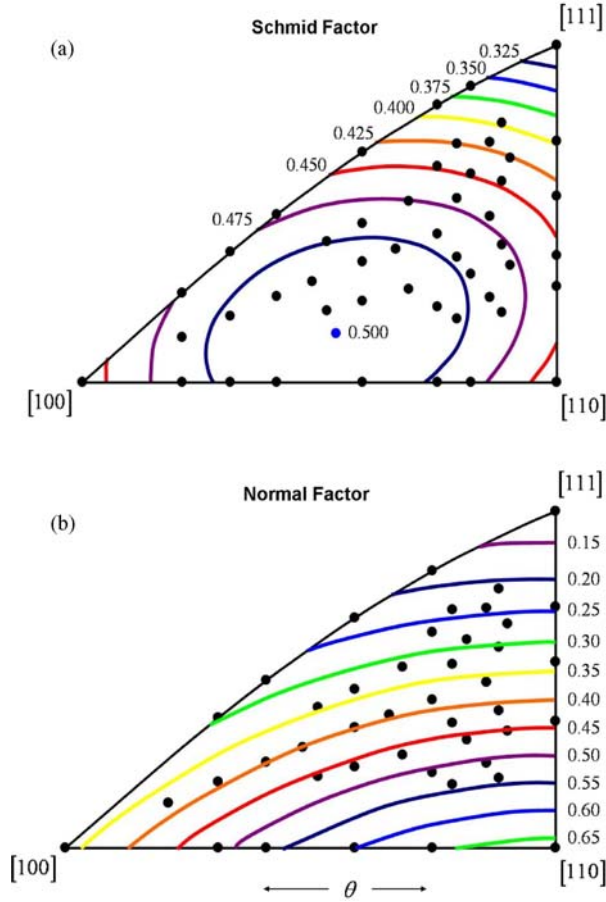


Fig. 35. Orientation dependence of the (a) Schmid factor SF and (b) normal factor NF for FCC crystals.

nucleation can be correlated to specific regions within the stereographic triangle where SF is greater than NF, or vice versa. Fig. 36 shows that the proposed relationship [eq. (12)] correlates well with the MD simulations for uniaxial tension of single crystals at various orientations along the [100]–[110], [100]–[111], and [111]–[110] boundaries. The normal factor (NF) is essential to describe dislocation nucleation in $\langle 100 \rangle$ single crystal models ($\mu_s = 0$, $\mu_p = 0.69$), while the maximum tensile stress required for dislocation nucleation in $\langle 110 \rangle$ single crystal models correlates more strongly with the SF parameter ($\mu_s = 0.60$, $\mu_p = 0.0$). This analysis for FCC Cu has shown that the co-slip factor has essentially no effect ($\mu_p = 0$) on the stress required for dislocation nucleation [18]. The co-slip factor resolves the shear stress in the [112] direction on the {111} slip plane. Typically, the non-Schmid parameter PF is used to modify the driving force for cross-slip of screw dislocations in body-centered cubic metals (cf. [145]). Unfortunately, Fig. 36 indicates that the SC model presented in eq. (12) cannot capture the continuing drop in stress between the

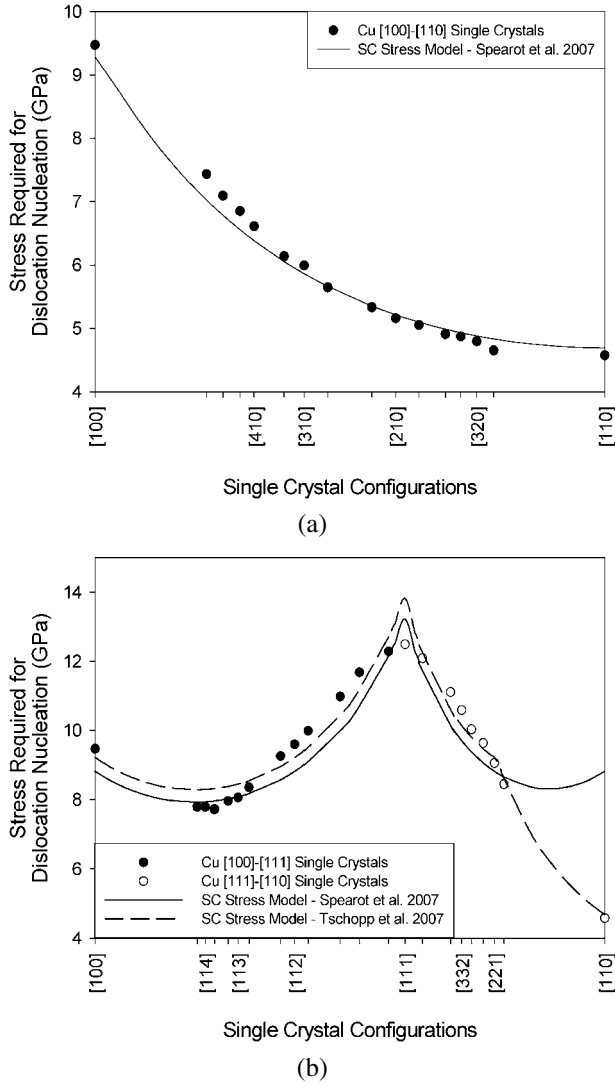


Fig. 36. Stress required for dislocation nucleation during uniaxial tensile deformation in single crystals and grain boundaries as a function of crystallographic orientation and misorientation, respectively. Single crystal data corresponds to (a) the [100]–[110] boundary ($\langle 100 \rangle$ STGBs) as well as (b) the [100]–[111] and [111]–[110] boundaries ($\langle 110 \rangle$ STGBs).

[221] and [110] orientations along the [111]–[110] boundary. This limitation is resolved in Section 5.1.2 [73].

To further illustrate the relative differences in the roles of SF and NF on dislocation nucleation for uniaxial tension of atomistic models with $\langle 100 \rangle$ and $\langle 110 \rangle$ misorientation axes, Figs 37(a) and 37(b) show the magnitudes of SF and NF, respectively, against the maximum tensile stress required for dislocation nucleation in single crystal samples. In general,

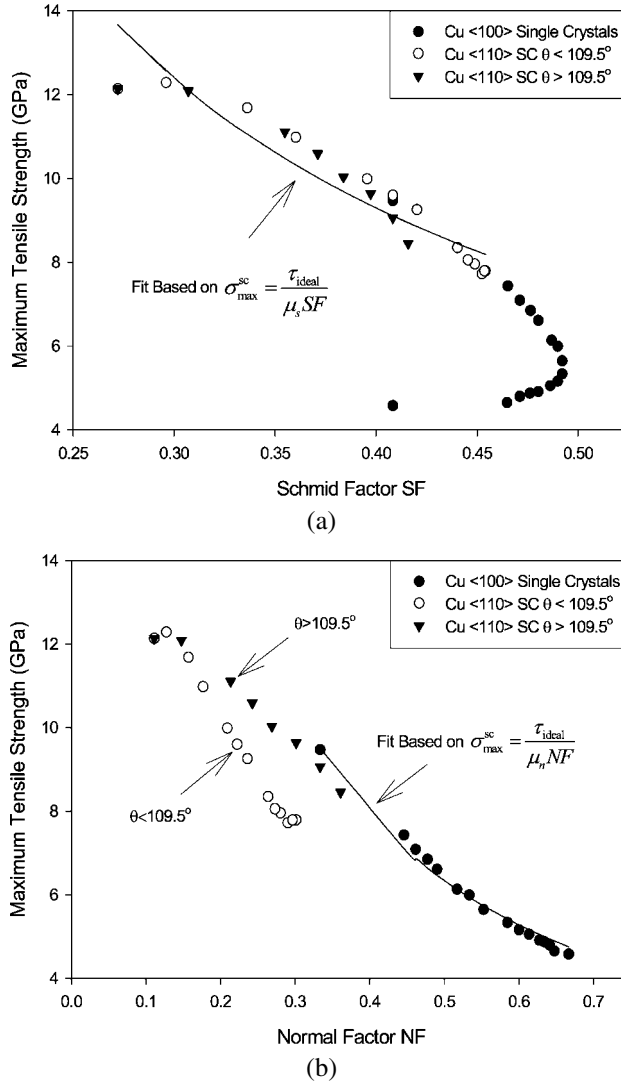


Fig. 37. Stress required for dislocation nucleation in single crystals as a function of (a) the Schmid factor parameter (SF) and (b) the normal factor (NF) parameter. Reprinted from [18] with permission; © 2007 Elsevier.

Fig. 37(a) shows that for small SF values (small resolved shear stress in the direction of slip) the tensile stress required for dislocation nucleation is greater than that at higher SF values. However, for some $\langle 100 \rangle$ orientations, the maximum tensile stress values deviate from this general trend, revealing that SF alone is incapable describing the nucleation stress for the $\langle 100 \rangle$ case. In Fig. 37(b), a similar trend is observed; as the NF magnitude increases, the stress required for dislocation nucleation decreases. In other words, an increase in the stress projected normal to the slip plane decreases the applied stress necessary to nucleate dislocations within the crystal lattice; this dependence on the normal stress has been

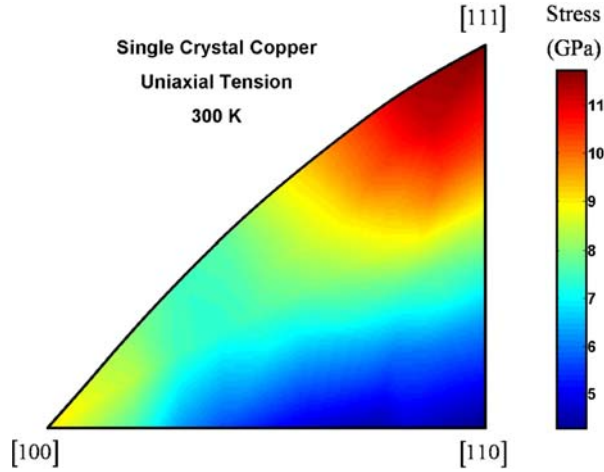


Fig. 38. Tensile stresses required for homogeneous dislocation nucleation as a function of the loading axis orientation for single crystal models at 300 K. Reprinted from [141] with permission; © 2007 American Institute of Physics.

observed using *ab initio* simulations by Ogata et al. [72]. Interestingly, the $\langle 110 \rangle$ curve displays the same general trend as the $\langle 100 \rangle$ data, but is divided into two regions: $\theta < 109.5^\circ$ and $\theta > 109.5^\circ$. The $\Sigma 3$ coherent twin boundary ($\theta = 109.5^\circ$) separates these two regions, delineating the transition between active slip systems for the two regions. The two active slip systems for the $\theta < 109.5^\circ$ single crystal orientations occur on different slip planes while the two slip systems for $\theta > 109.5^\circ$ are on the same slip plane (coplanar slip).

5.1.2. Second generation model for dislocation nucleation in single crystals

To provide a more complete correlation between SF, NF and the dislocation nucleation stress for all possible loading orientations requires atomistic simulations of SC models with orientations both on the exterior (multiple active slip systems) and interior (single slip) of the stereographic triangle. Fig. 33 shows a stereographic triangle with the 49 tensile axis orientations (filled-in circles) used to investigate the orientation dependence of homogeneous dislocation nucleation for single crystal Cu [73,141]. The expected slip system (maximum Schmid factor) is the $(11\bar{1})$ [101] slip system for all tensile axis orientations on the interior of the [100]–[110]–[111] triangle. Note that all the interior tensile axis orientations deform via single slip on the $(11\bar{1})$ [101] slip system, while all tensile axis orientations on the boundary of the stereographic triangle have at least two active slip systems.

The stress required for dislocation nucleation is calculated for all tensile axis orientations examined in this work. Fig. 38 shows a contour plot of the stress required for dislocation nucleation as a function of the tensile axis orientation on the stereographic triangle at 300 K. All intermediate tensile axis orientations in the stereographic triangle are obtained through linear interpolation. The [111] axis requires the largest tensile stress for dislocation nucleation while the [110] axis requires the lowest tensile stress for dislocation nucleation. The stress along the [100]–[110] boundary is relatively unchanged near the [110] vertex of

Table 1

Parameters used in the model for homogeneous dislocation nucleation stress [eq. (16)] in single crystals at both 10 and 300 K

Temperature (K)	τ_{ideal} (GPa)	SF-dominated region		NF-dominated region	
		$\mu_{s,1}$	$\mu_{n,1}$	$\mu_{s,2}$	$\mu_{n,2}$
10	2.16	0.574	0.000	0.000	0.693
300	2.16	0.396	0.000	0.037	0.473

the stereographic triangle; this trend is similar to the normal factor contour in Fig. 35(b). All other regions of the contour plot in Fig. 38 appear very similar to the Schmid factor contours in Fig. 35(a).

A second-generation model is proposed to correlate the stress required for dislocation nucleation using both SF and NF. The aim of this model is to isolate the influence of lattice orientation with respect to the uniaxial tensile axis on the homogeneous dislocation nucleation event. Recall that the relationship given in eq. (12) is unable to capture the effect on dislocation nucleation stress for all orientations, specifically orientations along the [111]–[110] boundary as shown in Fig. 36(b). Previous calculations of single crystal dislocation nucleation along the exterior orientations of the stereographic triangle show that the [100]–[110] boundary correlates best with NF and the [100]–[111] boundary correlates best with SF. This indicates that dislocation nucleation is driven by different resolved stresses in two regions within the stereographic triangle: a SF-dominated region and an NF-dominated region.

The aforementioned model in eq. (12) is separated into a piecewise form to capture the stress required for dislocation nucleation from all orientations within the stereographic triangle as well as the transition between the NF-dominated dislocation nucleation along the [100]–[110] boundary to the SF-dominated dislocation nucleation along the [100]–[111] boundary. The following criterion is used to identify the transition between these two regions within the stereographic triangle, i.e.,

$$\sigma_{\text{max}}^{\text{sc}} = \begin{cases} \frac{\tau_{\text{ideal}}}{\mu_{s,1}\text{SF} + \mu_{n,1}\text{NF}}, & \text{if } (\mu_{s,1}\text{SF} + \mu_{n,1}\text{NF}) \geq (\mu_{s,2}\text{SF} + \mu_{n,2}\text{NF}), \\ \frac{\tau_{\text{ideal}}}{\mu_{s,2}\text{SF} + \mu_{n,2}\text{NF}}, & \text{if } (\mu_{s,1}\text{SF} + \mu_{n,1}\text{NF}) < (\mu_{s,2}\text{SF} + \mu_{n,2}\text{NF}), \end{cases} \quad (14)$$

where $\mu_{s,i}$ and $\mu_{n,i}$ are fitting coefficients for the Schmid factor and normal factor; $i = 1$ corresponds to the SF-dominated dislocation nucleation region and $i = 2$ corresponds to the NF-dominated dislocation nucleation region. Eq. (14) is formulated to allow a mild dependence on NF in an SF-dominated region, and vice versa. Fitting parameters and the posed criterion act as the additional constraint $[\tau_{\text{ideal}}/(\mu_{s,1}\text{SF} + \mu_{n,1}\text{NF}) = \tau_{\text{ideal}}/(\mu_{s,2}\text{SF} + \mu_{n,2}\text{NF})$ when $(\mu_{s,1}\text{SF} + \mu_{n,1}\text{NF}) = (\mu_{s,2}\text{SF} + \mu_{n,2}\text{NF})$] that forces a first-order transition between the SF and NF-dominated regions.

Least squares regression is then used to determine the appropriate values of $\mu_{s,1}$, $\mu_{n,1}$, $\mu_{s,2}$, and $\mu_{n,2}$ based on the data for homogeneous dislocation nucleation in single crystal Cu. The parameters for eq. (14) at 10 and 300 K are listed in Table 1. These parameters are obtained by minimizing the sum of squares of the residual error between the calculated stress data and the predicted values. Interestingly, by forcing $\mu_{s,i} \geq 0$ and $\mu_{n,i} \geq 0$, the

minimum sum of squares shows that the normal factor NF has no influence ($\mu_{n,1} = 0$ at 10 and 300 K) in the SF-dominated dislocation nucleation region, while the Schmid factor SF has minimal influence ($\mu_{s,2} = 0$ at 10 K and $\mu_{s,2} = 0.037$ at 300 K) on dislocation nucleation in the NF-dominated region. The second-generation model for $\langle 110 \rangle$ single crystal orientations is shown in Fig. 36(b). Dislocation nucleation for tensile axis orientations along the $[100]$ – $[110]$ boundary is entirely driven by resolved stress normal to the slip plane (the normal factor), while dislocation nucleation along the $[100]$ – $[111]$ boundary is entirely driven by the resolved shear stress in the direction of slip (the Schmid factor). This SC model is nearly identical to the SC model of Spearot et al. [18], with a slight difference in the fitting parameters for Fig. 36(b) resulting from the interior orientations of the stereographic triangle. However, the second generation single crystal dislocation nucleation model is also able to capture the transition between the SF-dominated response to NF-dominated response along the $[111]$ – $[110]$ boundary in Fig. 36(b), which the initial model was unable to capture. Linear regression of the calculated dislocation nucleation stress versus the predicted stresses using eq. (14) for all orientations in Fig. 33 indicates relatively good agreement and yields correlation coefficients of $R^2 = 0.886$ (10 K) and $R^2 = 0.920$ (300 K).

5.1.3. Dislocation nucleation in single crystals under uniaxial compression

The stress required for dislocation nucleation is also calculated for all orientations (open circles) in Fig. 33 for uniaxial compression. Fig. 39(a) shows a contour plot of the stress required for dislocation nucleation as a function of the compressive axis orientation on the stereographic triangle at 300 K. There is a distinctly different orientation dependence of the stress required for dislocation nucleation in tension (Fig. 38) and compression [Fig. 39(a)]. For example, notice that the $[110]$ axis requires the lowest stress for dislocation nucleation in tension and the $[100]$ axis requires the lowest stress in compression.

The difference between the calculated stresses required for homogeneous dislocation nucleation in uniaxial tension and compression may be due to how the stress is resolved normal to the active slip system. Fig. 40 shows a schematic of the differences in resolved stresses between (a) uniaxial tension and (b) uniaxial compression. The resolved normal stress to the slip plane is tensile (compressive) in uniaxial tension (compression) for the loading axis orientations. Fig. 40(c) shows that the tensile normal stress acts to increase the interplanar spacing between $\{111\}$ planes, which may allow easier nucleation of the partial dislocation loop by lowering the resistance to slip on adjoining $\{111\}$ planes. In addition, in uniaxial compression, the compressive normal stress on the $\{111\}$ planes acts to decrease the interplanar spacing between $\{111\}$ planes, which may increase the interatomic friction to slip along these planes. While this fundamental description of how the resolved normal stress affects dislocation nucleation agrees with the calculated results from most loading axis orientations, it does not agree with all orientations (specifically, near the $[100]$ axis as described below).

Fig. 39(b) shows the ratio of the stress required for homogeneous dislocation nucleation under compression to that in tension as a function of the loading axis orientation for single crystal copper. A ratio greater than unity signifies that homogeneous dislocation nucleation requires a higher stress in compression than in tension, and vice versa. Most orientations within the stereographic triangle require a higher stress in uniaxial *compression*

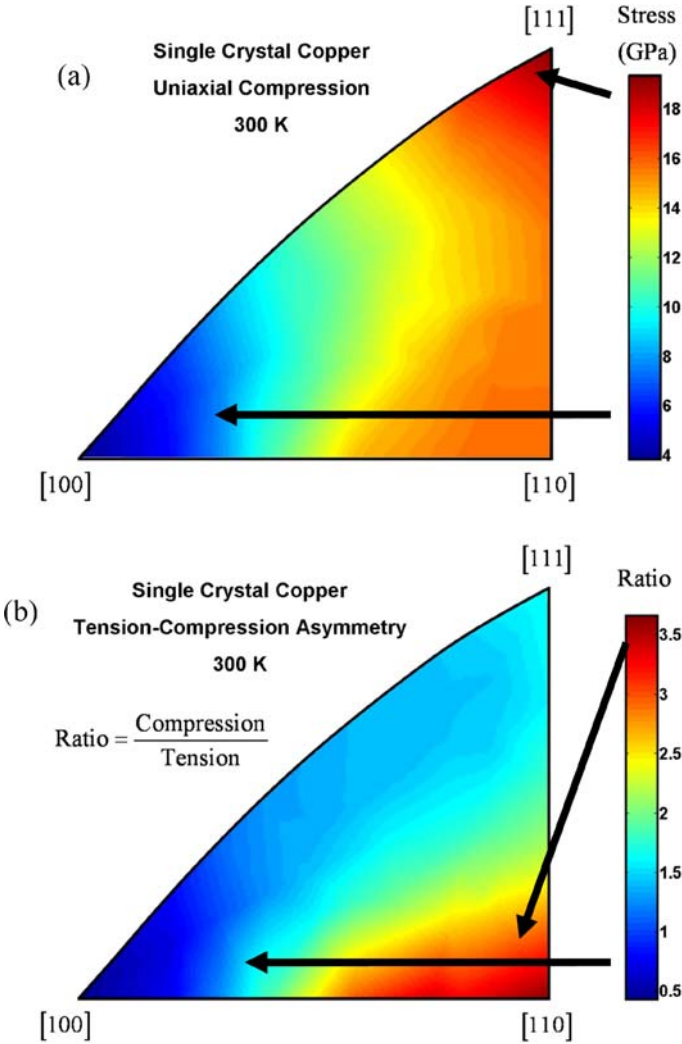


Fig. 39. (a) Compressive stresses required for homogeneous dislocation nucleation and (b) tension–compression asymmetry as a function of the loading axis orientation for single crystal models at 300 K. The tension–compression asymmetry is rendered by plotting the ratio of the stress required for homogeneous dislocation nucleation in uniaxial compression to that in uniaxial tension. Reprinted from [141] with permission; © 2007 American Institute of Physics.

tion to nucleate dislocations; the [110] axis has the largest ratio of 3.69 (15.58 GPa in compression/4.23 GPa in tension). This trend agrees with that discussed above for Fig. 40. Interestingly, not all orientations display this trend. Fig. 39(b) also shows that some axis orientations require a greater stress in uniaxial tension than uniaxial compression. Specifically, the [100] axis has the lowest ratio of 0.41 (3.71 GPa/9.12 GPa), showing a much

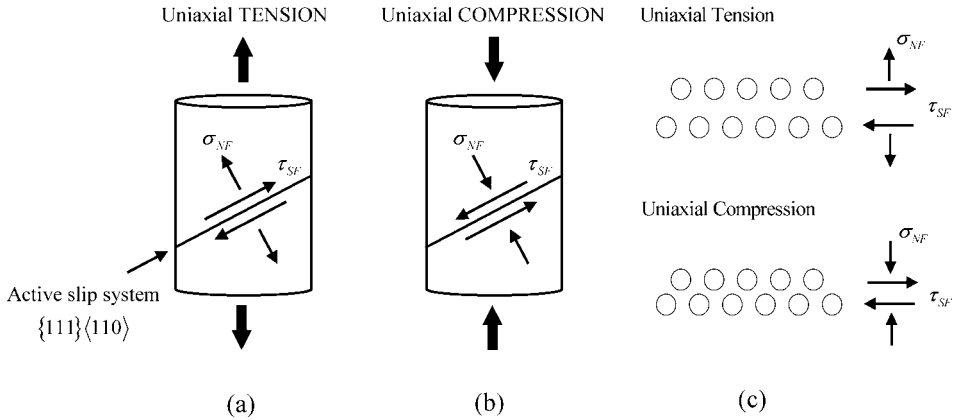


Fig. 40. Schematic showing the differences in resolved stresses on the active slip plane for (a) uniaxial tension and (b) uniaxial compression. At the atomic scale (c), the different directionality of the resolved normal stresses results in forces acting on the spacing of {111} planes, which may prove beneficial or detrimental to dislocation loop nucleation in single crystals depending on the loading.

greater propensity for homogeneous partial dislocation nucleation under an applied uniaxial compressive stress.

The asymmetry in dislocation nucleation stress between tension and compression has been of particular interest as material microstructure progresses towards nanometer scale dimensions. For example, Diao et al. [146] have shown that the yield strength asymmetry in Au nanowires for the [100] and [111] orientations are due to surface-induced internal stresses. Tomar and Zhou [147] related the yield strength asymmetry in nanocrystalline α -Fe₂O₃-fcc Al composites to differences in grain boundary sliding behavior. Lund and Schuh [148,149] have shown that nanocrystalline Ni has higher yield and flow stresses in compression than in tension (both uniaxial and biaxial simulations); these results suggest a similar atomic-level mechanism controls yield in both FCC Ni and metallic glasses [150]. Cheng et al. [151] proposed a pressure-dependent analytical model that predicts the tension/compression asymmetry of the yield strength in nanocrystalline Cu, Al, and BCC-Fe. Consequently, as the material length scale decreases to the nanoscale, tension–compression asymmetry is expected. While these studies have focused on inelastic deformation due to heterogeneities at the nanoscale, the influence of crystal orientation on dislocation nucleation in the *absence* of heterogeneities is also vital to a full understanding of inelasticity at the nanoscale. Therefore, the current MD simulations, which show a tension–compression asymmetry of dislocation nucleation in single crystals, agrees with previous simulations and analytical models that have shown a tension–compression asymmetry in the yield stress for nanocrystalline FCC metals [148,151], metallic glasses [150], and nanocrystalline α -Fe₂O₃-fcc Al composites [147]. Furthermore, studies of *homogeneous* dislocation nucleation in single crystals lend valuable insight that is complementary to modeling *heterogeneous* dislocation nucleation from interfaces [18].

5.1.4. Effect of lattice distortion on resolved stress components

The affine elastic distortion of the lattice during application of uniaxial stress prior to nucleation is significant in terms of rotation of the slip system and associated co-slip and slip plane normal directions. Here we consider how the strain to nucleation (on the order of 6–14%) can influence the resolved stress components in the current (deformed) configuration at the point of nucleation. To do this, the motion of the simulation cell boundaries was used to compute a deformation gradient tensor, \tilde{F}_{ij} , that maps the original orthogonal triad of unit vectors in the slip, co-slip and slip plane normal directions from the undeformed to the deformed configuration. The push-forward transformation

$$d_i^{\alpha*} = \tilde{F}_{im} d_m^{\alpha} \quad (15)$$

gives the deformed configuration components $d^{\alpha*}$ of these three unit vectors d^{α} , $\alpha = 1, 2, 3$ in the initial (undeformed) configuration.

These vectors are no longer orthogonal in the current configuration, having undergone stretch and rotation. The direction cosines ℓ_{ij} used in eq. (13) pertain to the resolution of Cauchy stress onto slip vectors d^{α} in the undeformed configuration. To provide a meaningful description of the resolved shear stress in the slip direction and the normal stress to the slip plane in the deformed configuration at the point of nucleation, we simply take a cross product of the deformed vectors in the slip and co-slip directions (which establish the slip plane tangent) to determine the slip plane normal direction. Then, a vector cross product of this slip plane normal direction with the deformed slip direction vector gives a modified co-slip direction, yielding an orthogonal triad which is then normalized to a set of unit vectors for defining an updated set of direction cosines in eq. (13). The slip direction and slip plane normal are preserved as primal descriptors.

Several calculations are performed to compare differences between using this rotated basis and the original undeformed basis of slip, co-slip and slip plane normal directions in eq. (13). First, the evolution of the Schmid factor was calculated as a function of strain for the 12 $\{111\}\langle 110 \rangle$ slip systems for the $[321]$ orientation under uniaxial tension at 10 K. The temperature of 10 K requires the largest strains for dislocation nucleation as a function of temperature and represents the upper bound for slip system rotation. The maximum Schmid factor $(11\bar{1})[101]$ slip system in the undeformed configuration has the highest SF value throughout uniaxial loading in tension. Even for large strain deformation (10% strain), the increase in SF on an individual slip system is not enough for another slip system to become the favored slip system, i.e., a higher SF than the $(11\bar{1})[101]$ slip system. For the remaining analyses, we assume that the $(11\bar{1})[101]$ slip system remains the active slip system throughout elastic deformation.

All crystal orientations around the stereographic triangle were sampled to find the approximate increase in the resolved stress parameters SF and NF at the strain associated with dislocation nucleation. In uniaxial tension at 10 K, SF and NF *decreased* by an average of 3% and 15%, respectively. In uniaxial compression at 10 K, SF and NF *increased* by an average of 2% and 20%, respectively. The changes in the resolved shear stress in the slip direction (i.e., SF) as a function of elastic deformation are minimal compared to the changes in the resolved stress normal to the slip plane (NF). Moreover, on average, the resolved stresses evolve differently in tension and compression; in tension the resolved stress components decrease and vice versa. However, while the evolution of resolved stress

components under tension and compression may partly explain the calculated tension–compression asymmetry, the magnitude of these changes are still small relative to the sign change for the resolved normal stress. For example, for the [321] orientation at 10 K, the change in the resolved shear stress due to lattice rotation is $\Delta\tau_{\text{SF}} = 4.7 - 4.6 = 0.1$ GPa in tension and $\Delta\tau_{\text{SF}} = 8.4 - 8.5 = -0.1$ GPa in compression. However, the difference in the resolved normal stress between tension and compression is $\Delta\sigma_{\text{NF}} = 11.5$ GPa at dislocation nucleation ($\Delta\sigma_{\text{NF}} = 10.7$ GPa based on the geometry of the undeformed lattice), considerably more pronounced than the change in the resolved shear stress.

Finally, the values of SF and NF at dislocation nucleation that account for lattice rotation at that point differ somewhat from results that neglect the effects of lattice rotation. First, the data in Fig. 37 are merely shifted appropriately along the SF and NF axes. The trends remain the same. Also, the single crystal model for homogeneous dislocation nucleation can be modified to reflect the SF and NF values at dislocation nucleation. Least squares nonlinear regression to eq. (14) results in $\mu_{\text{s},1} = 0.426$ and $\mu_{\text{n},2} = 0.583$ with $\mu_{\text{n},1} = \mu_{\text{s},2} = 0$, which is mainly influenced by the decrease of NF under uniaxial tension. The fitting parameters for eq. (14) are in line with those based off of the initial SF and NF. While a fit to eq. (14) with the resolved stress parameters at dislocation nucleation may be more appropriate, this requires atomistic information to calculate the elastic deformation gradient, unlike the initial resolved stress parameters in Sections 5.1.1–5.1.3. In this respect, the resolved stress parameters SF and NF from the initial single crystal configuration give a relatively good approximation of the resolved stress components required for dislocation nucleation, noting that the largest change at the onset of plasticity is in the resolved stress normal to the slip plane on which the dislocation nucleates.

5.2. Model for dislocation nucleation from tilt grain boundaries

5.2.1. Symmetric tilt grain boundaries

Once the effect of lattice orientation has been isolated, the second step in the development of the interface strength model is to incorporate a first-order dependence on the inherent GB nanoporosity or free volume, D_c , via the simple relation

$$\sigma_{\text{max}}^{\text{int}} = (1 - \xi D_c) \sigma_{\text{max}}^{\text{sc}}. \quad (16)$$

Here, ξ is an amplification factor, the magnitude of which is dependent on the scale of the selected interface region which is used to compute the average free volume. This representation considers only the average porosity within a strip around the interface, without regard to its distribution along the interface plane. Here, D_c is the initial free volume [152] inherent to the interface structure. It is computed in the present case from atomistic simulations prior to imposition of tensile deformation (stress). The free volume measure is developed by examining the first-nearest neighbor coordination number of each atom, Z_1^i . Of course, atoms in a perfect bulk FCC crystalline arrangement have a first-order coordination number of 12. Atoms with Z_1^i less than that of the bulk crystal are defined as ‘damaged’ in this methodology. Previous molecular dynamics simulations on nanocrystalline samples [24] have shown that atoms at grain boundaries and triple junctions have

a range of coordination numbers, implying the presence of initial porosity within the interface structure. In this work, damaged atoms may be directly attributed to porosity at the interface between crystalline regions (aside from thermal vibrations which have been found to have a negligible affect on the D_c calculation at 300 K). Using this concept, we formulate a damage parameter on a per atom basis as

$$D^i = 1 - \left\langle \frac{Z_1^i - Z_{1,\text{th}}}{Z_{1,\text{ref}} - Z_{1,\text{th}}} \right\rangle. \quad (17)$$

In eq. (17), $Z_{1,\text{ref}}$ is the coordination number associated with a perfect crystalline lattice and $Z_{1,\text{th}}$ is the threshold coordination number required for an atom to be considered completely damaged ($D^i = 1$). This threshold value is taken as $Z_{1,\text{th}} = 8$ in this work; however, $Z_{1,\text{th}}$ may be adjusted to make the calculation of D^i sensitive to different types of interfacial damage. Eq. (17) allows the i th atom to have partial damage ($0 \leq D^i \leq 1$) depending on its local environment. Angle brackets define that atoms with $Z_1^i < Z_{1,\text{th}}$ have $D^i = 1$ and atoms with $Z_1^i > Z_{1,\text{ref}}$ have $D^i = 0$. The free volume measure is defined as the average of the point-wise damage parameter over the interface region,

$$D_c = \frac{1}{N'} \left[\sum_{i=1}^{N'} D^i \right] = \frac{1}{N'} \left[\sum_{i=1}^{N'} \left(1 - \left\langle \frac{Z_1^i - Z_{1,\text{th}}}{Z_{1,\text{ref}} - Z_{1,\text{th}}} \right\rangle \right) \right]. \quad (18)$$

Here, N' is the total number of atoms within the interface region. Numerically, eq. (18) may be evaluated at each time step from the atomic positions and requires no *a priori* knowledge of the interface structure or the form of the porosity evolution. In summary, the proposed model for tensile interface strength requires specification of the crystal lattice geometry, the associated non-Schmid parameters μ_s , μ_n and μ_p , the initial interface free volume, and an amplification factor, ξ . Further development of a relationship relating the crystal lattice geometry with free volume would allow the calculation of the tensile stress required for interfacial dislocation nucleation using only continuum quantities and the aforementioned non-Schmid parameters.

The interface strength model [eq. (16)] is then fit to the computed peak tensile stress values for interface models with $\langle 100 \rangle$ and $\langle 110 \rangle$ misorientation axes. The amplification factor ξ is regarded as an additional fitting parameter that is required in eq. (16) to predict the peak tensile interface stress values. The least-squares regression fit for the interface models with $\langle 100 \rangle$ and $\langle 110 \rangle$ misorientation axes uses the same non-Schmid parameters μ_s , μ_n and μ_p that were calculated using the single crystal data. Fig. 41 shows that the proposed relationship is capable of capturing the influence of interface structure on the maximum tensile stress for bicrystal interfaces with a $\langle 100 \rangle$ misorientation axis. For these boundaries, the role of the interface misorientation on dislocation nucleation is effectively captured through the averaged description of the interfacial porosity. Fig. 41 shows that the proposed relationship works well for boundaries with a $\langle 110 \rangle$ misorientation axis and $\theta < 109.5^\circ$. However, MD simulation results indicate that the proposed first-order model is not universally applicable, as this model is unable to capture the significant drop in the maximum tensile stress for symmetric boundaries which include the E structural unit ($\theta > 109.5^\circ$).

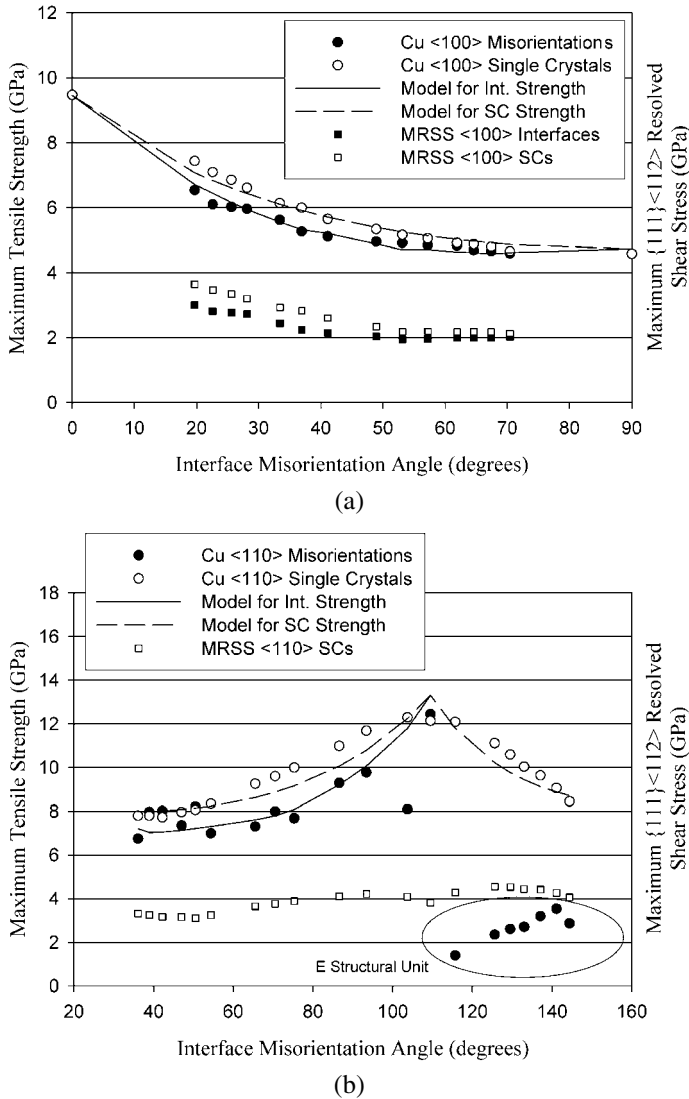


Fig. 41. Stress required for dislocation nucleation during uniaxial tensile deformation in single crystals and grain boundaries as a function of crystallographic orientation and misorientation, respectively. Single crystal data corresponds to (a) the [100]–[110] boundary ($\langle 100 \rangle$ STGBs) as well as (b) the [100]–[111] and [111]–[110] boundaries ($\langle 110 \rangle$ STGBs). Reprinted from [18] with permission; © 2007 Elsevier.

In order to address a greater range of interface misorientations for the $\langle 110 \rangle$ tilt axis, two solutions are currently being pursued to enhance the interface strength model. First, a higher-order formulation may be proposed, which includes a dependence on the *gradient* of free volume within the interface region. It is possible that localized ‘pockets’ of porosity, characteristic of interfaces with the E structural unit, result in high stress concen-

trations that contribute to the drop in tensile strength by promoting dislocation nucleation. Subsequent simulations of the spatial distribution of grain boundary free volume and its impact on dislocation nucleation for this range of boundaries are briefly discussed in Section 6.5. Additional details concerning the correlation between boundary structure and free volume can be found in Ref. [153]. Second, the amplification factor for the free volume measure may be posed as a function of the distribution of specific structural elements. This modification acknowledges that dissimilar interface features can contribute differently to the dislocation nucleation process. For example, Van Swygenhoven et al. have observed that stress concentrations at ledges and triple junctions in nanocrystalline samples can promote dislocation nucleation [35]. In our work, the natural alignment of certain structural units with respect to the primary slip systems appears to render certain interface features particularly susceptible to dislocation nucleation. For these boundaries, the tensile interface strength computed from MD simulations is probably closer to the Peierls–Nabarro stress (the applied stress required to overcome the lattice resistance to the movement of the interfacial dislocations).

5.2.2. Extensions to asymmetric tilt GBs

Several challenges arise in the formulation of an interface strength model for asymmetric tilt GBs. The ATGBs in this study contain an additional level of complexity relative to the STGBs in the aforementioned study; instead of two identical lattice orientations relative to the GB plane, the bicrystal lattice orientations relative to the ATGB mean boundary plane differ, resulting in different SF, NF, and PF values for each lattice. Also, while the free volume for ATGBs can be calculated, the faceting of ATGBs adds an additional layer of atomic level complexity because of its impact on dislocation nucleation. Finally, the preferential nucleation of dislocations from ATGBs dictates that the model parameters must have a physical basis. Obviously, using the Schmid and non-Schmid parameters of crystal 2 to predict the preferential nucleation of dislocations from the ATGB into crystal 1 is not physically appropriate. Therefore, as a first step towards an interface model for the stress required for dislocation nucleation at $\Sigma 3$ ATGBs, the present authors investigate the prediction of preferential nucleation in this class of asymmetric boundaries.

First, the Schmid and non-Schmid effects are investigated to examine their potential utility for understanding the preferential dislocation nucleation. As mentioned previously, the crystal lattices on each side of an ATGB are oriented differently relative to the applied stress direction, resulting in different Schmid and non-Schmid factors. Therefore, dislocation *motion* should be easiest in the lattice with the slip system associated with the highest Schmid factor, since this slip system has the highest resolved shear stress. However, dislocation *nucleation* from ATGBs does not necessarily occur on the highest Schmid factor slip system between the two crystals. Fig. 42(a) shows the maximum Schmid factor for both crystal lattices as a function of the inclination angle. The vertical lines at $\Phi = 35.26^\circ$ and $\Phi = 54.74^\circ$ correspond to relative minima in the maximum Schmid factor, which corresponds to a transition of active slip systems; the vertical line at $\Phi = 70.53^\circ$ delineates the region where ATGBs contain the 9R phase in Cu. However, contrary to what might be expected from Fig. 42(a) based on the Schmid factor, the partial dislocations are nucleated into crystal 1 for all $\Sigma 3$ ATGBs examined in Ref. [19]. This observation matches the crystal predicted from the maximum Schmid factors for low inclination angles only (i.e.,

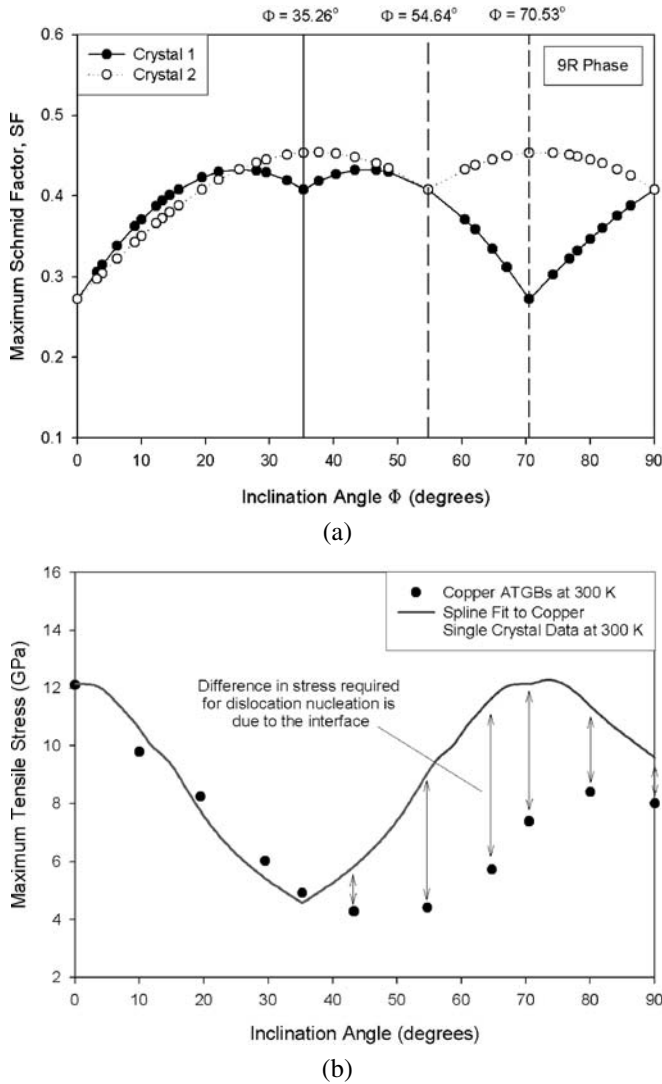


Fig. 42. (a) Change in the Schmid factor (SF) as a function of the grain boundary inclination angle for both Crystal 1 and Crystal 2. (b) Comparison between the stress required for dislocation nucleation in $\Sigma 3$ asymmetric tilt boundaries and single crystals for Cu at 300 K. Reprinted from [19] with permission; © 2007 Elsevier.

$\Phi < 25.24^\circ$). Similar trends are calculated for the normal and co-slip factors as well [19]; there are $\Sigma 3$ ATGB inclination angles for which NF and PF are greater in crystal 2 than crystal 1. Consequently, neither the Schmid or non-Schmid factors are useful as a criterion to predict the lattice in which the partial dislocation nucleates. However, the Schmid factor can be used to predict which slip system the dislocation nucleates on, once the crystal is known in which nucleation occurs.

Fig. 42(b) compares the stress required for dislocation nucleation in Cu $\Sigma 3$ ATGBs at 300 K with the stress required in Cu single crystals. The Cu single crystals are oriented the same as crystal 1. The single crystal stress values were calculated using the single crystal maximum tensile stress values required for dislocation nucleation at 300 K [18]. A cubic spline was used to interpolate stress values at intermediate misorientation angles. The single crystal stresses represent the *homogeneous* nucleation of dislocations in a defect-free lattice. Therefore, the stress required for *heterogeneous* dislocation nucleation from $\Sigma 3$ ATGBs should be less than or equal to the crystal with the lowest stress value. First, notice the good agreement between the single crystal and ATGB stress values for low inclination angles ($\Phi \leq 35.26^\circ$). Recall that the low inclination ATGB mechanism shows that the dislocation nucleates on a slip plane different from the plane of dissociation. Interestingly, this phenomenon requires stresses near the level required for homogeneous nucleation in crystal 1. Second, the stress required for nucleation in all other ATGBs ($\Phi \geq 43.31^\circ$) is much lower than the stress required for homogeneous nucleation. This difference has been captured in STGBs by considering GB characteristics, such as free volume [18].

The difference between stress values required for homogeneous (single crystal) and heterogeneous (bicrystal) dislocation nucleation may be due to a number of factors. Interface free volume and faceting were investigated in Ref. [19]. However, linear correlations to either the free volume or GB ledge density are not able to capture this difference. Dislocation nucleation in ATGBs may require more complicated nonlinear forms. In addition, the inclination of the facets with respect to the mean boundary plane may play a role in the decreased stresses required for heterogeneous nucleation of dislocations. As the inclination angle increases (decreases), a higher fraction of the uniaxial stress will resolve into a shear stress component on the CTB (SITB) facets. At $\Phi = 45^\circ$, the uniaxial tensile stress resolves equally normal to the facets (tensile) and perpendicular to the facets (shear). Furthermore, the CTB and SITB facets will likely behave differently with respect to the applied shear; e.g., the CTB deforms by twin migration under shear while many other boundaries deform via GB shuffling and partial dislocation nucleation [39]. Moreover, Sansoz and Molinari [38] show that the $\Sigma 9$ (221) STGB is about 4.5 times weaker in shear than in tension for Cu. Consequently, the inclination of the facets with respect to the mean boundary plane should result in an increased shear component, resulting in a lower tensile stress perpendicular to the mean boundary plane required for dislocation nucleation.

6. Insights and implications

The present work on structure and nucleation of dislocations at bicrystal boundaries illuminates certain issues pertaining to fundamental understanding of the role of grain boundaries. Here, we discuss some important aspects regarding dislocation nucleation in FCC metals under uniaxial loading applied perpendicular to the boundary plane: (i) grain boundary dislocation sources, (ii) representation of defects within grain boundaries as ordered structures comprised of disclination dipoles or disconnections, (iii) tension–compression asymmetry of trailing partial emission in Cu, (iv) the activation energy and volume for grain boundary dislocation nucleation, (v) the influence of grain boundary free volume on

dislocation nucleation, and (vi) continuum field theory. This understanding may benefit understanding of behavior of nanocrystalline and polycrystalline FCC metals.

6.1. Grain boundary dislocation sources

The dislocation nucleation event can be viewed as the activation of a dislocation source that lies within or nearby a boundary. The distinct structure of high-angle boundaries is best represented as a well-defined ordering of boundary dislocations. The nucleation and emission of dislocations from the boundary impacts the grain boundary dislocation content. This section briefly discusses several representative atomistic simulations to show how nucleated dislocations from activated sources interact with the high-angle grain boundary structure in the immediate vicinity.

The Burgers vector content of the grain boundary is often reduced following dislocation nucleation. For example, for $\Sigma 3$ asymmetric tilt grain boundaries of intermediate inclination angle, the grain boundary partial dislocation (D structural unit) is dissociated from the boundary on the maximum Schmid factor plane until it is emitted into the adjoining lattice. In this case, the Burgers vector content of the grain boundary is reduced by the emission of the partial dislocation, i.e., $b_{GB^*} = b_{GB} + b_{\text{dislocation}}$ where b_{GB^*} , b_{GB} , and $b_{\text{dislocation}}$ are the GB Burgers vector content before (asterisk) and after emission, and the Burgers vector of the emitted partial dislocation, respectively.

For certain boundaries in this work, the Burgers vector content of the grain boundary is not reduced following dislocation nucleation. For example, in the $\Sigma 3$ asymmetric tilt grain boundary of low inclination angle, the grain boundary dislocation is initially dissociated from the boundary on a slip plane of low resolved shear stress. However, the partial dislocation prefers nucleation on a slip plane of high resolved shear stress. Closer examination reveals that a partial dislocation loop nucleates on the maximum Schmid factor slip plane very near to the facet intersection (or GB ledge), as shown in Fig. 43. Because of the proximity to the boundary, the segment of the partial dislocation loop that glides toward the boundary is quickly absorbed, adding Burgers vector content to the boundary. The other half of the loop glides into the lattice, giving the appearance that this dislocation was emitted directly from the boundary. However, as Fig. 43 shows, the dislocation source visibly lies in the lattice near the intersection of the ATGB facets, and this ledge-like structure is the impetus for the dislocation nucleation event. This event can be thought of as the emission of a single dislocation loop within the lattice near the GB ledge. The size of simulation cell size limits our ability to discern whether these sources emit successive partial loop dislocations under further strain. Atomistic studies of this type offer details of the emission sequence that enhance our understanding of the source/sink nature of boundaries.

Dislocation sources can also lie directly in the interface. Recall the discussion of dislocation nucleation from $\langle 110 \rangle$ symmetric tilt grain boundaries with dissociated structure in Section 4.1.2. In this example, increasing tensile strain applied perpendicular to the boundary results in constriction of the dissociated partial dislocation after which partial dislocations are emitted in another nearby site, producing extrinsic stacking faults, and later intrinsic stacking faults, in both symmetric lattices. In this case, the dislocation source lies directly in the interface, leading to the nucleation of the partial dislocations within the grain

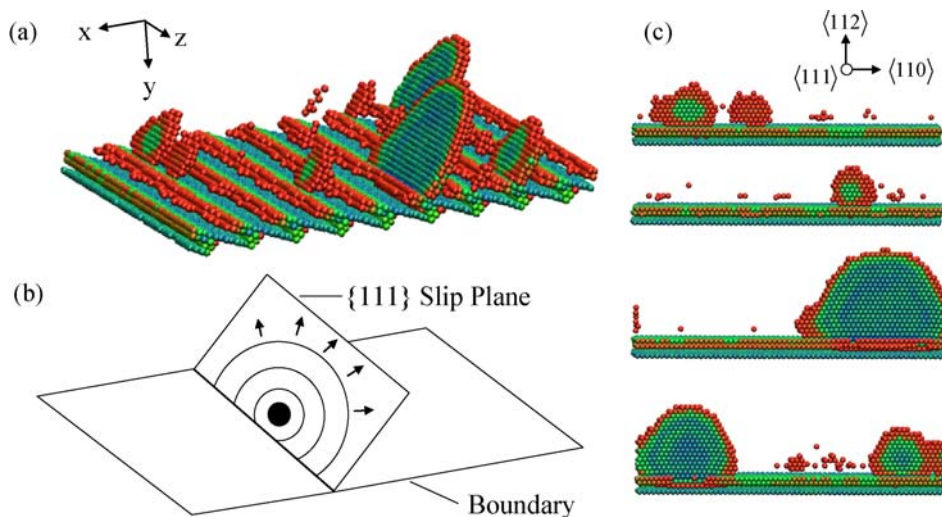


Fig. 43. Dislocation loops nucleate in the lattice near the facet intersections for the $\Sigma 3$ $(552)_1/(112)_2$ $\Phi = 19.47^\circ$ ATGB in Cu at 10 K. (a) Image of boundary at dislocation nucleation rendered via centrosymmetry. (b) Schematic showing the lattice dislocation source activated by deformation. (c) Slices of the $\{111\}$ slip plane showing various stages of dislocation loop nucleation.

boundary. Several partial dislocations were emitted from the grain boundary dislocation source and the boundary accommodates their emission through local structural rearrangement near the source. These kinds of complex sequence effects in dislocation nucleation become evident using atomistic simulations. A particularly fruitful area of endeavor is the characterization of Burgers vector content in various general boundaries following nucleation of dislocations, discerning how the residual content is manifested in terms of change of boundary structure. Moreover, the impact of this evolution on continued nucleation or absorption/desorption reactions is of great interest.

We must also emphasize that while the geometrically necessary dislocation density (associated net Burgers vector) contributes to lack of closure over a Burgers circuit in a crystal in the relaxed configuration, higher order gradients of the deformation gradient and gradients of lattice curvature also contribute to the lack of closure. This is discussed further in Section 6.4, and is especially important near grain boundaries that have undergone dislocation nucleation or other interactions with dislocations, as gradients of lattice curvature are pronounced in these regions. Hence, we regard that conservation of Burgers vector may be foundational in the more general setting of short range Burger circuit analyses that include a complete characterization of lattice curvature, including higher order gradients, but of course this is not usually done in constructing Burgers circuits near boundaries. Moreover, one can always assign dislocation content to the deformed grain boundary following dislocation nucleation to satisfy the balance relation, but whether or not this conforms to summation of specific configurations/reactions of a discrete set of feasible partial dislocations is another matter.

6.2. Disconnections and the description of GB defects

Recall from Section 1.2 that the undeformed structure of high-angle grain boundary interfaces may be described using disclination dipoles along with the structural unit model [62–68]. In this framework, the minority structural units are represented as wedge disclination dipoles while the strength of each wedge disclination is defined by the change in the angle between neighboring dissimilar structural units. To describe the irreversible distortion of the grain boundary structure after dislocation emission, Hurtado et al. [104] considered two theoretical models. The first model considered the creation of a disclination dipole (with opposite orientation to the dipoles within the interface) at the nucleation site. The length of the created dipole is assumed to be the same as that of the interface dipoles. The second model envisioned the creation of a dislocation at the nucleation site with the same Burgers vector and opposite orientation as the dislocation that is emitted into the lattice. Hirth and colleagues [69] provided a thorough description of grain boundary distortion caused by dislocation processes. For example, the transmission of dislocations through a tilt boundary results in the formation of a “disconnection” at the interface, which can be viewed as the superposition of a step of defined height and an edge dislocation. The emission of a dislocation from a tilt boundary results in the creation of an offset step which can be attributed the half-plane of the dislocation that has left the boundary. Depending on the local configuration in the neighborhood of the step, this offset can be described either as a grain boundary dislocation (GBD) or as a disconnection. We find this representation to be compelling; the offset associated with a disconnection is confirmed via the MD simulations presented in this work. For example, MD simulation of dislocation emission in Al resulted in a ledge at the intersection of the slip plane and the grain boundary (Fig. 20) while the emission of ISF facets in Cu introduces a small step in the interface plane (Fig. 23).

Fig. 44 shows a schematic comparing the disclination dipole model and the disconnection model based on analysis of the deformed $\Sigma 5$ (310) bicrystal interface structure. Recall that the original structure of the $\Sigma 5$ (310) interface (without ledges) involves a uniform distribution of C structural units, i.e., no disclination dipoles or disconnections are observed in the undeformed configuration, as shown in Fig. 44(a). The proposed disclination dipole representation of the distorted interface from [16] is shown in Fig. 44(b). The nucleation of a full dislocation from the interface is accompanied by a local lattice rotation, leading to the asymmetric expansion of two C structural units. This is represented as a series of staggered disclination dipoles that span the interface ledge at the nucleation site. It is noted that the deformed configurations in Fig. 44(b) are “idealized” to show that only two structural units are deformed by the slip process. In reality, a few structural units on either side of the dislocation nucleation point are slightly modified to smoothly accommodate the created ledge at the intersection of the slip plane and the interface. The strength of the each disclination within the dipole is equal to the difference between the angle of the C and the distorted C** structural units [recall structural unit definitions in Fig. 20(d)], which is calculated from MD as approximately 10° – 12° for this interface. The disclination dipole length is equal to that of two C** segments. If additional structural units existed between the C** units, such as B' units in higher-order CSL boundaries [16], then two dipoles may be required to represent the interface structure, each of which is oriented at an angle to the interface plane [67].

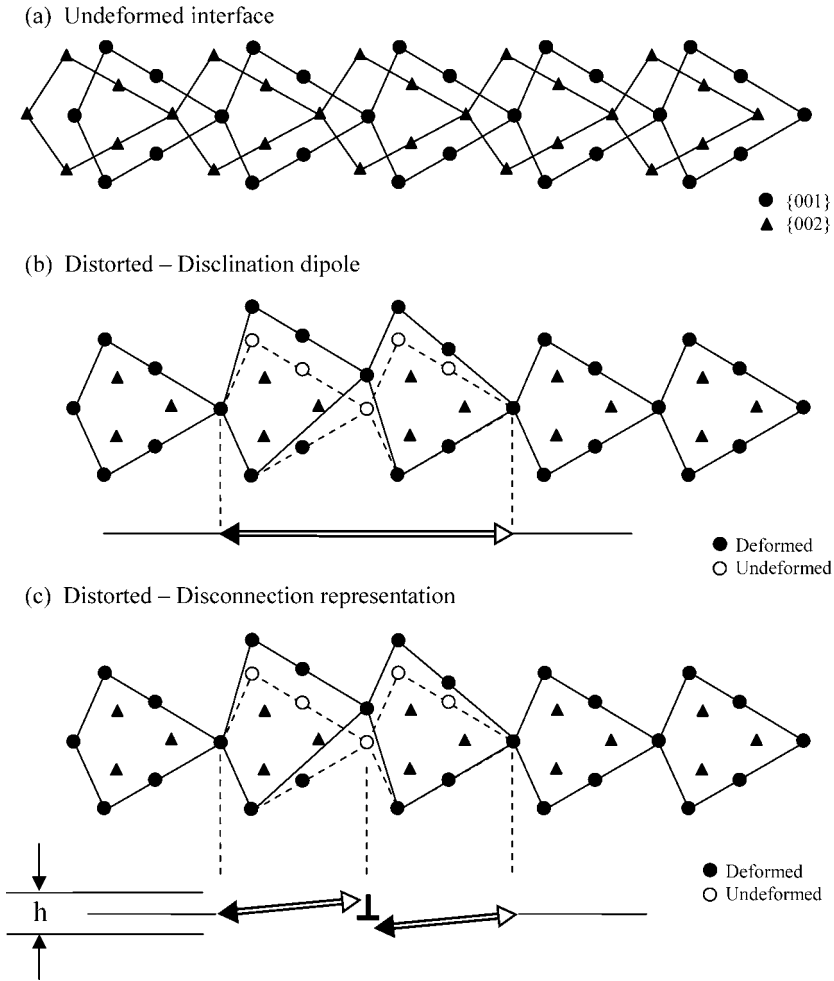


Fig. 44. Defect models for the distorted $\Sigma 5$ (310) interface after dislocation emission; (a) reference (undeformed configuration), (b) disclination dipole representation from [16] and (c) disconnection representation. Disclination dipoles are represented as a set of wedge disclinations using identical notation as Fig. 3.

It is clear from Figs 20(d) and 44(b) that the centerline of the C^{**} distorted structural units is not aligned along the interface (i.e., the lattice rotation during distortion is not symmetric about the misorientation axis). Thus, while the disclination dipole model captures the local change in lattice rotation at the defect site (the junction between C and C^{**} units) and the essential characteristics of the long-range field associated with the grain boundary distortion, it fails to truly capture the conformation of the step that is created at the dislocation nucleation site. Hirth et al. [69] proposed that this type of defect is more appropriately classified as a grain boundary dislocation or if localized lattice rotation is to be included, as a disconnection. The disconnection representation is shown in Fig. 44(c).

The disconnection description emphasizes the ledge within the grain boundary in addition to the local rotational deformation of the neighboring structural units at a distance away from the step and thus offers a more complete characterization of the defect. Finally, Hirth et al. [69] suggested two methods for which the disconnection can be removed. First, half of the semi-infinite array of dislocations at the interface can glide to restore the symmetric boundary, which will only likely happen for low-angle interfaces. Second, the disconnection itself can glide parallel to the interface plane to restore the low-energy boundary configuration. MD simulations in this work indicate a possible third mechanism for the removal of the disconnection at the interface. Upon application of a uniaxial stress normal to the boundary plane, which is perpendicular to the Burgers vector of the dislocation that represents the ledge in the interface, the disconnection is removed through a series of partial dislocation nucleation events on compatible slip systems in each crystal region. These dislocation nucleation events effectively unlock the disconnection at the interface resulting in a perfectly planar boundary, as shown in Figs 23 and 24 [17].

In our view, the distinction between structural units and disclination dipoles is somewhat of a matter of semantics, since the former clearly also possess the requisite geometric characteristics of a wedge type disclination dipole for low index tilt misorientation axes. However, the distinction may be viewed as useful on the basis that disclination dipoles are associated with lattice curvature gradients that either do not correspond to minimum energy repeating structural units in special (CSL) boundaries, or evolve in response to dislocation reactions with the boundary. As we have seen, in the process of dislocation emission, the responsible structural units can evolve into a pair of disclination dipoles with an interface dislocation representing a step in the disconnection convention. Moreover, disclination dipoles occur frequently in general boundaries and asymmetric tilt boundaries, which often have higher energy than the special boundaries that are characterized by dominance of repeating structural units.

6.3. Tension–compression asymmetry in trailing partial emission in Cu

The issue of partial dislocation versus full dislocation emission from grain boundaries has been the subject of recent interest in models for nanocrystalline materials. Recall that the mechanism of dislocation emission from the grain boundary occurs in several steps. First, a partial dislocation nucleates and is emitted from the grain boundary. Atomistic simulations have shown that stress-assisted free volume migration leads to the atomic shuffling necessary to form the Burgers vector required to nucleate a partial dislocation from the boundary region [29,31]. As the leading partial dislocation transects the grain, an intrinsic stacking fault is created behind the partial dislocation. For smaller grain sizes, the leading partial dislocation can be absorbed at the grain boundary on the opposite side of the grain prior to the emission of the trailing partial. For larger grain sizes, the trailing partial dislocation is nucleated from the boundary, restoring the order of the stacking sequence of {111} planes within the lattice and bounding the intrinsic stacking fault.

Developing models or relations with physically-based parameters that give insight to partial versus full dislocation nucleation has received much attention. For example, Yamakov and coworkers [154] proposed a deformation mechanism map that described

the transition from dislocation-mediated to grain boundary-mediated plastic deformation based on the equilibrium splitting distance for partials at $\sigma = 0$ and the grain boundary diameter, among other quantities. However, the description for the splitting distance is based solely on the intrinsic stacking fault energy, γ_{SF} , with no dependence on the unstable stacking fault energy, γ_{USF} . Simulations of nanocrystalline deformation do not support the cross-over of dislocation-based deformation mechanisms (slip of extended partial dislocations versus perfect slip of full dislocations) based only on the value of γ_{SF} . Van Swygenhoven et al. [32] noted that extended partial dislocations are observed above and below the predicted cross-over grain size in Cu [9–11]. In addition, NC deformation simulations [29,31] with a Ni potential (higher γ_{SF} than Al) only revealed extended partial dislocations for grain sizes as large as 20 nm. In contrast to the deformation mechanism map proposed by Yamakov and coworkers, Van Swygenhoven et al. [32] proposed that extended or full dislocation activity should be understood in terms of $\gamma_{\text{SF}}/\gamma_{\text{USF}}$ and, more importantly, that γ_{SF} alone cannot capture the important physics of the nucleation of leading and trailing partial dislocations from grain boundaries. Along those lines, Asaro and Suresh [155] present a mechanistic model for FCC nanocrystalline metals that employs the ratio $\gamma_{\text{SF}}/\gamma_{\text{USF}}$ to predict the emission of the trailing partial dislocation. *However, none of these arguments or models consider the effect of loading orientation (tension versus compression) or the resulting resolved normal stress on the emission of the trailing partial.*

Interestingly, MD simulations have shown a distinctly different behavior of the trailing partial dislocation between uniaxial tension and uniaxial compression for homogeneous and heterogeneous dislocation nucleation from single crystals and grain boundaries, respectively. For homogeneous dislocation nucleation in single crystal Cu, Fig. 45 shows that partial dislocation loops containing an intrinsic stacking fault are nucleated in tension and full dislocation loops are nucleated in compression for a single crystal with a [321] loading axis orientation. This phenomenon is commonly observed for multiple crystal orientations around the stereographic triangle.

For heterogeneous dislocation from grain boundaries, symmetric tilt grain boundaries with the E structural unit were deformed under uniaxial tension and compression. Fig. 45(c) shows the emission of partial dislocations from the $\Sigma 171$ (11, 11, 10) vicinal coherent twin boundary under uniaxial tension. Fig. 45(f) shows the emission of full dislocations from the same boundary under uniaxial compression. Interestingly, the full dislocation is emitted on the {100} slip plane, which has a higher resolved shear stress in the $\langle 110 \rangle$ slip direction than the {111} $\langle 110 \rangle$ slip systems. Despite the higher resolved shear stress, dislocation emission on the {100} slip plane is only observed in compression. As with single crystals, the partial (full) dislocation behavior in uniaxial tension (compression) is observed for a wide range of boundary structures across the misorientation range that corresponds to boundaries with the E structural unit. Other grain boundaries have not yet been deformed, but are expected to display similar behavior due to the high compressive resolved normal stress.

The contrast between the nucleation mechanisms under uniaxial tension and compression may shed light on our fundamental understanding of how resolved stresses affect dislocation nucleation in single crystals and grain boundaries. As discussed in Section 5 and depicted in Fig. 40, the main difference in how the applied stress is resolved for uniaxial tension and compression is the stress normal to the slip plane; in tension, this normal

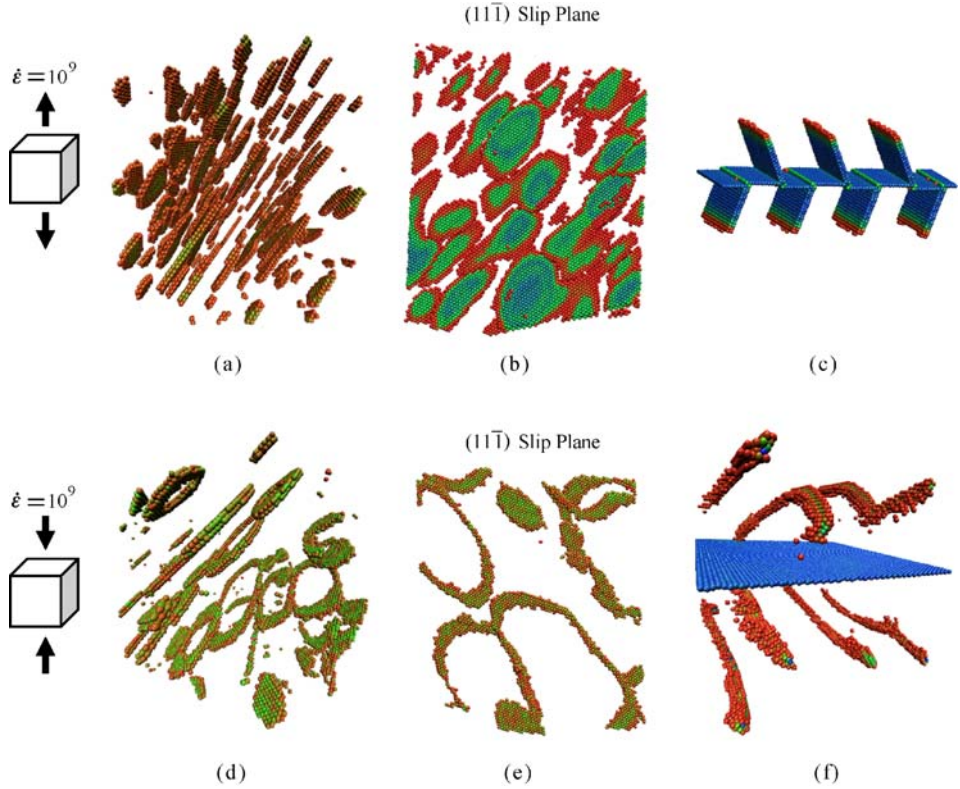


Fig. 45. Dislocation nucleation behavior in uniaxial tension (a–c) and uniaxial compression (d–f) for the (a, b, d, e) [321] single crystal and (c, f) $\Sigma 171$ (11, 11, 10) vicinal coherent twin boundary. The emission of the trailing partial dislocation is observed in compression, but not in tension. Images (b) and (e) are slices of the slip plane on which dislocations nucleate.

stress is tensile, and vice versa for compression. Full dislocation nucleation observed under uniaxial compression implies that a compressive stress normal on the active slip plane contributes to the nucleation of the trailing partial dislocation. In contrast, a tensile stress normal to the slip plane may deter the nucleation of a second partial dislocation. This may be explained with the generalized stacking fault (GSF) curve on the $\{111\}$ slip plane in the $\langle 112 \rangle$ direction for an FCC crystal. Zimmerman et al. [103] show that the GSF is affected by deformation of the material. They biaxially stretched the lattice by 4% while calculating the GSF curves and found that the unrelaxed γ_{USF} of 175 mJ/m² is reduced to 99 mJ/m² for the “deformed and relaxed” simulations. The unstable stacking fault energy (γ_{USF}) of the GSF curve is associated with the energy barrier for dislocation nucleation [101]. In this sense, the barrier to dislocation nucleation is reduced by the applied deformation. The GSF curve may be similarly affected by the magnitude and directionality of the resolved stress normal to the slip plane, particularly with respect to nucleation of the trailing partial dislocation. Indeed this feature of a changing potential energy landscape of grain boundaries under stress renders the prospect of characterizing the activation energies and

transition state pathways for various dislocation nucleation events quite challenging from a unit process standpoint.

6.4. Activation volumes and energies for grain boundary dislocation nucleation

The activation volume and the activation energy are important experimentally-measurable scalar quantities that can be used to model the rate and temperature sensitivity of plasticity mechanisms in constitutive relations [139,155,156]. The activation energy barrier for nucleation can be overcome with contributions from both mechanical work (applied stress) and thermal energy $k_B T$, where k_B is Boltzmann's constant and T is temperature. The activation volume is that required for the reaction to occur. Asaro and Suresh [155] have compiled a summary of available data on the effect of grain size on the activation volume in Cu and Ni. They show that the magnitudes of the activation volumes decrease substantially as the grain size decreases to the nanoscale, in line with other calculated and experimental observations [139,157–159]. For example, Schuh et al. [140] performed nanoindentation experiments on platinum at various temperatures and found activation volumes of $\sim 0.5 b^3$. Lu et al. [158] experimentally measured activation volumes of $\sim 10\text{--}20 b^3$ for nanotwinned copper. In addition to measurement of activation energies and activation volumes through experiments, Zhu and coworkers [156] have developed a computational methodology whereby atomistic simulations are used to calculate the activation energy and activation volume and assess the strain rate and temperature sensitivity of dislocation reactions. Here, we use MD calculations to obtain a first-order approximation of the activation energies and volumes for dislocation nucleation from $\Sigma 3$ asymmetric tilt grain boundaries in Cu and Al.

Calculations have shown that there is a significant drop in the stress required to nucleate dislocations from 10 to 300 K, suggesting that thermal activation plays a role in dislocation nucleation from the grain boundary. The activation volume Ω and activation energy Q for dislocation nucleation are calculated from a first-order model of stress-dependent activation energy whereby the activation energy linearly depends upon stress σ , i.e., $Q(\sigma) = Q^* - \sigma\Omega$. In this model, Q^* corresponds to the athermal nucleation energy barrier in the absence of applied stress. The activation energy Q measures the sensitivity of nucleation rate to temperature while the activation volume Ω measures the sensitivity of nucleation rate to stress. Zhu et al. [156] derived a form for the dislocation nucleation stress that takes into account both the temperature and strain-rate dependence. They applied this form to dislocation nucleation at surfaces under a constant strain rate. We employ the same equation to calculate the activation energy and activation volume in this study,

$$\sigma = \frac{Q^*}{\Omega} - \frac{k_B T}{\Omega} \ln \left(\frac{k_B T N \nu_0}{E \dot{\epsilon} \Omega} \right). \quad (19)$$

In eq. (19), the temperature $T = 300$ K, N is the number of nucleation sites ($N = 50,000$), ν_0 is the jump frequency ($\nu_0 = 3 \times 10^{11} \text{ s}^{-1}$), E is the elastic modulus, and $\dot{\epsilon}$ is the applied strain rate ($\dot{\epsilon} = 10^9 \text{ s}^{-1}$). The definitions of the terms are given by Zhu and coworkers [156]. The first term Q^*/Ω is the athermal stress required to nucleate a dislocation from the grain boundary. The pre-factor of the second term $k_B T/\Omega$ reduces the

nucleation stress by virtue of thermal fluctuation. In the logarithmic function, the numerator is the rate of energy exchange of the system with the thermal bath and the denominator is the rate of energy delivery into the system through mechanical work; the ratio between these terms determines the relative influence of thermal fluctuations in reducing the nucleation stress.

Several assumptions are made to calculate the activation volume and activation energy. First, the atomic jump frequency (ν_0) is chosen to represent the cooperative atomic motion necessary to form a dislocation, and is on the order of the frequency of free oscillation in Cu. Second, the number of nucleation sites (N) represents the approximate number of non-centrosymmetric atoms at the grain boundary. Since these are embedded in the logarithmic term, variation of $N\nu_0$ by several orders of magnitude results in very little change to the activation volume. Third, since the first term in eq. (19) corresponds to the athermal nucleation stress, the calculated nucleation stresses at 10 K were used as an approximate value. The nucleation stresses from all $\Sigma 3$ asymmetric tilt grain boundaries shown in Fig. 26(b) were used to capture the effect of variation in boundary structure and dislocation nucleation mechanisms on the activation energy and volume. Last, the elastic stiffness of the computational cell was calculated using the theoretical values of the two adjoining lattice regions; the effect of elastic anisotropy had little effect on the calculations. Using the nucleation stress values for uniaxial tension at $T = 300$ K, we find that the activation volumes for dislocation nucleation are on the order of $0.5\text{--}3 b^3$ in both Cu and Al, where $b = 0.255$ nm in Cu and $b = 0.286$ nm in Al. Rearranging the first term in eq. (19) such that $Q^* = \sigma\Omega$ gives the athermal activation energy barrier under zero applied stress, which ranges from 0.8–2.4 eV for $\Sigma 3$ asymmetric tilt grain boundaries. Also, using our first-order approximation of a linear dependence of activation energy on stress [$Q(\sigma) = Q^* - \sigma\Omega$] we calculate the activation energy for dislocation nucleation at 300 K as approximately 0.24–0.28 eV. Interestingly, the activation energies at 300 K are roughly the same for all $\Sigma 3$ boundaries examined, despite the wide range of boundary structures.

Zhu and coworkers [139,156] have calculated activation volumes and activation energies for heterogeneous dislocation nucleation and dislocation reactions using the climbing image nudged elastic band (CINEB) method. The CINEB method allows for a direct calculation of the activation energy versus stress relationship, without relying on several of the aforementioned assumptions made in the current calculations. Even so, the calculated activation energies are on the order of those computed for side surface nucleation ($Q = 0.64$ eV) and corner nucleation ($Q = 0.1$ eV) from nanopillars [156]. Furthermore, Zhu and coworkers [139] calculated activation energies for dislocation absorption ($Q_{\text{abs}} = 0.49$ eV) and dislocation direction transmission ($Q_{\text{trs}} = 0.67$ eV) at the coherent twin boundary that are similar to the present molecular dynamics calculations at a strain rate of 10^9 . The similarity of values suggests that the current calculations are a reasonable approximation of the activation volumes and activation energies for dislocation nucleation from $\Sigma 3$ asymmetric tilt grain boundaries.

The small activation volumes of $0.5\text{--}3 b^3$ promote enhanced temperature sensitivity of dislocation nucleation at grain boundaries and indicate that the atomic volume required for grain boundary dislocation nucleation is similar to the activation volume required for grain boundary shear events, $\Omega = 1 b^3$, in another FCC metal, Au [159]. The small activation volumes indicate that at the appropriate stress level, the motion of a few atoms may serve as

the impetus for nucleating a dislocation from the boundary. In addition, the small activation volume suggests that the nucleation event is appropriately viewed as a small dislocation loop nucleating at the grain boundary, as shown by our MD calculations in Section 4. As the length scales associated with activation volumes are on the order of interatomic spacing, we anticipate that the grain boundary free volume contributes to the driving force for the dislocation nucleation reaction.

6.5. Influence of grain boundary free volume on dislocation nucleation

The extent and distribution of grain boundary free volume may play a significant role in dislocation nucleation. For example, clusters of free volume on boundaries or at triple junctions are on the order of the activation volumes computed in the Section 6.4. In addition, the average free volume assists in correlation of the stress required for dislocation nucleation from $\langle 100 \rangle$ and $\langle 110 \rangle$ symmetric tilt grain boundaries, as discussed in Section 5.2. However, recall that the interface stress model in Section 5.2 was unable to capture the abrupt drop in the stresses required for dislocation nucleation in symmetric tilt grain boundaries with the E structural unit. This particular structural unit is associated with the $\Sigma 9$ (221) STGB and contains a large amount of free volume compared to other $\langle 110 \rangle$ symmetric tilt grain boundaries. Bicrystal simulations can provide insight into the relationship between grain boundary structure, grain boundary free volume, and dislocation nucleation from the boundary. Previous studies have shown that both the amount of free volume within the boundary and the spatial correlation of free volume within the boundary are important factors that play a role in dislocation nucleation [153].

A number of symmetric tilt grain boundaries within the misorientation range $109.5^\circ < \theta < 180^\circ$ were examined in terms of structure and free volume. The structures were generated using the methodology discussed in Section 2. The free volume was visualized and characterized with spatial correlation functions using a stereologically-based methodology, whereby a grid of points was superimposed in three dimensions over the atomic coordinates and each point was tested against a free volume criterion [153]. This methodology enabled Tschoopp et al. [153] to show that both the spacing and connectivity of the free volume in the tilt direction increase with increasing misorientation angle over the range $109.5^\circ < \theta < 180^\circ$. In fact, for low angle boundaries near the 180° perfect single crystal, the free volume is completely connected in the tilt direction.

The spatial distribution of free volume relates to dislocation nucleation because the free volume enables the cooperative atomic shuffling that triggers the emission of partial dislocations from the grain boundary. Not only is the spatial distribution important, but the spatial distribution of free volume *with respect to intersecting slip planes* may also affect dislocation nucleation. For dislocation nucleation to occur from the grain boundary, the cooperative motion of atoms on a $\{111\}$ slip plane intersecting the grain boundary is required. It is likely that this depends on the spacing and connectivity of free volume along that slip plane. For example, an isolated free volume pocket that intersects the slip plane will only allow local atomic shuffling in the few neighboring atoms. However, a large fraction of grain boundary free volume intersecting the slip plane affects a greater number of atoms along the slip plane, enabling the cooperative atomic shuffling required to nucleate

dislocations at the boundary. Moreover, for the E structural unit boundaries [153], the two active slip systems (maximum Schmid factor analysis) occur on the same {111} slip plane (coplanar slip), which intersects the boundary along the tilt direction. Thus, the spatial correlation statistics of free volume in the tilt direction are essential to the discussion of dislocation nucleation from boundaries with the E structural unit.

6.6. Continuum field theory

The foregoing implications have mainly focused on unit processes of dislocation nucleation over a wide range of grain boundary structures. We may also consider implications for framing higher scale models of inelasticity of polycrystals that might be pertinent to grain boundary engineering. Numerous studies have sought to increase the number density of certain special (CSL) boundaries by processing to assess whether fatigue and fracture resistance can be enhanced (cf. [13,14,47,48]). The assumption of superior characteristics of special boundaries has arguably outpaced fundamental understanding that can be gained by parametric study of mechanisms. Some work has been done using atomistic simulations to advance understanding. For example, Froseth et al. [160] used MD simulations to show that introducing clusters of grains with special boundaries in nanocrystalline materials results in a lower potential for strain accommodation relative to random orientation distributions. Combined with notions of percolation limits for special boundaries (cf. [161, 162]), parametric studies of symmetric and asymmetric special and general boundaries may provide a basis for a statistical approach to grain boundary engineering.

This work has also clarified directions for incorporating the structure of grain boundaries into a kinematical framework that extends the original concepts of Bilby and Smith [163] to incorporate lattice distortion in the grain boundary region that accommodates the net incompatibility over the crystal volume. Incorporation of disclinations and/or disconnections related to grain boundary structure into defect field theory can facilitate continuum crystal plasticity models that account for grain boundary structure. In classical crystal plasticity, grain boundaries are treated merely as compatible surfaces, with no manifestation of structure. In advanced continuum theories that invoke the notion of geometrically necessary dislocation density, the effect of grain boundaries is interpreted solely in terms of lattice curvature induced by first-order gradients of deformation, which does not capture the full nature of the kinematics near the boundary. The exchange and interaction of dislocations between the grain boundary and the grain interior requires treatment of grain boundary structure to discern the thermodynamic driving forces and kinetics properly [164].

The methodology we envision is founded upon two major assumptions, the first being a three-term multiplicative decomposition of the average deformation gradient for a volume element of crystalline material (cf. Clayton et al. [165,166]), i.e.,

$$\mathbf{F} = \underbrace{\mathbf{F}^e \mathbf{F}^i}_{\mathbf{F}^L} \mathbf{F}^p, \quad (20)$$

with the total lattice deformation written as \mathbf{F}^L . Here, \mathbf{F}^p accounts for the presence of line defects that leave the lattice unperturbed. The \mathbf{F}^i term accounts for incompatibility associated with defects that affect lattice arrangement as necessary to achieve compatibility

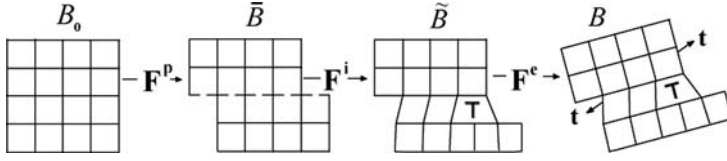


Fig. 46. Lattice model showing multiple configurations of a crystal volume element containing an edge dislocation.

with \mathbf{F}^p , the deformation gradient associated with dislocations. Fig. 46 shows how the lattice incompatibility associated with \mathbf{F}^p is accommodated by \mathbf{F}^i within the crystalline volume element, with the elastic deformation gradient \mathbf{F}^e representing both the recoverable lattice stretch associated with the average applied stress (long-range) acting on the element and rigid-body rotations of the lattice.

Compatibility is approached at the crystal level by considering covariant differentiation of the lattice directors in the current (deformed) configuration. At the microscopic level, spatial changes in the director vectors \mathbf{d}_a attached to the lattice are described by parallel transport of the directors with respect to a linear connection. The absolute change of the director vector field in the current configuration is found in terms of the covariant derivative $\hat{\nabla}$, i.e.

$$\hat{\nabla}_b \mathbf{d}_a = \mathbf{d}_{a,b} - \hat{\Gamma}_{ba}^{\cdot\cdot c} \mathbf{d}_c, \quad (21)$$

with the subscripted comma hereafter denoting partial coordinate differentiation with respect to current coordinates \mathbf{x} . The Christoffel symbols of the connection are defined as [167,168]

$$\hat{\Gamma}_{cb}^{\cdot\cdot a} \equiv F_{\cdot\alpha}^{La} F_{\cdot b, c}^{L-1\bar{\alpha}} + Q_{cb}^{\cdot\cdot a} = \bar{\Gamma}_{cb}^{\cdot\cdot a} + Q_{cb}^{\cdot\cdot a}, \quad (22)$$

where $\bar{\Gamma}_{cb}^{\cdot\cdot a} \equiv F_{\cdot\alpha}^{La} F_{\cdot b, c}^{L-1\bar{\alpha}} = -F_{\cdot\alpha, c}^{La} F_b^{L-1\bar{\alpha}}$ are coefficients of the crystal connection of non-Riemannian dislocation theories [169–173], and $Q_{cb}^{\cdot\cdot a}$ are micromorphic degrees-of-freedom representing contributions of spatial gradients of the lattice director field that are not incorporated in the term involving the first gradient of \mathbf{F}^L ; such gradients arise substantially from disclinations, for example. Upon assuming that $\hat{\nabla}_b \mathbf{d}_a = 0$ [168], the connection (eq. (22)) allows one to interpolate for the directions and magnitudes of the lattice directors between centroids of neighboring crystal volume elements. For example, in the trivial situation when $\hat{\Gamma}_{cb}^{\cdot\cdot a} = 0$, the lattice directors are spatially constant. The crystal connection ($\bar{\Gamma}$) component of eq. (22) accounts for effects of first-order spatial gradients of (the inverse of) \mathbf{F}^L , while the micromorphic variable \mathbf{Q} of eq. (22) accounts for additional spatial variation of lattice director vectors that is not captured by the first gradient of \mathbf{F}^L . The average continuum deformation of the director vectors located at the volume element's centroid is determined by \mathbf{F}^L , i.e., $\mathbf{d}_a = (F^{L-1})_{\cdot a}^{\alpha} \mathbf{g}_{\alpha}$, where \mathbf{g}_{α} are basis vectors in the current configuration. The director vector motion mapped from the intermediate configuration to the current configuration is given by $\chi = \mathbf{F}^e \mathbf{F}^i \tilde{\mathbf{l}} = \mathbf{F}^L \tilde{\mathbf{l}} \Rightarrow \mathbf{d}_a = \chi \mathbf{D}_a$, with $\chi^T \chi \neq \mathbf{1}$; here, the director triad on the reference configuration is an anholonomic basis $\mathbf{D}_a = D_a^{\beta} \mathbf{G}_{\beta}$, with holonomic basis vectors, \mathbf{G}_A , on the reference configuration. The dual lattice vectors \mathbf{D}^a , \mathbf{d}^a are defined by the relations $\mathbf{D}^a \cdot \mathbf{D}_b = \mathbf{d}^a \cdot \mathbf{d}_b = \delta_b^a$.

The components of the Riemann–Christoffel curvature tensor $\hat{R}_{bcd}^{\dots a}$ formed from the connection coefficients $\hat{\Gamma}_{cb}^{\dots a}$ are found using

$$\hat{R}_{bcd}^{\dots a} \equiv \hat{\Gamma}_{db,c}^{\dots a} - \hat{\Gamma}_{cb,d}^{\dots a} + \hat{\Gamma}_{ce}^{\dots a} \hat{\Gamma}_{db}^{\dots e} - \hat{\Gamma}_{de}^{\dots a} \hat{\Gamma}_{cb}^{\dots e}, \quad (23)$$

which, because $\hat{\Gamma}_{cb}^{\dots a} = \bar{\Gamma}_{cb}^{\dots a} + Q_{cb}^{\dots a}$, we are able to rewrite as [174]

$$\hat{R}_{bcd}^{\dots a} = \underbrace{\bar{R}_{bcd}^{\dots a}}_{=0} + 2\hat{\nabla}_{[c} Q_{d]b}^{\dots a} + Q_{ce}^{\dots a} Q_{db}^{\dots e} - Q_{de}^{\dots a} Q_{cb}^{\dots e} + \hat{T}_{cd}^{\dots e} Q_{eb}^{\dots a}, \quad (24)$$

where the curvature from the crystal connection, $\bar{R}_{bcd}^{\dots a}$, vanishes identically as shown, since $\bar{\Gamma}$ is integrable. We can then express the fully covariant rendition of the curvature tensor $\hat{R}_{abcd} \equiv C_{af}^L \hat{R}_{bcd}^{\dots f}$ as [167]

$$\hat{R}_{[ab]cd} = 2\hat{\nabla}_{[c} Q_{d][ba]} + \hat{T}_{cd}^{\dots e} Q_{e[ba]}, \quad \hat{R}_{(ab)cd} = 2\hat{\nabla}_{[c} Q_{d](ab)} + \hat{T}_{cd}^{\dots e} Q_{e(ab)}. \quad (25)$$

We see from eq. (25) that $\hat{\mathbf{R}}$ vanishes completely when $\mathbf{Q} = \mathbf{0}$. The connection coefficients $\hat{\Gamma}_{cb}^{\dots a}$ are given by eq. (22), with the covariant components of \mathbf{Q} assigned the following anti-symmetry property [167,168]:

$$Q_{cba} \equiv Q_{cb}^{\dots d} C_{da}^L = -Q_{cab} = Q_{c[ba]}. \quad (26)$$

The microrotation kinematic variable \mathbf{Q} describes spatial gradients of lattice rotation within the crystalline volume element arising from higher order gradients of net dislocation density and distributed partial disclinations. This includes the effect of partial disclination dipoles and additional boundary dislocations introduced in the disconnection characterization of Hirth et al. [69]. In the current configuration, consider a Burgers circuit c enclosing area a comprised of oriented differential elements $\mathbf{n} da$. A total Burgers vector accounting for incompatibility induced by the torsion and curvature tensors may be written as [167, 175,176],

$$B^a \equiv \frac{1}{2} \varepsilon^{dbc} \int_a (\hat{T}_{bc}^{\dots a} - \hat{R}_{ecb}^{\dots a} x^e) n_d da = B_T^a + B_R^a, \quad (27)$$

where $2B_T^a \equiv \varepsilon^{dbc} \int_a \hat{T}_{bc}^{\dots a} n_d da$ describes the closure failure of c and $2B_R^a \equiv \varepsilon^{dbc} \int_a \hat{R}_{ecb}^{\dots a} x^e n_d da$ measures the change in direction of position vector x^e upon parallel transport about c with respect to the connection $\hat{\Gamma}$. Eq. (27) reduces to the usual form based on net dislocation density (B_T^a only) when disclinations are absent and higher-order spatial gradients of lattice director vectors are neglected (i.e., when $\hat{T}_{bc}^{\dots a} = \bar{T}_{bc}^{\dots a}$, $Q_{bc}^{\dots a} = 0$, and $\hat{R}_{bcc}^{\dots a} = 0$).

To this point we have not associated the second term involving $Q_{cb}^{\dots a}$ in eq. (22) solely with disclinations. We may further specialize and simplify the theory by making this assertion and neglecting higher-order contributions of gradients of \mathbf{F}^L as an approximation, as done by Clayton et al. [165]. We can then re-write eq. (27) in terms of the second rank geometrically necessary dislocation tensor $\boldsymbol{\alpha}$ (Nye tensor) and second rank geometrically

necessary disclination tensor θ , each referred to the spatial configuration, i.e.,

$$B^a = \int_a (\alpha^{ad} + C^{L-1af} \varepsilon_{f gb} \theta^{gd} x^b) n_d da, \quad (28)$$

where

$$2\alpha^{ad} \equiv \varepsilon^{dbc} \hat{T}_{bc}^{..a}, \quad 4\theta^{gd} \equiv \varepsilon^{gba} \varepsilon^{dce} \hat{R}_{abce}. \quad (29)$$

Defect density tensors α and θ contain information enabling us to fully reconstruct $\hat{\mathbf{T}}$ and $\hat{\mathbf{R}}$, respectively, because of the skew-symmetric properties of these quantities:

$$\hat{T}_{cb}^{..a} = \hat{T}_{[cb]}^{..a} = \varepsilon_{cbd} \alpha^{ad}, \quad \hat{R}_{abcd} = \hat{R}_{[ab][cd]} = \varepsilon_{bae} \varepsilon_{cdf} \theta^{ef}. \quad (30)$$

The geometrically necessary defect density tensors of eq. (29) are related to the summed contributions of discrete crystal defects over a given crystal volume as

$$\alpha = \sum_j \rho^j \mathbf{b}^j \otimes \boldsymbol{\xi}^j, \quad \theta = \sum_k \eta^k \boldsymbol{\omega}^k \otimes \boldsymbol{\zeta}^k, \quad (31)$$

with ρ^j , \mathbf{b}^j , and $\boldsymbol{\xi}^j$ the *net* scalar dislocation line density, Burgers vector, and unit tangent line, respectively, for dislocation population j , and with η^k , $\boldsymbol{\omega}^k$, and $\boldsymbol{\zeta}^k$ the net scalar disclination line density, Frank vector, and unit tangent line, respectively, for disclination population k . All quantities in eq. (31) refer to the current (spatial) configuration B . Notice that α and θ do not account for curved defect segments and combinations of defect lines that do not contribute to a net Burgers vector (e.g., dislocation loops enclosed by a Burgers circuit). We use the qualifiers “net,” “geometrically necessary,” and “non-redundant” interchangeably to describe defect densities that contribute to incompatibility.

It is perhaps instructive to consider linearized compatibility equations for the net defect density tensors of eq. (31) that follow from identities of Bianchi and Schouten (cf. [174]), expressed in Cartesian coordinates as

$$\hat{T}_{[bc,d]}^{..a} = \hat{R}_{[bcd]}^{..a} \rightarrow (C^L \alpha)_{a,b}^b = \varepsilon_{abc} \theta^{bc}, \quad \hat{R}_{b[cd,e]}^{..a} = 0 \rightarrow \theta_{,b}^{ab} = 0. \quad (32)$$

In a small-strain formulation that employs additive elastoplastic strains and rotation gradients, De Wit [177] inferred from equations analogous to eq. (32) that disclinations may act as sources/sinks for dislocations, and that disclination lines cannot end abruptly within a crystal. Also, when disclinations are absent, the first of eq. (32) depicts a divergence-free dislocation density tensor, meaning that dislocations cannot start or end within the crystal. This linearization, while physically illustrative, is not essential in our general finite strain and rotation framework, nor do its implications necessarily carry over.

The second major assumption in our kinematic framework is an additive decomposition of a linear connection describing spatial gradients of the slip directions and lattice director vectors between neighboring crystalline elements (i.e., the microscopic description). Christoffel symbols of this connection, introduced formally in eq. (22), may be written as

$$\hat{\Gamma}_{cb}^{..a} = \underbrace{F_{,\bar{a}}^{La} F_{,b,c}^{L-1\bar{a}}}_{\text{crystal connection (GNDs)}} + \underbrace{C^{L-1ad} Q_{c[bd]}}_{\text{microrotation (disclinations)}}, \quad (33)$$

where the first term on the right side describes gradients of the director vectors due to first-order gradients in the average lattice deformation tensor \mathbf{F}^L , following Bilby et al. [169]. The micromorphic variable \mathbf{Q} (cf. [167,177]) appears in the second term on the right of eq. (33) and, neglecting contribution of higher order gradients of \mathbf{F}^L (to \mathbf{Q}), represents microrotation associated with disclinations.

The reader is referred to Clayton et al. [165] for a more complete discussion of the implications of foregoing discussion of net dislocation and disclination defect densities over a given scale of Burgers circuit in terms of the differential geometric interpretation. Moreover, Clayton et al. [165] discuss general Somigliana dislocations [70] that can be used to characterize the displacement discontinuities attributed to most defects, including translational (dislocations), rotational (disclinations) of Volterra [61], point defects [178, 179], and interface incompatibility in multi-phase composites [180] with additional terms in eq. (33).

At issue here is how to incorporate grain boundary structure into the preceding kinematic formalism for Burgers circuits that cross boundaries. The appropriate description depends on the scale of the crystal volume concerned. For Burgers circuits with size much greater than the periodic length of favored boundary structural units and disclination dipoles that comprise general boundaries, the partial dislocation content of the boundary can be lumped into a contribution to microrotation analogous to the second term in eq. (33), as is common practice in the macroscopic theory of grain boundaries based only on the dislocation description. However, at fine scales this decomposition of the crystal connection in eq. (22) becomes important since dislocations that contribute to the net dislocation density tensor of Nye [181] are associated with \mathbf{F}^p , and the crystal connection expresses the jump of orientation of the lattice across the boundary, \mathbf{F}^L , should incorporate the incompatible distortion of the lattice due both to the partial dislocation content (or net Frank vector) of favored boundary structural units in eq. (31.1) as well as disclination dipoles in eq. (31.2). This may be accomplished by assigning the former to $\mathbf{F}^p(\alpha)$ which depends on net dislocation density, and the latter to a component of $\tilde{\mathbf{F}}^i(\theta)$ which incorporates the net disclination content, with an additional component $\tilde{\tilde{\mathbf{F}}}^i$ that can be assessed to ensure local compatibility of the relation $\mathbf{F}^i \mathbf{F}^p$, assuming compatible \mathbf{F}^e associated with the long-range elastic deformation field, i.e.,

$$\mathbf{F} = \underbrace{\mathbf{F}^e \tilde{\tilde{\mathbf{F}}}^i \tilde{\mathbf{F}}^i(\theta)}_{\mathbf{F}^L} \mathbf{F}^p(\alpha). \quad (34)$$

This additional component $\tilde{\tilde{\mathbf{F}}}^i$ of course reflects the contributions of the higher order spatial gradients of lattice curvature alluded to previously. Of course, the components of this decomposition evolve during dislocation nucleation, absorption, or desorption (kinetics). The problem of elucidating the $\tilde{\tilde{\mathbf{F}}}^i \tilde{\mathbf{F}}^i(\theta) \mathbf{F}^p(\alpha)$ decomposition belongs to nanomechanics (e.g., atomistic modeling) owing to the nonlinear finite elasticity of the dislocation/disclination core regions. Both the boundary energy as well as the kinetics of dislocations can be explored. It is a fruitful area of future research.

7. Concluding remarks

This work has demonstrated how atomistic simulations can advance fundamental understanding of the structure and inelastic behavior (nucleation of dislocations) of symmetric and asymmetric tilt grain boundaries in fcc metals. Major findings include:

- The calculated interface energies for $\Sigma 3$ asymmetric tilt grain boundaries agree with experimentally measured grain boundary energies and are predicted based on an ideal faceting into the $\Sigma 3$ (111) and $\Sigma 3$ (112) symmetric tilt grain boundaries [79]. The minimum energy structures for Cu correspond well with HRTEM images of the 9R phase in other low stacking fault energy FCC metals. Also, the asymmetric tilt grain boundary structures ideally facet into the structural units of the two $\Sigma 3$ symmetric tilt boundaries with a well-defined ordering of structural units and their faceting [79,130]. A thorough appreciation for the structure of asymmetric tilt grain boundaries can improve understanding of the relationship between dislocation nucleation strength and grain boundary structure.
- Aside from the symmetric tilt $\Sigma 3$ (111) boundary, no increase in tensile strength is observed at boundaries with low-order CSL character. Increased tensile strength at the coherent $\Sigma 3$ (111) boundary can be attributed to the homogeneous nucleation of dislocations within each lattice, rather than heterogeneous nucleation from the grain boundary. For all other models, failure in uniaxial tension occurs by way of dislocation nucleation from the bicrystal interface. The dislocation nucleation event may be accompanied by structural rearrangement prior to emission (such as the evolution of short stacking fault facets) that locally improves the coherency of the interface.
- MD simulations indicate that the orientation of the opposing lattice regions relative to the applied stress and the presence of certain structural units are two significant features of the interface geometry/structure that affect the tensile interface strength. Specifically, boundaries that contain the E structural unit nucleate dislocations at low applied tensile stresses. Based on the MD simulation results, a first-order model for tensile interface strength is developed which is capable of capturing the dependence of interface misorientation for many tilt boundaries [18]. Non-Schmid effects are critical when formulating a model for homogeneous [73] and heterogeneous dislocation nucleation. Specifically, the stress normal to the slip plane is found to play a significant role in dislocation nucleation for boundaries with the $\langle 100 \rangle$ misorientation axis. Furthermore, accounting for interfacial free volume through an average measure based on coordination number [152] is sufficient to model the tensile strength of boundaries with the $\langle 100 \rangle$ tilt axis and many boundaries with the $\langle 110 \rangle$ tilt axis. However, for $\langle 110 \rangle$ boundaries that contain the E structural unit, it is likely that a higher-order model must be invoked that include the effect of gradients of free volume or more detailed information concerning the relationship between structural unit configuration and slip system orientation. For example, the spacing and connectivity of free volume pockets within the boundary and their distribution along a $\{111\}$ slip plane with a high resolved shear stress in the slip direction may impact the relative ease of the thermally activated dislocation nucleation event [153].
- The wide range of symmetric and asymmetric tilt grain boundaries investigated here provides insight into dislocation nucleation mechanisms and how they might impact inelastic deformation processes in higher scale nanocrystalline models. Of course, there

is the caveat that the energy minimized structures of this study are applicable to (near) equilibrium structures as might be obtained via electrodeposition, rather than via extensive deformation processing. Symmetric tilt grain boundaries in Al show that a ledge forms after emission of a full dislocation from a planar (100) boundary [16]. Symmetric tilt grain boundaries with dissociated structure show that the spacing between dissociated partial dislocations plays an important role in dislocation nucleation [17]. The dislocation nucleation mechanisms of $\Sigma 3$ asymmetric tilt grain boundaries are greatly affected by the faceted and dissociated boundary structure [19], despite having the same misorientation angle and low-order CSL content. The dislocation organization and character may also impact dislocation nucleation. Grain boundary dislocation sources behave differently; the nucleated dislocations in some high-angle boundaries merely result in a decrease of the Burgers vector content of the boundary equal to the Burgers vector of the emitted dislocations. However, as shown for a $\Sigma 3$ asymmetric tilt grain boundary, stress concentrations near the facet intersections for some boundaries may help activate lattice dislocation sources that nucleate dislocation loops near the boundary. The absorption of part of the dislocation loop into the boundary yields an increase in the Burgers vector content of the boundary. Additionally, dislocation sources can lie within the interface as shown for the dissociated symmetric tilt grain boundaries.

- Differences in the resolved normal stress to the plane of dislocation nucleation between uniaxial tension and compression leads to a tension–compression asymmetry of dislocation nucleation [141]. For single crystals, the stress required to homogeneously nucleate dislocations has a strong dependence on loading orientation in both uniaxial tension and compression. Some orientations require a higher stress in compression than in tension (e.g., [110] and [111]), while other orientations require a higher stress in tension ([100]). In addition to the normal stress affecting the magnitude of the stresses involved in dislocation nucleation, it also affects the emission of the trailing partial dislocation. In uniaxial tension for Cu single crystals and grain boundaries, no trailing partial dislocation is observed, as expected. However, in compression, the trailing partial dislocation is observed in both Cu single crystals and grain boundaries, despite the low stacking fault energy γ_{SF} and ratio γ_{SF}/γ_{USF} . This indicates that the resolved normal stress plays an important role in the emission of the trailing partial dislocation.
- The activation energies and activation volumes for dislocation nucleation from $\Sigma 3$ asymmetric tilt grain boundaries were calculated from a first-order model of stress-dependent activation energy. The athermal activation energies are on the order of 0.8–2.4 eV, the activation energies at 300 K are approximately 0.24–0.28 eV, and the activation volumes are on the order of $0.5\text{--}3\ b^3$ in both Cu and Al. The small activation volumes suggest that the nucleation of dislocations from the boundaries is associated with the cooperative motion of a small group of atoms within the boundary.
- The initial and distorted (post dislocation nucleation) structures of grain boundaries are discussed in terms of partial dislocations, disclination dipoles and disconnections. Symmetric tilt boundaries which obey the structural unit model can be represented as a series of repeating structural units associated with favored boundaries connected by disclination dipoles. Disconnections may also be incorporated into the description of the interface geometry if steps or ledges exist within the interface plane. More importantly, MD simulations in this work provide direct observation of the offset step that appears at the

interface after nucleation of full dislocations in Al [16]. The geometry of the offset step may be described using disconnections, or equivalently as a series of disclination dipoles and grain boundary dislocations, in agreement with Hirth et al. [69]. Furthermore, this work identifies additional mechanisms by which a disconnection at the interface may be removed [17].

- The relation of the grain boundary structure to continuum field theory representations of dislocations and disclinations has been discussed in terms of a generalization of the decomposition of the deformation gradient that addresses both geometrically necessary dislocations and microrotations captured by disclinations originally proposed by Clayton et al. [165], and some preliminary ideas have been advanced for addressing grain boundary structure through nanomechanical boundary value problems of the Bilby-Smith type [163].

Acknowledgements

The authors would like to thank Professor J.P. Hirth for the invitation to contribute to the Dislocations in Solids series. This work was supported in part by a National Science Foundation Graduate Research Fellowship (M.A.T.), by the NASA Langley Research Center under grant NAG-1-02054 (D.E.S.) and by the National Center for Supercomputing Applications under contract DMR060019N (utilizing Cobalt). D.L.M. is grateful for the additional support of this work by the Carter N. Paden Jr., Distinguished Chair in Metals Processing.

References

- [1] G.B. Olson, *Science* 288 (2000) 993.
- [2] C.S. Smith, *A Search for Structure: Selected Essays on Science, Art and History*, MIT Press, Cambridge, MA, 1981.
- [3] A.S. Khan, S. Huang, *Continuum Theory of Plasticity*, John Wiley & Sons, New York, 1995.
- [4] E.O. Hall, *Proc. R. Soc. London B* 64 (1951) 747.
- [5] N.J. Petch, *J. Iron Steel Ind.* 174 (1953) 25.
- [6] Y.M. Wang, A.V. Hamza, E. Ma, *Appl. Phys. Lett.* 86 (2005) 241917.
- [7] Y.M. Wang, A.V. Hamza, E. Ma, *Acta Mater.* 54 (2006) 2715.
- [8] Y. Zhou, U. Erb, K.T. Aust, G. Palumbo, *Scripta Mater.* 48 (2003) 825.
- [9] J. Schiotz, F.D. Di Tolla, K.W. Jacobsen, *Nature* 391 (1998) 561.
- [10] J. Schiotz, T. Vegge, F.D. Di Tolla, K.W. Jacobsen, *Phys. Rev. B* 60 (1999) 11971.
- [11] J. Schiotz, K.W. Jacobsen, *Science* 301 (2003) 1357.
- [12] J. Schiotz, *Scripta Mater.* 51 (2004) 837.
- [13] V. Randle, *The Role of the Coincidence Site Lattice in Grain Boundary Engineering*, Institute of Materials, Maney Publishing, London, 1997.
- [14] C.A. Schuh, M. Kumar, W.E. King, *Acta Mater.* 51 (2003) 687.
- [15] J.P. Hirth, J. Lothe, *Theory of Dislocations*, John Wiley & Sons, New York, 1982.
- [16] D.E. Spearot, K.I. Jacob, D.L. McDowell, *Acta Mater.* 53 (2005) 3579.
- [17] D.E. Spearot, K.I. Jacob, D.L. McDowell, *Int. J. Plast.* 23 (2007) 143.
- [18] D.E. Spearot, M.A. Tschopp, K.I. Jacob, D.L. McDowell, *Acta Mater.* 55 (2007) 705.
- [19] M.A. Tschopp, D.L. McDowell, *Int. J. Plast.* 24 (2008) 191.

- [20] V. Yamakov, D. Wolf, M. Salazar, S.R. Phillpot, H. Gleiter, *Acta Mater.* 49 (2001) 2713.
- [21] V. Yamakov, D. Wolf, S.R. Phillpot, H. Gleiter, *Acta Mater.* 50 (2002) 5005.
- [22] V. Yamakov, D. Wolf, S.R. Phillpot, A.K. Mukherjee, H. Gleiter, *Nat. Mater.* 1 (2002) 45.
- [23] V. Yamakov, D. Wolf, S.R. Phillpot, H. Gleiter, *Acta Mater.* 51 (2003) 4135.
- [24] H. Van Swygenhoven, M. Spaczer, A. Caro, *Acta Mater.* 47 (1999) 3117.
- [25] H. Van Swygenhoven, M. Spaczer, A. Caro, D. Farkas, *Phys. Rev. B* 60 (1999) 22.
- [26] H. Van Swygenhoven, P.A. Derlet, *Phys. Rev. B* 64 (2001).
- [27] H. Van Swygenhoven, A. Caro, D. Farkas, *Mater. Sci. Eng. A* 309–310 (2001) 440.
- [28] H. Van Swygenhoven, *Science* 296 (2002) 66.
- [29] H. Van Swygenhoven, P.M. Derlet, A. Hasnaoui, *Phys. Rev. B* 66 (2002).
- [30] P.M. Derlet, H. Van Swygenhoven, *Scripta Mater.* 47 (2002) 719.
- [31] P.M. Derlet, H. Van Swygenhoven, A. Hasnaoui, *Philos. Mag.* 83 (2003) 3569.
- [32] H. Van Swygenhoven, P.M. Derlet, A.G. Froseth, *Nat. Mater.* 3 (2004) 399.
- [33] A. Froseth, H. Van Swygenhoven, P.M. Derlet, *Acta Mater.* 52 (2004) 2259.
- [34] A.G. Froseth, P.M. Derlet, H. Van Swygenhoven, *Acta Mater.* 52 (2004) 5863.
- [35] H. Van Swygenhoven, P.M. Derlet, A.G. Froseth, *Acta Mater.* 54 (2006) 1975.
- [36] H. Van Swygenhoven, J.R. Weertman, *Mater. Today* 9 (2006) 24.
- [37] T. Shimokawa, A. Nakatani, H. Kitagawa, *Phys. Rev. B* 71 (2005).
- [38] F. Sansoz, J.F. Molinari, *Scripta Mater.* 50 (2004) 1283.
- [39] F. Sansoz, J.F. Molinari, *Acta Mater.* 53 (2005) 1931.
- [40] D.H. Warner, F. Sansoz, J.F. Molinari, *Int. J. Plast.* 22 (2006) 754.
- [41] J.W. Cahn, Y. Mishin, A. Suzuki, *Acta Mater.* 54 (2006) 4953.
- [42] H. Zhang, M.I. Mendelev, D.J. Srolovitz, *Scripta Mater.* 52 (2005) 1193.
- [43] N. Chandra, *Mater. Sci. Forum* 304–306 (1999) 411.
- [44] N. Chandra, P. Dang, *J. Mater. Sci.* 34 (1999) 655.
- [45] S. Namilaie, N. Chandra, T.G. Nieh, *Scripta Mater.* 46 (2002) 49.
- [46] V. Yamakov, D. Wolf, S.R. Phillpot, H. Gleiter, *Acta Mater.* 50 (2002) 61.
- [47] T. Watanabe, *Res. Mech.* 11 (1984) 47.
- [48] T. Watanabe, *Mater. Sci. Eng. A* 176 (1994) 39.
- [49] V.Y. Gertsman, K. Tangri, *Acta Metall. Mater.* 43 (1995) 2317.
- [50] J.M. Howe, *Interfaces in Materials: Atomic Structure, Thermodynamic and Kinetics of Solid–Vapor, Solid–Liquid and Solid–Solid Interfaces*, Wiley, New York, 1997.
- [51] V. Randle, *The Measurement of Grain Boundary Geometry*, Institute of Physics Publishing, Bristol, 1993.
- [52] J.D. Rittner, D.N. Seidman, *Phys. Rev. B* 54 (1996) 6999.
- [53] J.D. Rittner, D.N. Seidman, *Mater. Sci. Forum* 207–209 (1996) 333.
- [54] W.T. Read, W. Shockley, *Phys. Rev.* 78 (1950) 275.
- [55] A.P. Sutton, V. Vitek, *Philos. Trans. R. Soc. London A* 309 (1983) 1.
- [56] A.P. Sutton, V. Vitek, *Philos. Trans. R. Soc. London A* 309 (1983) 37.
- [57] A.P. Sutton, V. Vitek, *Philos. Trans. R. Soc. London A* 309 (1983) 55.
- [58] G.J. Wang, A.P. Sutton, V. Vitek, *Acta Metall.* 32 (1984) 1093.
- [59] A.P. Sutton, R.W. Balluffi, *Philos. Mag. Lett.* 61 (1990) 91.
- [60] J.D. Rittner, D.N. Seidman, K.L. Merkle, *Phys. Rev. B* 53 (1996) 4241.
- [61] V. Volterra, *Ann. Ecole Norm. Super.* 24 (1907) 401.
- [62] J.C.M. Li, *Surf. Sci.* 31 (1972) 12.
- [63] K.K. Shih, J.C.M. Li, *Surf. Sci.* 50 (1975) 109.
- [64] A.E. Romanov, *Mater. Sci. Eng. A* 164 (1993) 58.
- [65] D.V. Bachurin, R.T. Murzaev, A.A. Nazarov, *Fiz. Met. Metalloved.* 96 (2003) 11.
- [66] V.Y. Gertsman, A.A. Nazarov, A.E. Romanov, R.Z. Valiev, V.I. Vladimirov, *Philos. Mag. A* 59 (1989) 1113.
- [67] A.A. Nazarov, O.A. Shenderova, D.W. Brenner, *Mater. Sci. Eng. A* 281 (2000) 148.
- [68] R.Z. Valiev, V.I. Vladimirov, V.Y. Gertsman, A.A. Nazarov, A.E. Romanov, *Phys. Met. Metallography* 69 (1990) 30.
- [69] J.P. Hirth, R.C. Pond, J. Lothe, *Acta Mater.* 54 (2006) 4237.
- [70] C. Somigliana, *Rend. CI. Sci. Fis. Mat. Nat.* 23 (1914) 463.

- [71] G. Xu, A.S. Argon, *Mater. Sci. Eng. A* 319–321 (2001) 144.
- [72] S. Ogata, J. Li, S. Yip, *Science* 298 (2002) 807.
- [73] M.A. Tschoopp, D.E. Spearot, D.L. McDowell, *Modell. Simul. Mater. Sci. Eng.* 15 (2007) 693.
- [74] T. Zhu, J. Li, K.J. Van Vliet, S. Ogata, S. Yip, S. Suresh, *J. Mech. Phys. Solids* 52 (2004) 691.
- [75] M.P. Allen, D.J. Tildesley, *Computer Simulations of Liquids*, Clarendon Press, Oxford, 1987.
- [76] J.M. Haile, *Molecular Dynamics Simulation: Elementary Methods*, Wiley, New York, 1992.
- [77] J.R. Shewchuk, <http://www-2.cs.cmu.edu/~jrs/jrspapers.html#cg>, 1994.
- [78] D. Wolf, *Acta Metall.* 38 (1990) 781.
- [79] M.A. Tschoopp, D.L. McDowell, *Philos. Mag.* 87 (2007) 3147.
- [80] D.L. Medlin, M.J. Mills, W.M. Stobbs, M.S. Daw, F. Cosandey, *Mater. Res. Soc. Sympos. Proc.* 295 (1993) 91.
- [81] J.M. Penisson, U. Dahmen, M.J. Mills, *Philos. Mag. Lett.* 64 (1991) 277.
- [82] U. Wolf, F. Ernst, T. Muschik, M.W. Finnis, H.F. Fischmeister, *Philos. Mag. A* 66 (1992) 991.
- [83] F. Ernst, M.W. Finnis, A. Koch, C. Schmidt, B. Straumal, W. Gust, *Z. Metallkd.* 87 (1996) 911.
- [84] F. Ernst, M.W. Finnis, D. Hofmann, T. Muschik, U. Schonberger, U. Wolf, M. Methfessel, *Phys. Rev. Lett.* 69 (1992) 620.
- [85] D. Hofmann, M.W. Finnis, *Acta Metall. Mater.* 42 (1994) 3555.
- [86] H.C. Andersen, *J. Chem. Phys.* 72 (1980) 2384.
- [87] S. Melchionna, G. Ciccotti, B.L. Holian, *Mol. Phys.* 78 (1993) 533.
- [88] W.G. Hoover, *Phys. Rev. A* 31 (1985) 1695.
- [89] S. Nose, *Mol. Phys.* 52 (1984) 255.
- [90] K.S. Cheung, S. Yip, *J. Appl. Phys.* 70 (1991) 5688.
- [91] J. Cormier, J.M. Rickman, T.J. Delph, *J. Appl. Phys.* 89 (2001) 99.
- [92] J.F. Lutsko, *J. Appl. Phys.* 64 (1988) 1152.
- [93] D.H. Tsai, *J. Chem. Phys.* 70 (1979) 1375.
- [94] M. Zhou, *Proc. R. Soc. London A* 459 (2003) 2347.
- [95] J.A. Zimmerman, E.B. Webb III, J.J. Hoyt, R.E. Jones, P.A. Klein, D.J. Bammann, *Modell. Simul. Mater. Sci. Eng.* 12 (2004) S319.
- [96] M.S. Daw, M.I. Baskes, *Phys. Rev. Lett.* 50 (1983) 1285.
- [97] M.S. Daw, M.I. Baskes, *Phys. Rev. B* 29 (1984) 6443.
- [98] M.S. Daw, *Phys. Rev. B* 39 (1989) 7441.
- [99] Y. Mishin, D. Farkas, M.J. Mehl, D.A. Papaconstantopoulos, *Phys. Rev. B* 59 (1999) 3393.
- [100] Y. Mishin, M.J. Mehl, D.A. Papaconstantopoulos, A.F. Voter, J.D. Kress, *Phys. Rev. B* 63 (2001) 224106.
- [101] J.R. Rice, *J. Mech. Phys. Solids* 40 (1992) 239.
- [102] R.D. Boyer, J. Li, S. Ogata, S. Yip, *Modell. Simul. Mater. Sci. Eng.* 12 (2004) 1017.
- [103] J.A. Zimmerman, H. Gao, F.F. Abraham, *Modell. Simul. Mater. Sci. Eng.* 8 (2000) 103.
- [104] J.A. Hurtado, B.R. Elliott, H.M. Shodja, D.V. Gorelikov, C.E. Campbell, H.E. Lippard, T.C. Isabell, J. Weertman, *Mater. Sci. Eng. A* 190 (1995) 1.
- [105] L.E. Shilkrot, W.A. Curtin, R.E. Miller, *J. Mech. Phys. Solids* 50 (2002) 2085.
- [106] L.E. Shilkrot, R.E. Miller, W.A. Curtin, *J. Mech. Phys. Solids* 52 (2004) 755.
- [107] R. Miller, M. Ortiz, R. Phillips, V. Shenoy, E.B. Tadmor, *Eng. Fract. Mech.* 61 (1998) 427.
- [108] R. Miller, E.B. Tadmor, R. Phillips, M. Ortiz, *Modell. Simul. Mater. Sci. Eng.* 6 (1998) 607.
- [109] D.E. Spearot, *Atomistic Calculations of Nanoscale Interface Behavior in FCC Metals*, Ph.D. dissertation, Georgia Institute of Technology, 2005.
- [110] V. Tomar, M. Zhou, *J. Mech. Phys. Solids* 55 (2007) 1053.
- [111] P. Muller, A. Saul, *Surf. Sci. Rep.* 54 (2004) 157.
- [112] P. Nozieres, D.E. Wolf, *Z. Phys. B* 70 (1988) 399.
- [113] D.E. Wolf, P. Nozieres, *Z. Phys. B* 70 (1988) 507.
- [114] P. Grigoriadis, T. Karakostas, P. Komninou, V. Pontikis, *Mater. Sci. Forum* 294–296 (1999) 177.
- [115] C.L. Kelchner, S.J. Plimpton, J.C. Hamilton, *Phys. Rev. B* 58 (1998) 11085.
- [116] M.J. Mills, M.S. Daw, G.J. Thomas, F. Cosandey, *Ultramicroscopy* 40 (1992) 247.
- [117] G.S. Rohrer, D.M. Saylor, B. El Dasher, B.L. Adams, A.D. Rollett, P. Wynblatt, *Z. Metallkd.* 95 (2004) 197.
- [118] C.S. Kim, Y. Hu, G.S. Rohrer, V. Randle, *Scripta Mater.* 52 (2005) 633.

- [119] K. Barmak, J. Kim, C.S. Kim, W.E. Archibald, G.S. Rohrer, A.D. Rollett, D. Kinderlehrer, S. Ta'asan, H. Zhang, D.J. Srolovitz, *Scripta Mater.* 54 (2006) 1059.
- [120] D.M. Saylor, B. El Dasher, T. Sano, G.S. Rohrer, *J. Am. Ceram. Soc.* 87 (2004) 670.
- [121] D.M. Saylor, B.S. El Dasher, A.D. Rollett, G.S. Rohrer, *Acta Mater.* 52 (2004) 3649.
- [122] D.M. Saylor, A. Morawiec, G.S. Rohrer, *Acta Mater.* 51 (2003) 3663.
- [123] C. Minkwitz, C. Herzig, E. Rabkin, W. Gust, *Acta Mater.* 47 (1999) 1231.
- [124] H. Miyamoto, K. Ikeuchi, T. Mimaki, *Scripta Mater.* 50 (2004) 1417.
- [125] C. Schmidt, M.W. Finnis, F. Ernst, V. Vitek, *Philos. Mag. A* 77 (1998) 1161.
- [126] T. Muschik, W. Laub, U. Wolf, M.W. Finnis, W. Gust, *Acta Metall. Mater.* 41 (1993) 2163.
- [127] M.A. Tschopp, D.L. McDowell, *Philos. Mag.* 87 (2007) 3871.
- [128] U. Wolf, P. Gumbsch, H. Ichinose, H.F. Fischmeister, *J. Phys. (Paris), Colloque C 1* (1990) 359.
- [129] D.L. Medlin, G.H. Campbell, C.R. Carter, *Acta Mater.* 46 (1998) 5135.
- [130] M.A. Tschopp, D.L. McDowell, *J. Mater. Sci.* 42 (2007) 7806.
- [131] M.L. Kronberg, F.H. Wilson, *Am. Inst. Min. Metall. Eng. J. Met.* 1 (1949) 501.
- [132] A.P. Sutton, *Acta Metall.* 36 (1988) 1291.
- [133] A.P. Sutton, *Interfaces in Crystalline Materials*, Clarendon Press, Oxford, 1995.
- [134] J.-M. Zhang, F. Ma, K.-W. Xu, *Appl. Surf. Sci.* 229 (2004) 34.
- [135] J.A. Zimmerman, C.L. Kelchner, P.A. Klein, J.C. Hamilton, S.M. Foiles, *Phys. Rev. Lett.* 87 (2001) 165507.
- [136] T.S. Byun, *Acta Mater.* 51 (2003) 3063.
- [137] M.I. Baskes, R.G. Hoagland, T. Tsuji, *Modell. Simul. Mater. Sci. Eng.* 6 (1998) 9.
- [138] W.F. Hosford, *The Mechanics of Crystals and Textured Polycrystals*, Oxford University Press, Oxford, 1993.
- [139] T. Zhu, J. Li, A. Samanta, H.G. Kim, S. Suresh, *Proc. Natl. Acad. Sci.* 104 (2007) 3031.
- [140] C. Schuh, J.K. Mason, A.C. Lund, *Nat. Mater.* 4 (2005) 617.
- [141] M.A. Tschopp, D.L. McDowell, *Appl. Phys. Lett.* 90 (2007) 121916.
- [142] C.R. Krenn, D. Roundy, M.L. Cohen, D.C. Chrzan, J.W. Morris, *Phys. Rev. B* 65 (2002) 134111.
- [143] C.R. Krenn, D. Roundy, J.W. Morris Jr., M.L. Cohen, *Mater. Sci. Eng. A* 317 (2001) 44.
- [144] D. Roundy, C.R. Krenn, M.L. Cohen, J.W. Morris Jr., *Phys. Rev. Lett.* 82 (1999) 2713.
- [145] P. Steinmann, E. Kuhl, E. Stein, *Int. J. Solids Struct.* 35 (1998) 4437.
- [146] J.K. Diao, K. Gall, M.L. Dunn, *Nano Lett.* 4 (2004) 2431.
- [147] V. Tomar, M. Zhou, *Appl. Phys. Lett.* 88 (2006).
- [148] A.C. Lund, T.G. Nieh, C.A. Schuh, *Phys. Rev. B* 69 (2004).
- [149] A.C. Lund, C.A. Schuh, *Acta Mater.* 53 (2005) 3193.
- [150] A.C. Lund, C.A. Schuh, *Acta Mater.* 51 (2003) 5399.
- [151] S. Cheng, J.A. Spencer, W.W. Milligan, *Acta Mater.* 51 (2003) 4505.
- [152] D.E. Spearot, K.I. Jacob, D.L. McDowell, *Mech. Mater.* 36 (2004) 825.
- [153] M.A. Tschopp, G.J. Tucker, D.L. McDowell, *Acta Mater.* 55 (2007) 3959.
- [154] V. Yamakov, D. Wolf, S.R. Phillpot, A.K. Mukherjee, H. Gleiter, *Nat. Mater.* 3 (2004) 43.
- [155] R.J. Asaro, S. Suresh, *Acta Mater.* 53 (2005) 3369.
- [156] T. Zhu, J. Li, A. Samanta, A. Leach, K. Gall, *Phys. Rev. Lett.* 100 (2008) 025502.
- [157] Y.M. Wang, E. Ma, *Mater. Sci. Eng. A* 375–377 (2004) 46.
- [158] L. Lu, R. Schwaiger, Z.W. Shan, M. Dao, K. Lu, S. Suresh, *Acta Mater.* 53 (2005) 2169.
- [159] H. Conrad, K. Jung, *Mater. Sci. Eng. A* 391 (2005) 272.
- [160] A.G. Froseth, H. Van Swygenhoven, P.M. Derlet, *Acta Mater.* 53 (2005) 4847.
- [161] M. Frary, C.A. Schuh, *Phys. Rev. B* 69 (2004) 134115.
- [162] C.A. Schuh, R.W. Minich, M. Kumar, *Philos. Mag.* 83 (2003) 711.
- [163] B.A. Bilby, E. Smith, *Proc. R. Soc. London A* 236 (1956) 481.
- [164] L.P. Evers, D.M. Parks, W.A.M. Brekelmans, M.G.D. Geers, *J. Mech. Phys. Solids* 50 (2002) 2403–2424.
- [165] J.D. Clayton, D.J. Bammann, D.L. McDowell, *Philos. Mag.* 85 (2005) 3983.
- [166] J.D. Clayton, D.L. McDowell, *Int. J. Plast.* 19 (2003) 1401.
- [167] S. Minagawa, *Arch. Mech.* 31 (1979) 783.
- [168] S. Minagawa, *Int. J. Eng. Sci.* 19 (1981) 1705.
- [169] B.A. Bilby, R. Bullough, E. Smith, *Proc. R. Soc. London A* 231 (1955) 263.
- [170] K.C. Le, H. Stumpf, *Int. J. Eng. Sci.* 34 (1996) 339.

- [171] K.C. Le, H. Stumpf, *Proc. R. Soc. London A* 452 (1996) 359.
- [172] W. Noll, *Arch. Rat. Mech. Anal.* 27 (1967) 1.
- [173] P. Steinmann, *Int. J. Eng. Sci.* 34 (1996) 1717.
- [174] J.A. Schouten, *Ricci Calculus*, Springer-Verlag, Berlin, 1954.
- [175] K. Kondo, *Int. J. Eng. Sci.* 2 (1964) 219.
- [176] R.W. Lardner, *Arch. Mech.* 25 (1973) 911.
- [177] R. De Wit, *Int. J. Eng. Sci.* 19 (1981) 1475.
- [178] J.D. Eshelby, *Philos. Trans. R. Soc. London A* 244 (1951) 87.
- [179] J.D. Eshelby, in: F. Séitz, D. Turnbull (Eds.), *Solid State Physics*, Academic Press, 1956, p. 79.
- [180] R.J. Asaro, *Int. J. Eng. Sci.* 13 (1975) 271.
- [181] J.F. Nye, *Acta Metall.* 1 (1953) 153.